DEVELOPMENT OF A LABORATORY VERIFIED SINGLE-DUCT VAV SYSTEM MODEL WITH FAN POWERED TERMINAL UNITS OPTIMIZED USING COMPUTATIONAL FLUID DYNAMICS

A Dissertation

by

MICHAEL A. DAVIS

Submitted to the Office of Graduate Studies of
Texas A&M University
in partial fulfillment of the requirements for the degree of

DOCTOR OF PHILOSOPHY

August 2010

Major Subject: Mechanical Engineering

DEVELOPMENT OF A LABORATORY VERIFIED SINGLE-DUCT VAV SYSTEM MODEL WITH FAN POWERED TERMINAL UNITS OPTIMIZED USING COMPUTATIONAL FLUID DYNAMICS

A Dissertation

by

MICHAEL A. DAVIS

Submitted to the Office of Graduate Studies of
Texas A&M University
in partial fulfillment of the requirements for the degree of

DOCTOR OF PHILOSOPHY

Approved by:

Chair of Committee, Dennis O'Neal
Committee Members, John Bryant
Warren Heffington
Bryan Rasmussen
Head of Department, Dennis O'Neal

August 2010

Major Subject: Mechanical Engineering

ABSTRACT

Development of a Laboratory Verified Single-Duct
VAV System Model with Fan Powered Terminal Units
Optimized Using Computational Fluid Dynamics. (August 2010)
Michael A. Davis, B.S., Texas A&M University; M.S., Texas A&M University
Chair of Advisory Committee: Dr. Dennis O'Neal

Single Duct Variable Air Volume (SDVAV) systems use series and parallel Fan Powered Terminal Units to control the air flow in conditioned spaces. This research developed a laboratory verified model of SDVAV systems that used series and parallel fan terminal units where the fan speeds were controlled by either Silicon Controlled Rectifiers (SCR) or Electronically Commutated Motors (ECM) motors. As part of the research, the model was used to compare the performance of the systems and to predict the harmonics generated by ECM systems. All research objectives were achieved.

The CFD model, which was verified with laboratory measurements, showed the potential to identify opportunities for improvement in the design of the FPTU and accurately predicted the static pressure drop as air passed through the unit over the full operating range of the FPTU.

Computational fluid dynamics (CFD) models of typical a FPTU were developed and used to investigate opportunities for optimizing the design of FPTUs. The CFD model identified key parameters required to conduct numerical simulations of FPTU and some

of the internal components used to manufacture the units. One key internal component was a porous baffle used to enhance mixing when primary air and induced air entered the mixing chamber. The CFD analysis showed that a pressure-drop based on face velocity model could be used to accurately predict the performance of the FPTU.

The SDVAV simulation results showed that parallel FPTUs used less energy overall than series systems that used SCR motors as long as primary air leakage was not considered. Simulation results also showed that series ECM FPTUs used about the same amount of energy, within 3%, of parallel FPTU even when leakage was not considered. A leakage rate of 10% was enough to reduce the performance of the parallel FPTU to the level of the series SCR system and the series ECM FPTUs outperformed the parallel FPTUs at all weather locations used in the study.

ACKNOWLEDGEMENTS

This work was partially funded by ASHRAE and QNRF. I would like to thank both groups for their financial support.

I would like to thank my advisor, Dr. Dennis O'Neal, and committee members, Dr. John Bryant, Dr. Warren Heffington, and Dr. Bryan Rasmussen. Dr. O'Neal has provided valuable guidance on this research and given me academic and career advice along with encouragement and unfailing moral support that has been invaluable. Dr. Bryant provided both academic and professional advice as well as encouragement during this work. Dr. Heffington and Dr. Rasmussen both graciously agreed to serve on my committee. I acknowledge and appreciate the contributions and service of all of my committee members. Thank you.

Finally, thanks to my wife, Sally, and kids for their encouragement and support. For years Sally has patiently endured the evenings and weekends when we couldn't go anywhere or do anything because I was "working." Thank you.

NOMENCLATURE

BEMS	Building energy management system
CAV	Constant air volume
CFM	Cubic feet per minute (ft^3/min)
C_{pl}	Latent heating/cooling specific heat
C_{ps}	Sensible heating/cooling specific heat
$C_1 \ldots C_n$	Coefficients of an equation
ECM	Electronically commutated motor
FPTU	Fan powered terminal unit
HVAC	Heating, ventilating and air-conditioning
K	Constant relating ΔP to $\dot{Q}^2$ (in w.g.-min^2 / ft^6)
L_p	Primary air leakage as decimal percent of primary flow
$\dot{m}$	Mass flow rate (lb/min)
$\dot{m}_f$	Terminal unit fan air mass flow rate (lb/min)
$\dot{m}_p$	Primary air mass flow rate (lb/min)
$\dot{m}_s$	Supply air mass flow rate (lb/min)
$\dot{m}_L$	Leakage mass flow rate (lb/min)
PCC	Point of common coupling
P_{dwn}	Down stream static pressure (in. w.g.)
P_{iav}	Primary air inlet valve entering air velocity differential pressure (in. w.g.)

ΔP	Pressure drop (in w.g)
$\dot{Q}$	Volumetric air flow rate (ft^3/min)
Q_{aux}	Auxiliary sensible heat added (Btu/h)
Q_f	Fan power (Btu/h)
$\dot{Q}_f$	Flow rate of the terminal unit fan (ft^3/min)
$\dot{Q}_{ind}$	Induced air flow rate (ft^3/min)
$\dot{Q}_L$	Leakage flow rate (ft^3/min)
Q_{lat}	Latent space load (Btu/h)
Q_{min}	Minimum sensible cooling supplied to a zone (Btu/h)
$\dot{Q}_p$	Primary air flow rate (ft^3/min)
$\dot{Q}_{pmin}$	Primary minimum air flow rate (ft^3/min)
$\dot{Q}_r$	Return air flow rate (ft^3/min)
$\dot{Q}_s$	Supply air flow rate (ft^3/min)
Q_{sen}	Sensible space load (Btu/h)
RH	Relative humidity (%)
RH_p	Primary air relative humidity (%)
S	Damper position in degrees
SCR	Silicon controlled rectifier
T_L	Leaked air temperature (°F)
T_p	Primary air temperature (°F)
T_{pfest}	Estimated pre-fan mixed air temperature (°F)

T_{rpf}	Required pre-fan mixed air temperature (°F)
T_r	Return air temperature (°F)
T_s	Supply air temperature (°F)
T_{sest}	Supply temperature (°F) based on current conditions
T_{sreq}	Supply temperature (°F) required to maintain T_{sp}
T_{sp}	Set point temperature (°F)
V	FPTU fan control voltage
VAV	Variable air volume
$\dot{W}_f$	Fan power (Watts)
ω_r	Return air humidity ratio ($lb_{moiture}/lb_{air}$)
ω_p	Primary air humidity ratio ($lb_{moiture}/lb_{air}$)
ρ	Density of the air (lb/ft^3)

TABLE OF CONTENTS

Page

CHAPTER Page

CHAPTER Page

LIST OF FIGURES

Page

Page

Page

LIST OF TABLES

Page

Page

Page

CHAPTER I

INTRODUCTION

Introduction / background

Air conditioning systems in large commercial office buildings typically utilize single duct variable air volume (SDVAV) air distribution systems. SDVAV systems vary the primary (conditioned) airflow into the conditioned zones in a building in response to the change in the cooling or heating loads. SDVAV systems provide significant energy savings over conventional constant volume systems. A critical component in SDVAV systems is the Fan Powered Terminal Unit (FPTU) which is also known as a Powered Induction Unit (PIU). For this thesis, only the FPTU term will be used.

Figure 1-1 shows a typical SDVAV system using FPTU. A SDVAV system supplies conditioned air through a primary duct system to multiple zones. Each zone has a FPTU that was sized to handle the peak cooling load for the zone. There are two basic types of fan powered terminal units: (1) series and (2) parallel fan arrangements. The purpose of the FPTU is to control the flow of conditioned air supplied by the primary fan. By adjusting the amount of primary air to meet the space load, the amount of reheat required to maintain space conditions can be reduced or eliminated.

The FPTU has a small fan that is mounted either in series or in parallel with the primary system fan. First generation FPTUs had constant speed fans where the fan

---

This dissertation follows the style of *HVAC&R Research*.

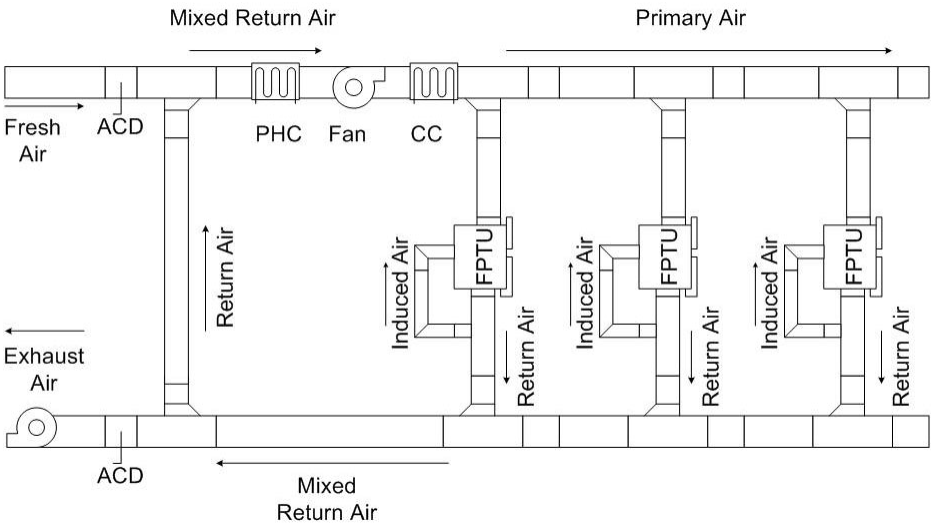

Figure 1-1: A typical multi-zone SDVAV system using fan-powered terminal units.

motor speed was regulated with a silicon controlled rectifier (SCR) controller. Once the fan speed was set during the installation and commissioning process, it was then operated as a constant speed on or off device.

In recent years, manufacturers have begun to make available electronically commutated motors (ECM) in FPTUs. An ECM allows the speed of the fan to vary as a function of a control signal from the building energy management system (BEMS or BMS) and can be modulated as the load in the zone changes. ECM motors also use about one-third of the energy of a similar sized SCR controlled motor and they have the potential to reduce the cooling and fan energy use in commercial buildings. However, they cost more than conventional single speed motors in FPTUs and have the undesirable side-effect of introducing harmonic distortions into the buildings' electrical power grid.

During the years that VAV systems began to gain popularity, Inoue and Matsumoto (1979) concluded that a VAV system could reduce supply fan power consumption by 40% compared to a dual duct constant air volume (CAV) or a terminal reheat CAV system. These conclusions were based on computer simulations using HASP/ACLD 7101 (Inoue and Matsumoto 1979), an HVAC simulation tool developed in Japan, and validated by a field study on a building in Tokyo.

FPTUs first appeared in 1974 (In-Hout 2008). Initial versions of FPTU consisted of parallel units which were followed by the introduction of the series type units.

Figure 1-2 shows a schematic of a typical parallel FPTU. The unit is called a parallel FPTU because the air flow path of the terminal fan is parallel to the air flow path of the primary fan. The parallel unit fan only operates at low primary air flow conditions. As a result of the low-load operation, many engineers have the perception that they use less energy to operate than the series FPTU.

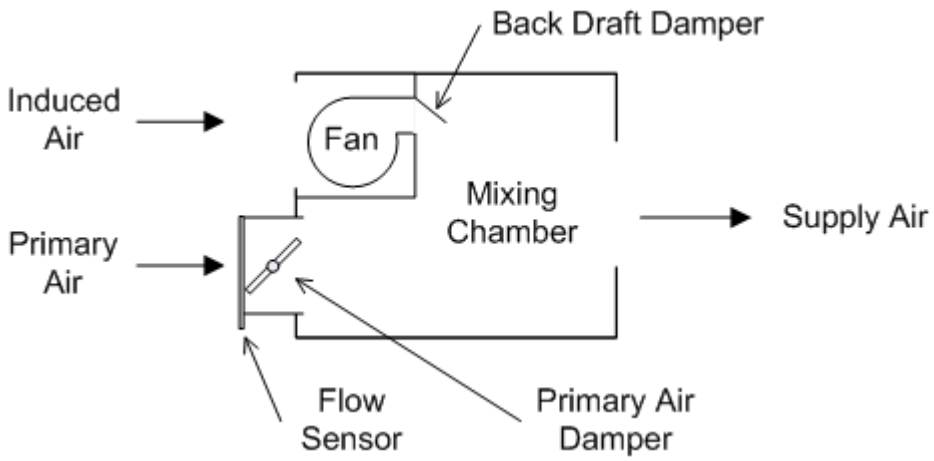

Figure 1-2: A typical parallel type fan powered terminal unit.

Figure 1-3 shows a schematic of a typical series FPTU. The unit is called a series FPTU because the unit fan is in series with the primary fan. The series unit fan always operates when space conditions are being actively controlled by the HVAC system. During off hours, the unit fans and primary air are turned off.

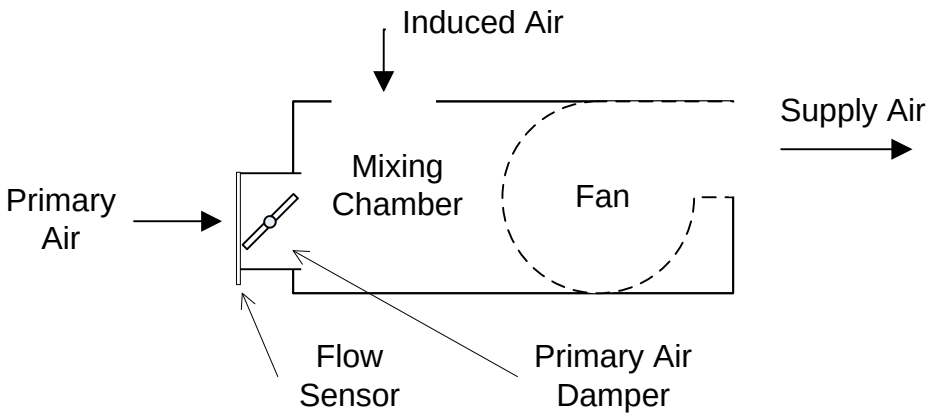

Figure 1-3: A typical series type fan powered terminal unit.

Sekhar (1997) had similar conclusions to Inoue and Matsumoto (1979) based on a set of computer simulations on two buildings. Sekhar quantified energy savings for buildings located in a hot and humid environment. He concluded that between 10% and 20% combined fan and cooling energy could be saved by employing a VAV system. However, in his study and that by Inoue and Matsumoto (1979), the VAV systems consisted of damper-only operated VAV terminal units and did not include fan powered terminal units.

Ardehali and Smith (1996) conducted a simulation that compared CAV systems and VAV systems using fan powered terminal units. The simulation, utilizing the TRACE

(1993) program, modeled a commercial building in Des Moines, Iowa. The building was selected to represent a 'typical' existing office building. The results of the simulations indicated that a fan powered VAV system could result in energy savings that could provide a 40% reduction in utility costs compared to a CAV system.

All of these studies indicated that VAV systems were a significant improvement over CAV systems. Because they have been proven to be the most energy efficient method for air distribution, the current challenge is to improve VAV systems. Proper application of parallel and series fan VAV systems has become an important issue particularly in light of the introduction of ECM motors and the potential harmonic distortions they introduce into the building's power supply. The general disagreement concerning the energy differences between systems of these two VAV terminal units has led to several investigations into the overall power consumption of the two systems.

Elleson (1993) conducted a field study of cold air distribution systems with series and parallel fan powered mixing terminal units in two separate buildings. Cold air distribution systems use reduced temperature supply air, typically at 45 °F (7.2 °C), which requires less primary air delivered to the conditioned space than a higher temperature system, resulting in supply fan energy savings. Field data were compared to the results from computer simulations of alternative air distribution systems for each building. Although the focus of the paper was to provide evidence supporting cold air distribution systems, the results from the simulations provided a comparison between series and parallel systems for both cold air and conventional air distribution systems.

For both cold air and conventional systems, the results showed that the total fan power consumption, combining the power of the supply fan and terminal units' fans, was greater for series FPTUs. This conclusion was based on results of simulations on one of the two buildings studied. The simulations included a reduced supply static pressure for series units of 0.25 in. w.g. (62 Pa) less than the parallel units' design static pressure.

A study sponsored by the California Energy Commission included a comparison of parallel and series terminal units operating in perimeter zones (Kolderup et al. 2003). The study was based on running a simulation with DOE 2.2 (LBNL 1998) and attempted to account for the reduced static pressure of the main supply fan in a series system. The main supply fan static pressure was reduced from 4.0 to 3.67 in. w.g. (996 to 914 Pa) for the series systems. The findings concluded that, for the case studied, a parallel system would have 9% less energy costs than a series system. The bulk of the energy savings was in the difference in total power consumption of the fans. The explanation given for the energy difference was that since the series fans were in constant operation, and they were less efficient than the larger primary supply fan, a series system had greater energy consumption than a parallel system. However, the study only simulated a single building in California. A building located in a cooler climate could expect larger supplemental heating requirements, in which the parallel terminal unit fans would be required to operate longer hours, and use more energy.

The studies by Elleson (1993) and Kolderup et al. (2003) use the built-in functions of their HVAC simulation software to model the fan powered terminal units. These built-in functions approximate the terminal units, ignoring some variables (U.S. Department of

Energy 1982) such as leakage in parallel units. The effect of the SCR on power consumption is ignored. Other design differences, such as the type of primary air or back draft dampers are also not included. As a result, these built-in functions do not fully describe the characteristics of typical fan powered terminal units and do not include any allowance for modeling leakage from parallel units.

There was no experimental evidence to support the computer simulations by Elleson (1993) and Kolderup et al. (2003) who claimed that parallel VAV systems are more energy efficient than a series system. There was a need to develop a better understanding of systems using parallel and series fan powered VAV terminal units. To model the system properly, it is important to be able to characterize the individual units. To date, there has been little work in this area. Khoo et al. (1998) developed non-linear models for three VAV terminal units. They focused on standard VAV terminal units without fans. The empirical models approximated the pressure drop across the entire unit as a function of damper position. Because of the non-linear relationship between pressure drop and the position of the damper, logarithmic functions were used to express this relationship. This study concluded that the damper-only approximations of VAV terminal units used in some HVAC simulation packages were not accurate representations of VAV terminal units.

The performance of single speed FPTUs has recently been characterized by Furr et al. (2007). In a follow-on project, the characterization of ECM based FPTU was started by Cramlet (2008) and completed by Edmondson (2009). Leakage is when the primary air flows directly through the FPTU into the return air stream without passing through

the conditioned space. Both of the studies by Furr et al. (2007) and Edmondson (2009) showed that parallel terminal units can and do leak and that some parallel FPTUs can have primary air leakage rates in excess of 10%. The studies also showed that series terminal units have a potential for leakage but leakage will occur only if the control system drives more primary air into the mixing chamber than the unit fan is set up to supply to the conditioned space. Previous system level studies did not include leakage.

A system level study was done by Davis et al. (2007) that included the effects of leakage in parallel FPTUs. The study evaluated the energy consumption of SCR controlled series and parallel FPTUs at five weather locations around the United States. The study showed that when leakage rates for parallel FPTUs were below 10%, the parallel units used less energy. The problem is that laboratory measurements by Furr et al. (2007) and Edmondson (2009) showed that leakage rates of 10% were possible and that depending on the how the units are installed, maintained, and operated there may be no significant difference between the annual energy consumption of either series or parallel units.

Calculating changes in the properties of air

The simulations required modeling of some basic thermodynamic processes such as sensible heating of the primary air by the duct heaters and FPTU fans, cooling and dehumidification at the cooling coil, and mixing of air stream at different temperatures and humidity ratios. For this project, the calculation procedures were simplified by assuming constant properties, which for the temperature ranges of interest to this project resulted in less than a 0.2% error in the calculations (Cengal et al 2005).

Assumptions that were made to simplify the equations were that all processes were constant density. The values that defined the range of interest were determined by the operating parameters set by the industry advisory board that guided the simulation work and included the range of moist air from 55 F, 95% RH to 78 F, 50% RH. The density of air at 55 F 95% RH was 0.076 lb/ft^3 and was used to derive Equation 1-1 as shown in Appendix I. Equation 1-1 was used throughout the simulations to model sensible heating and cooling.

$$Q = C_s \dot{Q}(T_2 - T_1) \tag{1-1}$$

where Csens was a combination of the specific heat and the conversion factors that accounted for the volumetric flow rate, $\dot{V}$, in ft3/min and the density of the moist air in lb/ft3. T2 and T1 were the dry bulb temperatures that defined the end points of the process. Equation 1-2 was used throughout the simulations to model constant temperature moisture changes such as latent heat that was added to the return air as a result of a latent load in a conditioned space.

$$Q = C_l \dot{Q}(\omega_2 - \omega_1) \tag{1-2}$$

The latent and sensible space loads were generated by the DOE2 simulations that were done in the early stages of the project. Equation 1-3 (Kreider 2002) represents the enthalpy of moist air.

$$h = c_{pa}T_d + \omega(h_{g,ref} + c_{pw}T_d) \quad (1\text{-}3)$$

Equations 1-1 and 1-2 were derived from equation 1-3 as shown in Appendix 1. The values used throughout this project for C_{ps} and C_{pl} were 1.1 BTUs-min/(hr-ft^3-F) and 4840 BTUs-min-lb$_{air}$/(hr-ft^3-lb$_{water}$), respectively, as shown in Appendix I. The values for C_{ps} and C_{ps} were inputs to the simulation and could be varied if the temperature ranges were outside of the parameters defined by the industry advisors as shown in the appendix.

Research objectives

This research project had six main objectives:

1. Develop a system model of a single-duct VAV system using fan-powered terminal units based on the characteristics of currently manufactured FPTUs.
2. Develop a software model that can be used to evaluate the operation of a single-duct VAV system based on either series or parallel terminal units.
3. Use the software model to estimate the total overall energy consumption of series and parallel based systems.
4. Compare the total energy use of series and parallel based systems at five distinct weather locations within the continental United States.

5. Develop a fan-powered terminal unit model that could be offered to the Department of Energy (DOE) as an upgrade to the model that is used in EnergyPlus.
6. Demonstrate that Computational Fluid Dynamics can be used as a design tool that can be used to improve the performance of FPTU.

All of the research objectives were achieved and this thesis describes the results. Chapter II provides a literature review. Chapter III describes the model of the operation of a zone that is controlled by a parallel FPTU. Chapter IV describes the model of the operation of a zone that is controlled by a series FPTU. Chapter V describes the model of the operation a system that uses either series or parallel FPTUs. Chapter VI describes the results of the base case model for series and parallel FPTU. After the description of the base case, Chapter VI details the results of the comparisons between the series and parallel units at various operating conditions and at five locations in the United States. Chapter VII covers the development of a Computational Fluid Dynamics (CFD) model for FPTUs. Chapter VIII describes the results of the CFD model. Chapter IX summarizes the results from the project and provides conclusions from the results.

CHAPTER II

LITERATURE REVIEW

EnergyPlus is currently the standard for building energy simulations (DOE 2009) and includes a model of FPTUs but uses the term Power Induction Unit (PIU) instead of FPTU. EnergyPlus supports both series and parallel FPTUs, but the terminal unit fan is the same "generic" model used to simulate any type of forward curved fan. The work performed by Furr et al. (2007) showed that the performance of both series and parallel FPTUs were directly related to the design of the air flow path and that the unit performance was dependent upon the type of inlet air valve used as well as the geometry of the mixing chamber in the FPTU. The EnergyPlus model does not take into account any variations in box geometry and uses a simple static pressure flow model for computing terminal unit energy consumption (DOE 2009). As a result, the user may not get an accurate estimation of the energy consumption when doing side-by-side comparisons of two units of the same size (air flow rates) with different box geometries.

The variation in the primary air flow rates for VAV systems implies that it is possible to have a variation in the primary air static pressure. The EnergyPlus model does not calculate the minimum primary static pressure required to provide the primary air flow rate for a given zone load. Instead, EnergyPlus calculates the primary static pressure based on total flow and then adjusts the FPTU inlet air valve to achieve the desired air flow rates. Although this method has no impact on series units, it has the effect of setting the pressure differential across the fan for the parallel units. From a

practical standpoint this method does not cause any significant error if the building operator uses a constant primary static, but it will cause an error in the analysis if designers or building operators are searching for the “optimal” building operation parameters associated with off-peak loads.

The study by Furr et al. (2007) showed leakage potential for both the series and the parallel FPTU. The previous work by Ellison (1993) and Kolderup (2003) did not take into account the effect of leakage in the estimated operating costs of the systems that were studied. The EnergyPlus model does not include provisions for impact on the system when leakage is considered.

EnergyPlus (DOE 2009) does not include provisions for ECM motors used in a variable speed operating mode. The constant speed operation of the ECM motor can be modeled as a higher efficiency forward curved fan but the variable speed as a function primary static pressure and zone load is not currently supported.

The ECM characterization work done by Cramlet (2008) and Edmondson (2009) showed that ECM motors have the potential to introduce significant harmonic distortions into the building electrical power supply. The power quality analysis performed by Cramlet (2008) included harmonics associated with voltage, current and real power. Specific attention was given to triplen harmonics. Triplen harmonics are odd harmonics which are also multiples of 3. They represent zero sequence currents which are in phase with the fundamental frequency current. Triplen current harmonics add to each other and cause heat gain and voltage drop along the neutral conductor and induce noise into

nearby circuits (Kennedy 2000). EnergyPlus does not currently include the ability to analyze the impact on the system from triplen harmonics or triplen current.

In addition to triplen harmonics, Cramlet (2008) and Edmondson (2009) also reported total harmonic distortion with regards to power quality. THD accounts for all harmonics and is typically presented in percentage form. THD is defined as the ratio of cumulative harmonic frequencies over the fundamental as shown in equation 2-1.

$$THD = \frac{\sum harmonic\ powers}{fundamental\ frequency\ power} = \frac{f_2 + f_3 + \cdots + + f_n}{f_1} \quad (2\text{-}1)$$

Figure 2-1 is a graph of the real power harmonics from a SCR FPTU fan motor. Figure 2-2 is a graph of the real power harmonics from an ECM FPTU fan motor. Although the power values shown in the graphs may not seem significant, consider that in a typical installation there may be hundreds of these devices attached to a single building's electrical system.

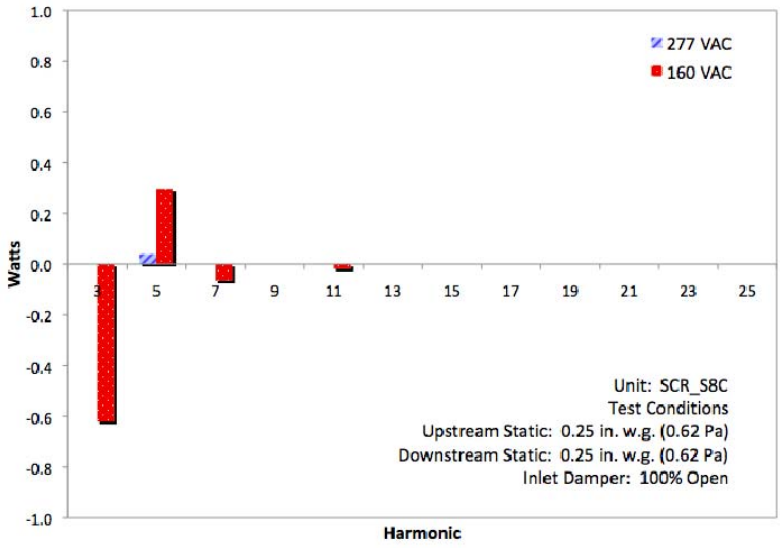

Figure 2-1: SCR series real power harmonics. (Cramlet 2008)

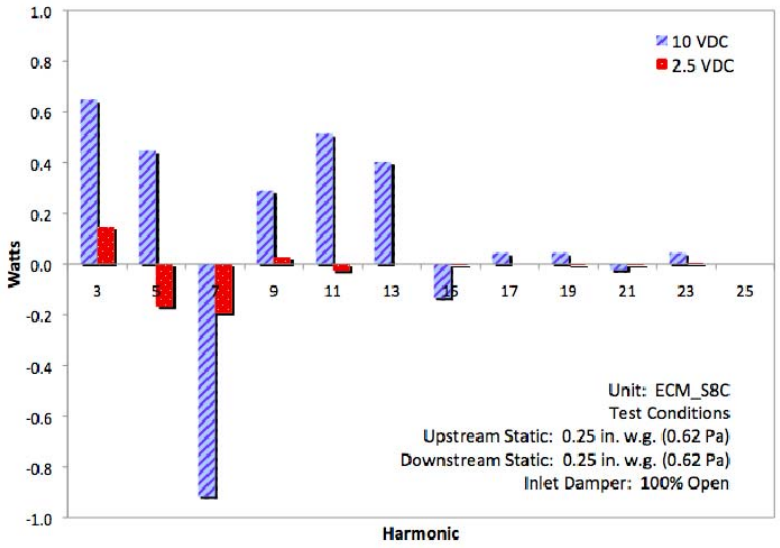

Figure 2-2: ECM series real power harmonics. (Edmondson 2009)

Figure 2-3 is a graph of the voltage harmonics from an SCR FPTU fan motor.

Figure 2-4 is a graph of the voltage harmonics from an ECM FPTU fan motor.

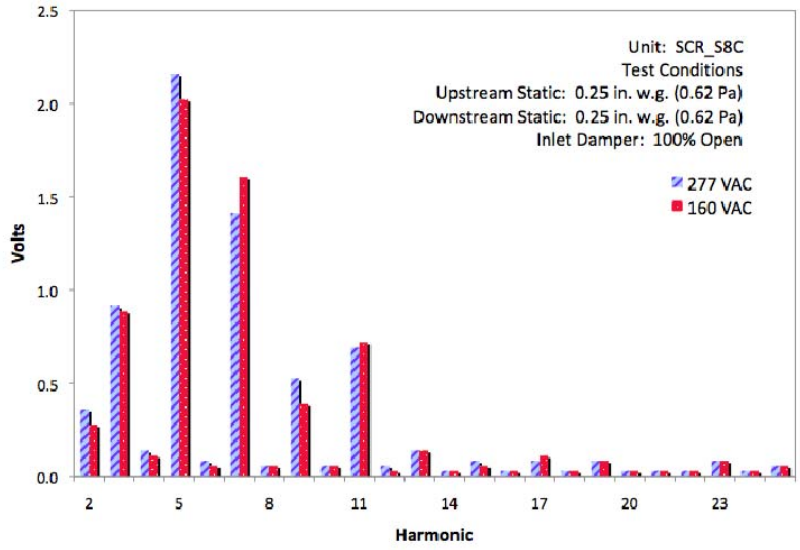

Figure 2-3: SCR series voltage harmonics. (Cramlet 2008)

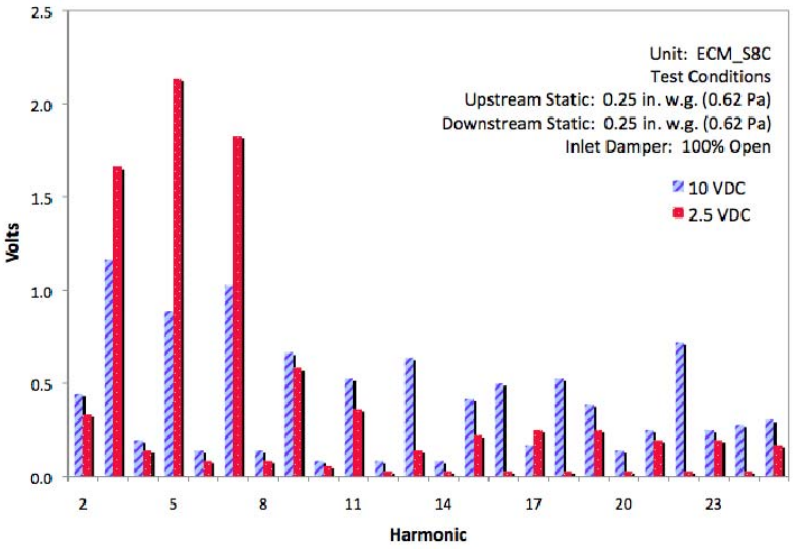

Figure 2-4: ECM series voltage harmonics. (Edmondson 2009)

The significance of Figures 2-1 through 2-4 is the harmonic content of ECM FPTUs in comparison to the SCR FPTUs. Figure 2-2 shows that there is more harmonic power consumption present in the S8 ECM terminal unit, compared to the S8 SCR unit and that the magnitudes of the real power consumption are higher. There is also more triplen power consumption present which implies the presence of triplen currents. Figures 2-3 and 2-4 show the presence of harmonic voltages. When harmonic voltages are fed back into the power line they induce harmonic currents in nearby equipment which could be damaged if not properly protected. Figure 2-4 shows a significant increase in the presence of harmonic voltages for ECM FPTU compared to the SCR FPTU.

The adverse effects of THD include the overheating of induction motors, transformers and capacitors and the overloading of neutrals (Gosbell 2000). EnergyPlus does not currently have provisions to support the characterization of the impact of the harmonics from the ECM motors.

The literature review combined with recent work indicated that the characterization of FPTUs with ECM motors needed to be continued. A system model needed to be developed that reflected the actual performance of FPTUs in a multi-zone air distribution system. The system model needed to include support that allowed the operator or designer to determine the optimal system operation from the zone loads and the actual operating characteristics of the FPTUs.

Currently, there are numerous manufacturers that produce a wide variety of SCR and ECM controlled series and parallel FPTU. A review of the currently manufactured types of FPTUs resulted in three basic variations in the series and the parallel units. The

variation in the types of FPTUs and the features of these units is characterized in Table 2-1 for series FPTUs and Table 2-2 for parallel FPTUs. The units shown in the tables consisted of various combinations of primary air inlet control dampers, air flow mixing chambers, air flow paths, and back-draft damper designs.

Table 2-1: Specifications of Series Terminal Units. (Furr et al. 2007)

Size	Terminal Unit	Fan Rated hp (W)	Primary Air Damper Type	Location of Induced Air Port
8 in. (203 mm)	S8A	¼ (187)	Butterfly	Parallel to Primary Inlet
	A8B	¼ (187)	Butterfly	Parallel to Primary Inlet
	S8C	¼ (187)	Opposing Blade	Side
12 in. (304 mm)	S12A	½ (373)	Butterfly	Parallel to Primary Inlet
	S12B	1/3 (249)	Butterfly	Parallel to Primary Inlet
	S12C	½ (373)	Opposing Blade	Side

Table 2-2: Specifications of Parallel Terminal Units. (Furr et al. 2007)

Size	Terminal Unit	Fan Rated hp (W)	Primary Air Damper Type	Backdraft Damper Style	Location of Backdraft Damper
8 in. (203 mm)	P8A	1/10 (75)	Butterfly	Primary Airflow Operated	In Primary Airstream
	P8B	1/6 (124)	Butterfly	Gravity Operated	Out of Primary Airstream
	P8C	¼ (187)	Butterfly	Gravity Operated	In Primary Airstream
12 in. (304 mm)	P12A	½ (373)	Butterfly	Primary Airflow Operated	In Primary Airstream
	P12B	¼ (187)	Butterfly	Gravity Operated	Out of Primary Airstream
	P12C	½ (373)	Butterfly	Gravity Operated	In Primary Airstream

Manufacturers produce FPTUs of various standard sizes, and quite often a manufacturer will use more than one terminal unit design in their product line. The current FPTU designs were not necessarily optimized to minimize internal losses. Current designs consist of square edges, sharp turns, and blunt flow control devices which can generate substantial internal losses. For example, one of the parallel units tested by Furr et al. (et al 2007) required almost 1 in w.g. (250 Pa) of static pressure to move the primary air through the terminal unit at peak cooling load conditions while other manufacturers' units had almost no measurable pressure drop for almost identical flow rates.

A system model that is based on the variations in currently manufactured designs could be developed and integrated into EnergyPlus building models. Due to the large number of permutations of FPTUs that are currently in production, it is impractical to fully investigate the performance of FPTUs with laboratory experiments alone. A computational fluid dynamics (CFD) model could be used to evaluate various FPTU designs as well as to investigate specific features of a particular unit design. A laboratory verified CFD model could also be used to evaluate whether or not a "generic" model based on design parameters would even be practical. No reference was found in the literature that any CFD models have been developed for FPTUs of any type.

The Navier-Stokes (NS) equations are the basis for solving problems in fluid mechanics that involve Newtonian fluids. Even after applying simplifying assumptions, exact solutions can only be found for flows that involve very simple geometries.

Numerical methods are required for flows that involve complex geometries even when dealing with incompressible fluids with constant properties.

Computational Fluid Dynamics (CFD) is the application of numerical methods to discretize and solve appropriately simplified versions of the Navier-Stokes (NS) equations. Typical CFD algorithms use finite difference, finite volume, or finite element techniques to model complex problems in fluid mechanics.

CFD has advanced to the point where commercially available software packages such as COMSOL, Fluent and Star CCM+ can be used by engineers to shorten the design cycle of new products or to improve the design of existing products without having to deal with the issues related to the numerical technique used to solve the equations.

By using existing commercially available programs, the engineer can focus on the design of the product and the interpretation of the output of the simulations without having to deal with the details of the programming related to the numerical method used to solve the discretized equations.

The weakness of the CFD approach is that since the output is only as good as the input, it is very easy for engineers to use a commercially available product to produce results that "look" reasonable but that contain significant errors. In many applications, laboratory measurements can be used to verify the accuracy of CFD models. When CFD is combined with targeted laboratory measurements, the quality of the CFD analysis is improved and the cost of experimentation can be reduced.

The objective in developing a CFD model for FPTUs was to show that the design process could be improved by the use of a commercially available product to perform accurate analysis of FPTUs. In order for the engineer to be able to effectively use CFD as design tool, significant model parameters needed to be identified and appropriate values quantified as they apply to fan powered terminal units.

This chapter focuses on a description of the development of a CFD model using a commercial product to analyze the operation of a FPTU. The development of a CFD model appropriate for use with FPTUs required the selection of a FPTU for study, a CFD software package, a computational technique, and the parameters that were appropriate for the equations that modeled the air flow through the terminal unit. Star CCM+ was chosen for this project but other programs such as Fluent or COMSOL could have been used.

The solution of the Navier-Stokes equations is a function of the properties of the fluid, the type of flow, and the geometry of the flow path. The geometry of the flow path was determined by the selection of the FPTU that was used as the basis for this study. The properties of the fluid were determined by using dry air at 20C and 101.7 kPa pressure. The knowledge of the type of flow was required so that the proper form of the NS equations would be used. The simulations were performed over a range of flow rates and the peak velocity of air entering the inlet air valve was 4,000 feet/min which was low enough that the flow was treated as incompressible. The flow was internal and the Reynolds number varied from a maximum of 389,000 at a velocity of 20 m/s to

minimum of 19,500 at a velocity of 1 m/s and the flow is turbulent over the full range of the operation of the units.

CHAPTER III

PARALLEL FPTU

This chapter focuses on a detailed description of the model of the operation of a zone controlled by both SCR and ECM parallel fan powered terminal units. The operation of the parallel FPTU (PFPTU) and its interaction with the system are covered in Chapter V which describes the system model.

Terminal unit description

Figure 3-1 shows the components in a parallel FPTU which consists of a primary air damper, flow sensor, induction port, fan, back draft damper, mixing chamber, and a supply air port that is connected by a duct to the conditioned space. When the fan is in operation, air is drawn into the fan through the induction port from the return air plenum and after it passes through the fan it is supplied into the mixing chamber.

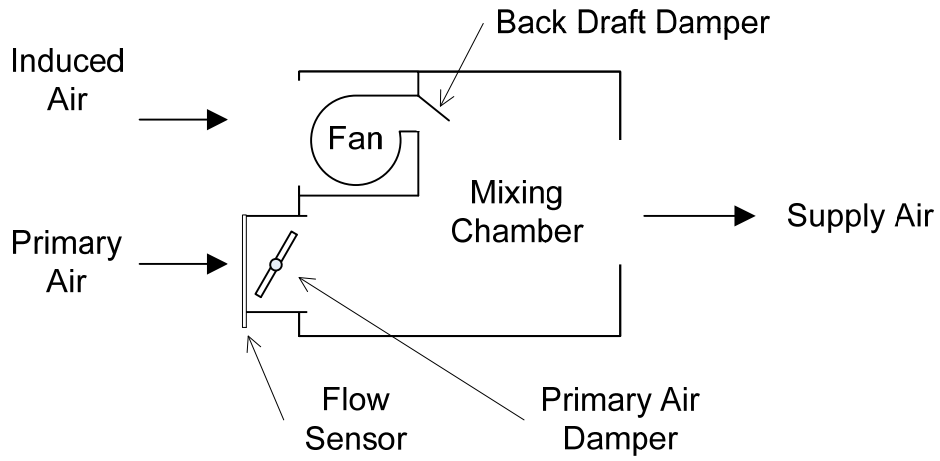

Figure 3-1: Parallel FPTU with fan oriented parallel to the primary air flow.

The primary air valve is an assembly that contains the flow sensor and the primary air damper. Primary air is supplied by a duct connected to the primary air stream and it passes through the primary air valve into the mixing chamber. All of the air that flows into the mixing chamber leaves the parallel FPTU through the supply port where it is delivered into the conditioned space. The air that leaves the supply port is called the "supply air."

The parallel terminal unit has two blower orientations consisting of parallel and perpendicular to the primary air inlet as shown in Figures 3-1 and 3-2. The arrangement chosen by a particular manufacturer is based on their opinion of the effectiveness of the mixing of the primary and induced air streams during fan operation.

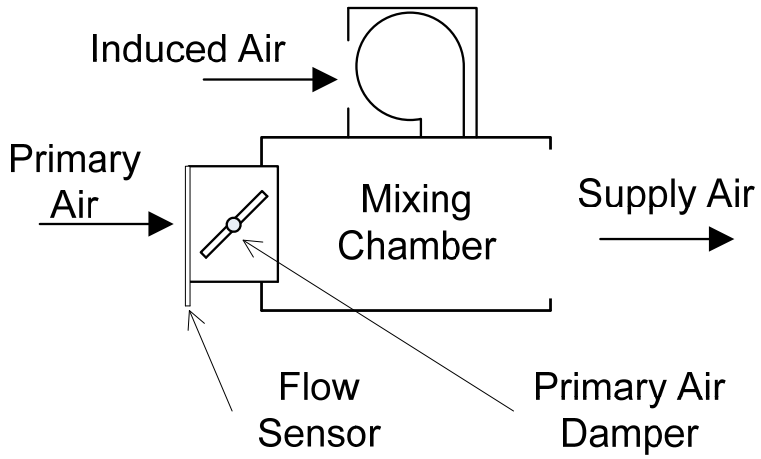

Figure 3-2: Parallel FPTU with fan oriented perpendicular to the primary air flow.

Background

One of the objectives of this research was to verify the accuracy of the model using laboratory experiments. For verification purposes the model had to predict the upstream static pressure, the downstream static pressure, the primary air flow rate, the primary air damper position and the induced air flow rate for a known space load. During the verification stage, the simulation program consisted of an Excel workbook that contained the inputs and outputs of the calculations in various spreadsheets within the workbook. The calculation procedures were developed as Visual Basic macros that were embedded in the programming modules within the workbook. The details of the model verification procedure and the experimental results can be found in a paper by Davis et al (2009). The model described in this chapter is based on the verified calculation procedure that was implemented as a Windows program written in C++. The C++ program was developed to facilitate the incorporation of the model into existing commercially available programs such as EnergyPlus.

The parallel fan powered terminal unit has two basic operating modes – fan-on and fan-off. Although the ECM control units can be used in a variable speed mode as an adjustable reheat mixing box, only the constant speed "on" or "off" fan operation is considered in this model.

The analysis of the operation of a zone required some of the parameters to be set by the user. For the parallel FPTU, these parameters consisted of the primary air temperature, T_p, primary air relative humidity, RH_p, the setpoint temperature of the

space, T_{sp}, the primary air leakage rate, L_p, and the minimum primary air flow rate, $\dot{Q}_{p,min}$, that must be delivered to the space.

The values used for this project were set based on recommendations from the advisory board of an industry consortium that helped fund the work. For the model the minimum primary air flow rate, $\dot{Q}_{p,min}$, was a variable and for this project it was set at 20% of design flow. The fan operating set point was also a variable and the fan was set up such that when it was operational, the induced air flow rate was 50% of the design flow. The 20% minimum primary plus the 50% return air from the fan totaled to 70% of the design flow rate when the fan was operating.

The primary air temperature, T_p, and primary air relative humidity, RH_p, were set at 55 F and 95% respectively. The setpoint temperature of the space, T_{sp}, was 78 F for both heating and cooling loads. The primary air leakage rate, L_p, was input during the simulation and was set at 10% (0.10) or 20% (0.20).

The operation of the parallel fan powered terminal unit changed dramatically once the fan was on. When a parallel FPTU is installed and setup by an HVAC contractor, the terminal unit fan speed is adjusted to the desired value and runs at a constant speed from that time forward whenever the fan is in operation. For cooling load operations, the fan does not run for a parallel terminal unit as long as the temperature in the zone can be maintained at the set point without adding supplemental heating. As the cooling load drops, the primary air flow rate is reduced to match the space sensible cooling load. The primary air flow rate can be reduced to a minimum flow rate that is determined by the need for fresh air to be supplied to the space.

When the space load dropped below the point where the terminal unit fan was activated the VAV terminal unit was operated as a constant volume device that supplied air to the conditioned space. When the fan was operational, the ratio of primary air to mixed air was essentially constant. The name "variable air volume" is derived from the variations in the amount of primary (conditioned) air that is supplied to the space during part load conditions that are above the minimum load levels that activate the terminal unit fan.

Terminal unit leakage

First documented by Furr et al. (2007) and later confirmed by Cramlet (2008) and Edmondson (2009), parallel terminal units leak during both fan-off and fan-on operation. Leakage is defined as the air that passes through the primary air valve into the mixing chamber but that does not pass through the supply port into the conditioned space. The source of the leaks includes the seams where the box components were joined together, penetrations in the unit to run wires, and the back draft damper that covers the fan port when the fan is off. The leaked air enters the return air stream without passing through the conditioned space. As a result of leakage, more primary air must be supplied to the terminal unit than is required to meet the space load. The net effect on the system is to increase the amount of air that must be handled by the primary fan, which increases the overall energy consumption of the system.

The primary air inlet valve entering air velocity differential pressure, P_{iav}, varies as a function of the flow rate of the primary air as it enters the FPTU. The leakage rate, $\dot{Q}_L$, was shown to be a function of the downstream static pressure, P_{down}, and the flow

rate sensor pressure, P_{iav}. The equation used to model the leakage rate was taken from Furr et al. (2007) and is shown in Equation 3-1. The coefficients for the ECM motors were taken from Edmonson (2009) and are presented in Table 3-1. The coefficients for the SCR controlled terminal units were taken from Cramlet (2008) and are presented in Table 3-2.

$$\dot{Q}_L = C_1 + C_2 P_{down} + C_3 P_{iav} \tag{3-1}$$

Table 3-1: Leakage coefficients for SCR parallel FPTU. (Furr et al. 2007)

FPTU	C1	C2	C3	R2
SCR_P8A	16.47	138.1	-6.16	0.97
SCR_P12A	14.4	97.94	-37.9	0.858
SCR_P8B	13.8	37.41	0	0.767
SCR_P12B	17.83	58.26	-27.16	0.945
SCR_P8C	16.86	77.55	-10.76	0.97
SCR_P12C	22.3	100.83	-15.02	0.989

Table 3-2: Leakage coefficients for ECM parallel FPTU. (Cramlet 2008 and Edmondson 2009)

FPTU	C1	C2	C3	R2
ECM_P8A	43.287	121.922	11.878	0.972
ECM_P12A	81.339	165.046	31.638	0.948
ECM_P8B	8.705	72.872	-4.472	0.887
ECM_P12B	15.997	78.834	-13.244	0.856
ECM_P8C-M1	37.87	119.98	3.213	0.918
ECM_P8C-M2	27.127	90.5	-4.985	0.895
ECM_P12C-M1	28.996	72.274	-6.628	0.927
ECM_P12C-M2	35.044	76.499	-4.948	0.826

The leakage rate was calculated by using equation 3-1 after the required amount of primary air needed to meet the space load was determined. Once the leakage flow rate and the primary air required for the space load were determined, then the primary leakage rate, L_P, as a decimal percent of the total primary flow rate was determined using equation 3-2.

$$L_p = \frac{\dot{Q}_L}{\dot{Q}_s + \dot{Q}_L} = \frac{\dot{Q}_L}{\dot{Q}_P} \tag{3-2}$$

The leakage rate was used in the calculations because it allowed the user of the parallel FPTU model to either use the results of the leakage model or to directly input a leakage rate which was convenient for investigating the sensitivity of the system model to the leakage rates of the FPTUs.

Calculations for the parallel FPTU when the fan is off

Figure 3-3 shows a flow chart of the algorithm used to model operation of the parallel VAV terminal unit and the zone supplied by the terminal unit. The following sections discuss the details of the calculation process as outlined in Figure 3-3.

The first step in the analysis was to determine whether or not the zone sensible space load was a cooling load. If the load was a cooling load, then the terminal unit fan was off and the supply air properties were the same as the primary air properties.

The supply air flow rate, $\dot{Q}_s$, that had to be delivered to the space to meet the cooling load was calculated using equation 3-3. When leakage was included, and the fan was off, the supply air flow was the primary air flow minus the leakage.

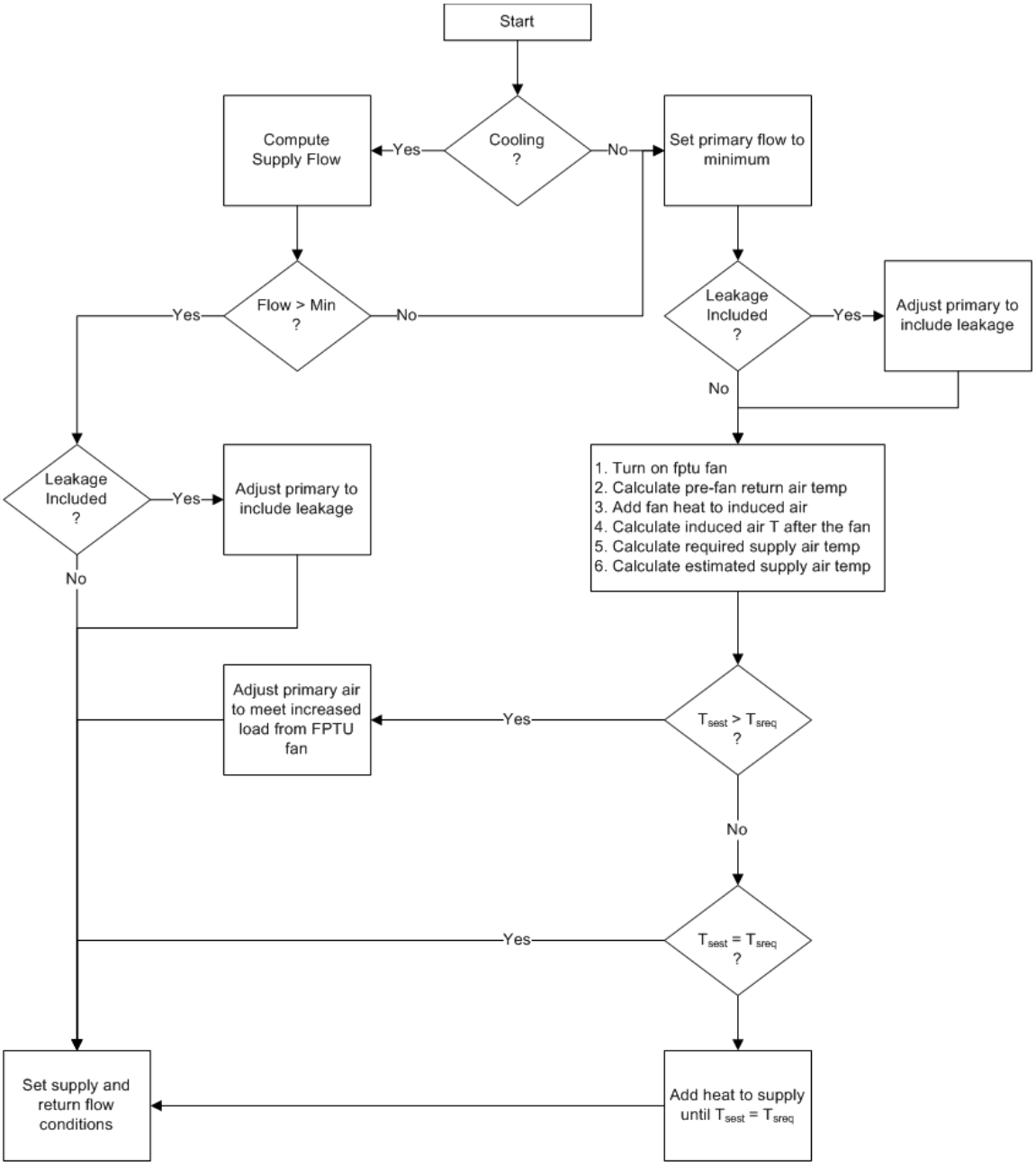

Figure 3-3: Flowchart of the Parallel FPTU operation.

When leakage was not included and the fan was off, the supply air flow was the same as the primary air flow. When leakage was included and the fan was on, the supply air flow was the primary air flow plus the induced air flow minus the leakage flow.

$$\dot{Q}_s = \frac{Q_{sen}}{C_s(T_{sp} - T_p)} \tag{3-3}$$

The setpoint temperature of the space, T_{sp}, was maintained by adjusting the primary air flow damper to modulate the amount of supply air, $\dot{Q}_s$, delivered to the space.

The properties for the return air were evaluated by performing an energy and mass balance on the return air duct. In all cases, the return air flow rate, $\dot{Q}_r$, was the same as the primary air flow rate, $\dot{Q}_p$. Equation 3-4 was used to calculate the mixed return air temperature and was based on an energy balance of the return air stream.

$$T_r = T_{sp} + L_p\left(T_p - T_{sp}\right) \tag{3-4}$$

If the primary air leakage rate, L_P, was zero, the return air temperature, T_r, was the same as the set point temperature, T_{sp}, for the space; otherwise, the return air temperature was lower than the setpoint temperature.

The latent space load was managed by assuming that the latent capacity of the primary air was sufficient at any specific sensible load. In a real system, the BEMS operator would control the latent capacity of the system by adjusting the chilled water

temperature of the primary cooling coil. Determining the proper chilled water setting was not considered as part of this model development.

The leaving coil conditions of dry-bulb temperature and relative humidity of the primary air were settings input by the user of the model and were used to calculate the humidity ratio of the primary air. The primary air entering the FPTU had the same properties as the primary air leaving the cooling coil.

The latent load of the space was combined with the humidity ratio of the supply air to calculate the humidity ratio of the return air. The zone return air humidity ratio, ω_r, was calculated using equation 3-5.

$$\omega_r = \omega_p + \frac{Q_{lat}}{C_{pl}\,\dot{Q}_p} \tag{3-5}$$

The calculated zone return air humidity ratio gave the moisture content of the air returned from the zone to the system air stream. The air flow rate used in equation 3-5 was the primary air flow rate, $\dot{Q}_p$, supplied for the zone.

If the supply air flow rate was above the minimum, then the primary flow rate was adjusted to account for leakage if it were included in the analysis. For the cooling load path, the final step was to compute the return air properties and any additional supply conditions such as the minimum static pressure.

Calculations for the parallel FPTU when the fan is on

For the case where the primary air flow rate was at or below the minimum, the analysis of the operation of FPTU proceeded along the path as if the unit were not in a

cooling mode. If the sensible load for the zone was not a cooling load, then the terminal unit was in heating mode, the terminal unit fan was turned on, and the analysis followed the "fan-on" operation.

Once the fan was turned on and the primary flow delivered to the space was set to the minimum, the downstream static pressure was calculated using equation 3-V-

$$P_{dwn} = K\left(\frac{\dot{Q}_s}{1000}\right)^2 \quad (3\text{-}6)$$

The "K" factor for the zone was calculated by using a user-defined downstream static pressure at peak air flow. Equation 3-6 was used to calculate the "K" factor for each zone at peak flow conditions which were defined by the user. The calculated "K" was then used at part load conditions to calculate the downstream static pressure, P_{dwn}.

Equation 3-6 required the flow rate of the terminal unit fan because the supply flow rate was the primary air flow plus the fan flow minus the leakage flow. Equation 3-7 developed by Furr et al. (2007) was used to calculate the flow rate of the fan. The coefficients for the SCR controlled motors are from Furr et al. (2007) and are presented in Table 3-3. The coefficients for the ECM motors are from Cramlet (2008) and Edmonson (2009) and are presented in Table 3-4.

$$\dot{Q}_f = C_1 + C_2V^2 + C_3V + C_4P_{dwn} + C_5P_{dwn} \quad (3\text{-}7)$$

Table 3-3: Fan flow coefficients for SCR Parallel FPTUs. (Furr et al. 2007)

FPTU	C1	C2	C3	C4	C5	R2
SCR_P8A	1108.5	0.028	-9.53	-516.9	-172.8	0.985
SCR_P12A	-1567.2	-0.0199	16.98	-407.4	-360.2	0.978
SCR_P8B	-988.5	-0.0197	11.85	-303	0	0.99
SCR_P12B	-1143	-0.0131	13.56	-364.8	0	0.998
SCR_P8C	-1725	-0.0328	19.79	-564.4	0	0.991
SCR_P12C	-2142.9	-0.0396	26.36	-1920.9	0	0.931

Table 3-4: Fan flow coefficients for ECM Parallel FPTUs. (Cramlet 2008 and Edmondson 2009)

FPTU	C1	C2	C3	C4	C5	R2
ECM_P8A	139.907	0.18	5.047	66.163	0	0.992
ECM_P12A	24.713	0.019	13.221	51.429	0	0.995
ECM_P8B	300.029	0.007	7.846	139.826	0	0.994
ECM_P12B	358.348	0.011	7.17	49.795	0	0.955
ECM_P8C-M1	-282.267	-0.13841	25.7991	-290.917	0	0.982
ECM_P8C-M2	40.273	-0.011	11.015	-111.869	0	0.979
ECM_P12C-M1	-206.123	-0.083	22.925	-122	0	0.99
ECM_P12C-M2	-53.466	-0.039	16.115	-272.663	0	0.987

After the downstream static pressure was determined, the fan power was calculated using equation 3-8 which was developed by Furr et al. (2007). The coefficients for 3-8 for the SCR motors are from Furr et al. (2007) and are presented in Table 3-5. The coefficients for the ECM motors are from Edmondson (2009) and are presented in Table 3-6.

$$\dot{W}_f = C_1 + C_2 V^2 + C_3 V + C_4 P_{dwn} + C_5 P_{iav} \quad (3\text{-}8)$$

Table 3-5: Fan power coefficients for SCR parallel FPTUs. (Furr et al. 2007)

FPTU	C1	C2	C3	C4	C5	R2
P8A	5.86	0.000895	0.304	-89.3	-31.9	0.908
P12A	-631	-0.0039	6.22	-142	0	0.956
P8B	-258	-0.006	3.65	-82.3	0	0.989
P12B	-403	-0.00515	5.15	-128.7	0	0.996
P8C	-363	-0.0088	5.18	-145	0	0.99
P12C	-622	-0.0159	9.48	-638	0	0.923

Table 3-6: Fan power coefficients for ECM parallel FPTUs. (Cramlet 2008 and Edmondson 2009)

FPTU	C1	C2	C3	C4	C5	R2
P8A	11.698	0.025	-0.919	203.915	0	0.953
P12A	3.345	0.06	-1.987	358.335	0	0.922
P8B	11.463	0.036	-0.35	245.189	0	0.99
P12B	29.067	0.042	-0.521	196.659	0	0.955
P8C-M1	-202.61	-0.041	9.994	-8.424	0	0.919
P8C-M2	55.736	0.074	-3.739	172.102	0	0.943
P12C-M1	-59.413	0.027	1.347	167.824	0	0.977
P12C-M2	22.523	0.043	-1.318	114.355	0	0.976

Equation 3-9 was developed by Furr et al. (2007) and was used to calculate the value of P_{iav} in equations 3-7 and 3-8. The coefficients for the SCR parallel FPTUs are from Furr et al. (2007) and are presented in Table 3-7. The coefficients for the ECM parallel FPTUs are from Edmondson (2009) and are presented in Table 3-8.

$$P_{iav} = C_1 + C_2 \dot{Q}_p \tag{3-9}$$

Table 3-7: P_{iav} coefficients for SCR parallel FPTUs. (Furr et al. 2007)

Name	C_1[in. w.g.]	C_2[in. w.g./CFM]
P8A	-0.19	0.00109
P8B	-0.13	0.000749
P8C	-0.149	0.000816
P12A	-0.168	0.000438
P12B	-0.0991	0.000277
P12C	-0.109	0.000279

Table 3-8: P_{iav} coefficients for ECM parallel FPTUs. (Cramlet 2008 and Edmondson 2009)

Name	C_1[in. w.g.]	C_2[in. w.g./CFM]
P8A	-0.19	0.00109
P8B	-0.13	0.000749
P8C	-0.149	0.000816
P12A	-0.168	0.000438
P12B	-0.0991	0.000277
P12C	-0.109	0.000279

In equations 3-7 and 3-8 the term "V" refers to the "voltage" applied to control the terminal units. In the case of the SCR motors, "V" refers to the SCR output voltage which ranged from 0 – 277 VAC. For the ECM motors "V" meant either a control voltage of 0 – 10 VDC or a controller setting of 0 – 100%. Edmondson (2009) details the variations in the use of the voltage (V) as it relates to the equations. For the model,

the user inputs a flow rate of 0 – 100% in the FPTU setup portion of the user interface and the software automatically converts to the proper "V" range for the calculations.

The fan power, $\dot{W}_f$, in Watts was added to the return air inducted into the fan and the temperature of the air supplied to the mixing chamber by the fan, T_f, was computed:

$$T_f = T_r + \frac{3.413\dot{W}_f}{C_s\dot{Q}_f} \tag{3-10}$$

where 3.413 was the factor used to convert from Watts to BTUs/hr. To determine the supply temperature, T_s, a mass and energy balance was performed on the FPTU mixing chamber. Figure 3-4 shows the parallel FPTU air flow path with the mixing chamber outlined as the control volume.

A mass balance on the mixing chamber control volume yielded:

$$\dot{m}_f + \dot{m}_p = \dot{m}_s + \dot{m}_L \tag{3-11}$$

where:

$$\dot{m} = \rho\dot{Q} \tag{3-12}$$

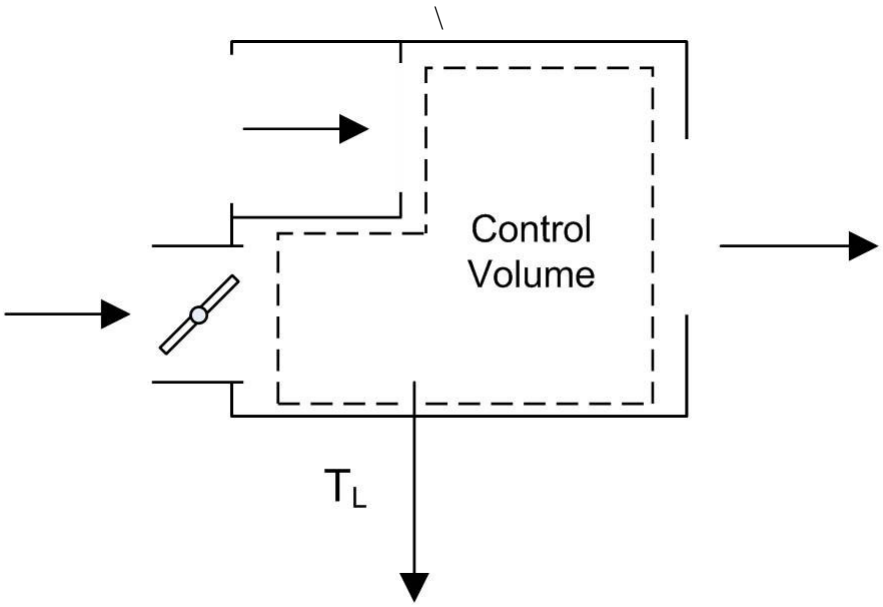

Figure 3-4: Control volume of the parallel unit after the fan was turned on.

Assuming constant density and combining equation 3-11 with 3-12:

$$\dot{Q}_f + \dot{Q}_p = \dot{Q}_s + \dot{Q}_L \tag{3-13}$$

An energy balance on the control volume yields:

$$\dot{m}_f C_p T_f + \dot{m}_p C_p T_p = \dot{m}_s C_p T_s + \dot{m}_L C_p T_L \tag{3-14}$$

With the assumption that the entering air streams mix completely, the temperature of the supply air and the leakage air must be equal which means that $T_L = T_s$. If the density

and specific heats of the air are assumed constant, then equations 3-12 and 3-14 can be combined to yield:

$$\dot{Q}_f T_f + \dot{Q}_p T_p = (\dot{Q}_s + \dot{Q}_L) T_S \tag{3-15}$$

Combining equation 3-15 with 3-12 and solving for T_s yields an equation that can be used to calculate the estimated supply air temperature, T_{sest}.

$$T_{sest} = \frac{\dot{Q}_p T_p + \dot{Q}_f T_f}{\dot{Q}_p + \dot{Q}_f} \tag{3-16A}$$

The pre-fan return air temperature, T_r, was required by equation 3-10. When the fan was on and leakage was included, an energy and mass balance was required to solve for the return air temperature. Equation 3-16B was derived using a mass and energy balance on the return air control volume. The temperature of the supply air and the temperature of the pre-fan return air, T_r, were estimated using a procedure that iterated through equations 3-16A and 3-16B until both the supply temperature and the pre-fan return air temperature changed by less than 0.01 F from one iteration to the next.

$$T_r = \frac{\dot{Q}_l T_m + \dot{Q}_s T_{sp}}{\dot{Q}_p + \dot{Q}_f} \tag{3-16B}$$

Once the estimated supply air temperature, T_{sest}, was known it was compared to the supply air temperature required to maintain space conditions, T_{sreq}. The required supply temperature, T_{sreq}, was calculated using the sensible heat equation, equation 1-1, to solve for T_{sreq} where the sensible heat transfer was the summation of the space load and the cooling delivered to the space by the minimum primary air setting supplied by the user.

If the estimated temperature was above the required temperature, then the primary air flow rate was adjusted (increased) to handle the extra heat provided by the terminal unit blower motor. The simulation then proceeded to the final step of calculating return air conditions and the minimum static pressure.

If the estimated supply air temperature was below the required supply air temperature, then heat energy was added to increase the supply temperature to the required value. At this point the simulation proceeded to calculate return air conditions and the minimum static pressure.

Static pressure calculations – minimum static pressure

The advantage of VAV systems is the ability to reduce fan power as a result of the reduced air flow requirements at part load conditions. When the flow rate decreases, there is a related drop in the amount of static pressure required to move the primary air through the system and to deliver the air to the space. To be able to optimize the operation of the system, it would be valuable to know the minimum static pressure requirement for each of the zones. With this information, the operator could reduce the

primary fan speed to supply the proper air flow at the minimum pressure required by the system.

The procedure for estimating the minimum required static pressure consisted of using the previously described process to determine the required amount of primary air flow to meet the space loads and the amount of air supplied to the space. Once the primary air flow rate and the supply air flow rates were known, the minimum static pressure could be calculated.

Equation 3-17 developed by Furr et al. (2007) can be used to calculate the flow rate for the primary air for both the SCR and ECM FPTUs for a given damper setting and differential pressure. The coefficients for SCR parallel FPTUs were from Furr et al. (2007) and are presented in Table 3-9. The coefficients for ECM parallel FPTUs were from Cramlet (2008) and Edmondson (2009) and are presented in Table 3-10.

$$\dot{Q}_p = C_1(1 + C_2S + C_3S^2)\sqrt{\Delta P} \qquad (3\text{-}17)$$

Table 3-9: Primary air flow coefficients for SCR Parallel FPTUs. (Furr et al. 2007)

FPTU	C1	C2	C3	R2
SCR_P8A	1363	-2.02E-02	9.87E-05	0.924
SCR_P12A	7425	-3.07E-02	2.45E-04	0.935
SCR_P8B	1935	-2.48E-02	1.91E-04	0.981
SCR_P12B	5781	-2.77E-02	2.04E-04	0.935
SCR_P8C	1594	-2.73E-02	1.91E-04	0.981
SCR_P12C	1838	-1.16E-02	1.63E-05	0.637

Table 3-10: Primary air flow coefficients for ECM Parallel FPTUs. (Cramlet 2008 and Edmondson 2009)

FPTU	C1	C2	C3	R2
ECM_P8A	1380	-2.03E-02	8.90E-05	0.982
ECM_P12A	3868	-1.54E-02	3.27E-05	0.961
ECM_P8B	2212	-2.71E-02	1.89E-04	0.988
ECM_P12B	6528	-2.84E-02	2.06E-04	0.872
ECM_P8C-M2	1469	-2.35E-02	1.38E-04	0.975
ECM_P8C-M1	1671	-2.53E-02	1.71E-04	0.978
ECM_P12C-M1	3380	-2.25E-02	1.22E-04	0.96
ECM_P12C-M2	3747	-2.98E-02	2.27E-04	0.969

The pressure differential is calculated by using a binary search algorithm for the ΔP needed to calculate the $\dot{V}_p$ required to meet space conditions. The minimum static pressure requires that the damper be in a fully open position so the value of "S" was zero (0) degrees for this calculation. Once ΔP was determined, the downstream static pressure was calculated using equation 3-16 (if it had not already been calculated). The upstream static pressure was determined by adding ΔP to the downstream static pressure.

The performance of the system was a function of the operating characteristics of the zones. Figure 3-5 shows the primary air flow rate and the upstream static pressure as a function of the space load from maximum heating to maximum cooling for a parallel FPTU. The primary air flow rate is the amount of primary air that is required to provide the proper supply temperature to maintain space conditions.

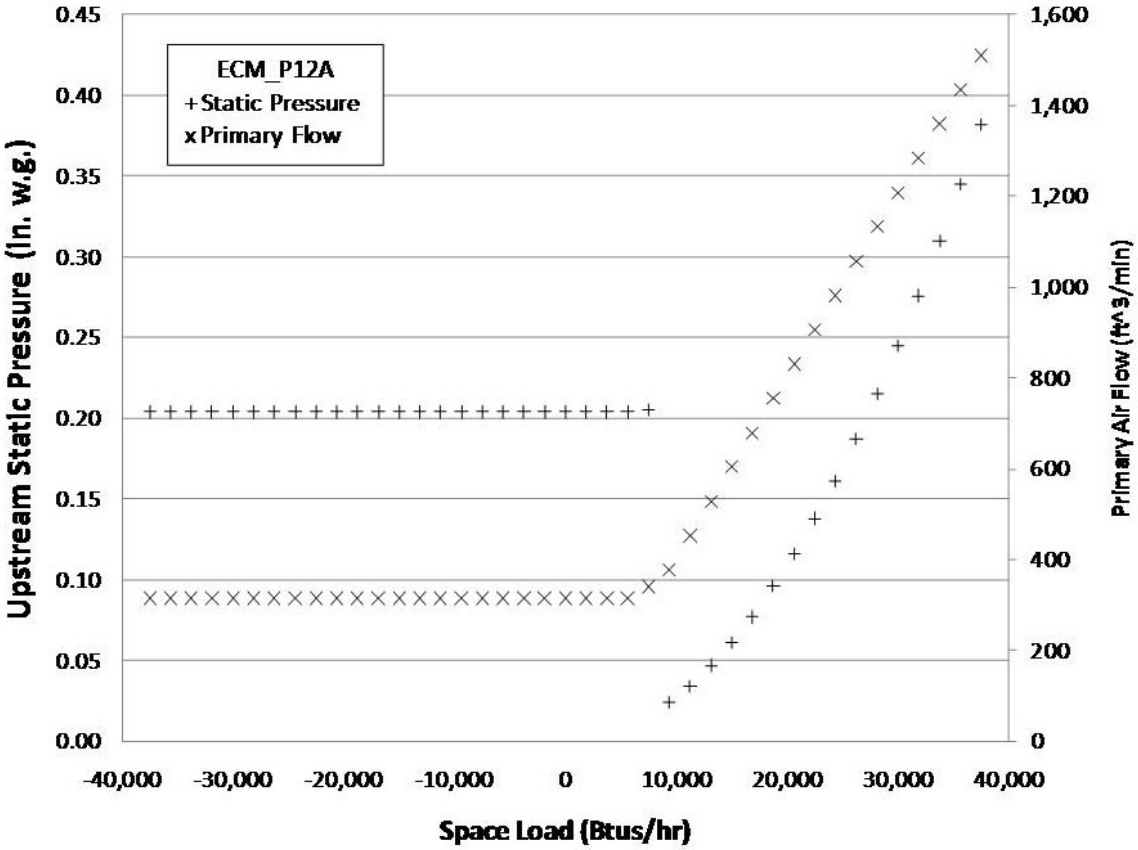

Figure 3-5: Parallel primary air flow and static pressure vs. space load.

Figure 3-5 shows that the upstream static pressure for the parallel terminal unit drops with the space loads but that it jumps to almost full-load levels when the terminal unit fan is in operation. The increase in the upstream static pressure at low-load conditions causes a system-wide increase in the available upstream static pressure for all zones.

Harmonics

Modeling the detailed harmonic distortions would have required a detailed analysis of the various frequencies present in the building when the terminal unit fan was in operation and it would have required the same analysis at each operating point of both

speed and load. Edmondson (2009) showed that a more practical approach was to look at the Total Harmonic Distortion (THD) of various electrical signals that were of interest due to their impact on the building electrical system.

The items of interest for this project were the THD for real power, current, voltage, and the Triplen currents and their impact at the point of common coupling (PCC). The PCC is the point in the electrical system where the power is distributed to the equipment. In a building this could be at the power distribution panel that handles the equipment tied to an air-handling unit, such as a power distribution panel, or a motor control center. The PCC may also be the point where power is supplied to the entire facility.

Although not previously reported, Edmondson (2009) measured the power factor for parallel ECM FPTU and the average values are presented Table 3-11 along with the average current THD (%) (Edmondson 2009).

Table 3-11: Power factor and Current THD (%) for parallel ECM FPTUs. (Edmondson 2009)

	THD_i[%]	PF
P8A	90.4	0.42
P8B	90.0	0.45
P8C-M2	86.1	0.50
P12A	148.2	0.52
P12B	87.3	0.44
P12C-M1	177.1	0.49
P12C-M2	149.1	0.53

The voltage THD at the PCC was calculated at the system level and required the harmonic currents from zones. Measurements taken by Edmondson (2009) provided harmonic currents as a percentage of the fundamental current, I_1. The data from Edmondson (2009) was used to calculate average harmonics ratios for parallel FPTUs and is presented in Table 3-12. The procedure for calculating the THD at the PCC was included in Chapter V which described the system model.

Table 3-12: Harmonic current multiplication factors, I_n/I_1, in percent (%) for parallel ECM FPTU derived from measurements by Edmondson. (Edmondson 2009)

	P8A	P8B	P8C-M2	P12A	P12B	P12C-M1	P12C-M2
2	4.5	3.6	2.8	2.7	3.6	3.4	3.0
3	92.2	93.3	87.4	91.3	93.2	90.4	86.1
4	5.2	3.5	2.4	2.9	3.8	2.7	2.3
5	86.3	86.7	78.7	81.5	86.5	81.4	76.1
6	6.4	4.1	2.7	3.0	4.3	2.8	2.2
7	79.7	78.5	67.2	68.4	77.9	70.1	63.3
8	8.0	5.4	3.1	3.1	5.3	2.9	2.0
9	70.8	68.1	53.6	52.6	67.3	57.1	46.7
10	9.8	7.0	4.0	2.9	6.6	2.9	1.9
11	61.0	56.8	39.7	37.9	56.6	45.8	33.2
12	11.7	8.9	5.4	2.6	8.0	2.8	1.7
13	51.4	45.9	27.4	24.3	46.9	35.5	19.7
14	13.5	10.8	6.9	2.2	9.5	2.6	1.5
15	42.4	35.8	18.2	14.7	38.5	28.1	11.0
16	15.3	12.5	8.7	1.8	10.8	2.3	1.2
17	33.8	27.1	13.0	10.2	31.7	22.6	9.3
18	16.2	13.5	9.7	1.4	11.6	1.9	1.0
19	27.2	20.9	12.8	9.7	26.6	18.4	10.4
20	16.9	14.1	10.5	1.1	12.1	1.6	0.9
21	22.6	17.3	13.5	9.8	22.3	14.8	10.9
22	16.3	13.7	9.5	0.9	11.7	1.4	0.8
23	19.6	15.5	13.2	9.3	18.8	11.8	10.0
24	16.7	13.6	10.6	0.8	11.5	1.3	0.6
25	18.5	14.7	12.5	7.8	16.1	9.5	7.6

The value of the currents for the first twenty-five harmonics were calculated at the zone level by using the multipliers in Table 3-12 in equation 3-18. The current at each frequency was stored and returned as information for use by the system level calculations.

$$I_n = \frac{{}^{I_n}/_{I_1}}{100} I_1 \tag{3-18}$$

I_{rms} was calculated with equation 3-19 using the power consumed by the FPTU and the average power factor from Table 3-12.

$$I_{rms} = \frac{P}{V_{rms} PF} \tag{3-19}$$

For this analysis, V_{rms} is the same as the fundamental harmonic voltage, V_1, and was a user input. For the simulations, 277 V was used because it is a common line voltage used in commercial buildings in the United States and it was the line voltage used during the laboratory testing.

I_1 was calculated with equation 3-20 using I_{rms} and the current THD from Table 3-12.

$$I_1 = \frac{I_{rms}}{\sqrt{1+THD_I{}^2}} \tag{3-20}$$

The value for the triplen currents from a parallel ECM FPTU were calculated using equation 3-21 using the multipliers presented in Table 3-13 which were derived from measurements made by Edmondson (2009).

$$I_{Ti} = M_i I_1 \tag{3-21}$$

In equation 3-21 I_{Ti} is the triplen current at a specific harmonic and M_i is the multiplier from Table 3-13. The total triplen current is the summation of the four harmonics which from Table 3-13 is $I_{TT} = 1.93I_1$.

Table 3-13: Multipliers for estimating the triplen current for parallel ECM FPTU.

Triplen	%
3	91
9	59
15	27
21	16

CHAPTER IV

SERIES FPTU

This chapter focused on a detailed description of the model of the operation of a zone controlled by both SCR and ECM series fan-powered terminal units. The operation of the series FPTU and its interaction with the system were covered in Chapter V which describes the system model.

Terminal unit description

Figure 4-1 shows the components in a series FPTU, which consisted of a primary air damper, flow sensor, induction port, mixing chamber, fan, and a supply air port that was connected by a duct to the conditioned space.

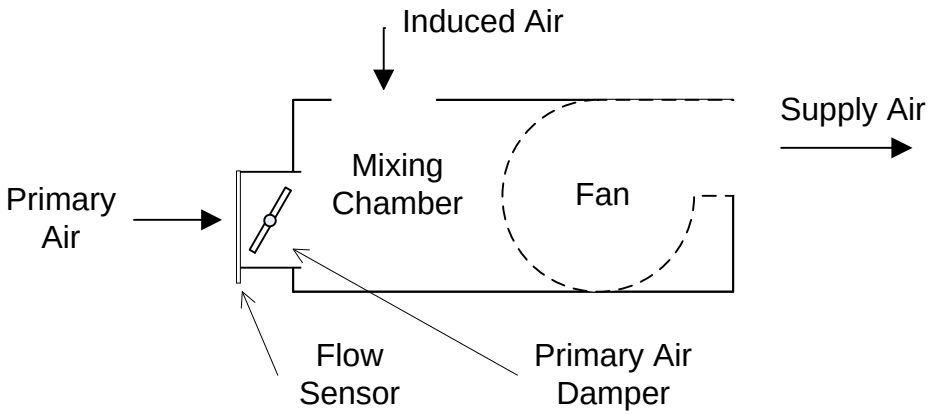

Figure 4-1: Typical configuration of a Series FPTU.

When the space conditions were actively being controlled by the series FPTU, the fan was always in operation. The primary air valve contains the flow sensor and the

primary air damper. Primary air was supplied by a duct connected to the primary air stream and it passed through the primary air valve into the mixing chamber. When the fan drew more air from the mixing chamber than was supplied by the primary air valve, then return air was inducted into the mixing chamber from the return air stream along with the air supplied by the primary air valve. All of the air that flowed into the mixing chamber passed through the fan into the supply port where it was delivered into the conditioned space. The air that leaves the supply port was called the "supply air."

When an SCR series terminal unit was installed, the fan speed was set so that the supply air flow rate was sufficient to handle the peak primary air flow rate that was required to meet the peak space load plus the heat load from the terminal unit fan. Once the fan speed was set, the series FPTU operated as a CAV unit that provided a fixed flow rate of supply air. Space conditions were maintained by adjusting the temperature of the supply air. The new ECM series FPTU have the ability to operate as true VAV FPTUs but for this project only the CAV operation was modeled.

Background

One of the objectives of the research was to verify the accuracy of the model using laboratory experiments. For verification purposes, the model had to predict the upstream static pressure, the primary air flow rate, the primary air damper position and the induced air flow rate for a known space load with a fixed downstream static pressure. During the verification stage, the simulation program consisted of an Excel workbook that contained the inputs and outputs of the calculations in various spreadsheets within the workbook. The calculation procedures were developed as Visual Basic macros that

were embedded in the programming modules within the workbook. The ECM FPTUs were tested after the models were verified using experimental data from Furr et al. (2007).

The details of the model verification procedure and the experimental results can be found in a paper by Davis et al (2009). The model described in this chapter is based on the verified calculation procedure that was implemented as a Windows program written in C++. The C++ program was developed to facilitate the incorporation of the model into existing commercially available programs such as EnergyPlus. The verification process was done using measurements from SCR FPTUs. The verified procedure was used to model both SCR and ECM FPTUs.

When the series fan powered terminal unit was actively controlling a zone, the fan was always on and it had two basic operating modes – variable air volume and constant air volume. The VAV mode applied only to ECM-controlled units and was a recent innovation that was introduced after the model verification process was completed. Although the VAV mode was added to the model, it was not verified or included in this dissertation. This dissertation included only a description of the verified CAV-operating mode for ECM and SCR series FPTUs.

The analysis of the operation of a zone required some of the parameters to be set by the user. For the series FPTU, these parameters consisted of the primary air temperature, T_p, primary air relative humidity, RH_p, the setpoint temperature of the space, T_{sp}, the downstream static pressure, P_{dwn}, and the minimum primary air flow rate, $\dot{Q}_{p,min}$, that

must be delivered to the space. The user had to specify the fan flow settings and once they were set, the fan speed, supply air flow and fan power were constant.

The values used for this project were based on recommendations from the advisory board of an industry consortium that helped fund the work. For the model, the minimum primary air flow rate, $\dot{Q}_{p,min}$, was a variable and for this project it was set at 20% of design flow.

The primary air temperature, T_p, and primary air relative humidity, RH_p, were set at 55 F and 95%, respectively. The setpoint temperature of the space, T_{sp}, was 78 F for both heating and cooling loads and the downstream static pressure was a constant 0.25 in. w.g. for all operating conditions.

CAV mode setup and operation

When a CAV series FPTU is installed and setup by an HVAC contractor, the terminal unit fan speed is adjusted to the desired value and runs at a constant speed from that time forward whenever the fan is in operation. It was shown by Furr et al. (2007), Cramlet (2008) and Edmondson (2009) that when series FPTUs are operated at a constant speed they supply a constant volume of air to the space over the operating range of the terminal unit for both the speed of the motor and the range of damper settings used to control the supply temperature.

For cooling load operation, the temperature in the zone was maintained at the set point without adding supplemental heating by adjusting the primary air flow which changes the supply air temperature. As the cooling load drops, the primary air flow rate is reduced to match the space sensible cooling load. The primary air flow rate can be

reduced to a minimum flow rate that is determined by the need for fresh air to be supplied to the space.

Furr et al. (2007) demonstrated that the fan flow for a series FPTU was a function of the fan motor speed and the flow rate of the primary air that entered the mixing chamber expressed as a velocity pressure, P_{iav}, across the inlet flow sensor. The speed of the motor was expressed as a function of the control voltage (V). For SCR motors, V varied from 0 – 277 V. For ECM motors, V varied from 0-10 V DC. For the model, the user input the fan speed as a percentage of the full speed and the algorithms automatically adjusted for the type of FPTU used by the zone.

For the series FPTUs, the supply air flow, $\dot{Q}_s$, is the same as the fan air flow, $\dot{Q}_f$, and was calculated using equation 4-1 which was developed by Furr et al. (2007).

$$\dot{Q}_s = \dot{Q}_f = C_1 + C_2V^2 + C_3V + C_4P_{iav} \quad (4\text{-}1)$$

The coefficients for the SCR-controlled motors were developed by Furr et al. (2007) and are presented in Table 4-1. The coefficients for the ECM series FPTUs were developed by Edmondson (2009) and are presented in Table 4-2.

Table 4-1: Fan flow coefficients for SCR Series FPTUs. (Furr et al. 2007)

FPTU	C1	C2	C3	C4	C5	R2
SCR_S8A	-1776	-0.0228	16.49	0.0036	0	0.989
SCR_S12A	-778.5	0.0091	6.918	0.0394	0	0.993
SCR_S8B	-1705	-0.0254	18.15	-0.0448	0	0.994
SCR_S8C	-1310	-0.0183	13.94	0.0677	0	0.997
SCR_S12C	-1903	-0.0105	16.78	0.0812	0	0.99

Table 4-2: Fan flow coefficients for ECM Series FPTUs. (Edmondson 2009)

FPTU	C1	C2	C3	C4	C5	R2
ECM_S8A	58.918	0.016	8.502	6.602	0	0.987
ECM_S12A	148.921	0.025	20.236	43.5	0	0.996
ECM_S8B	-90.795	-0.052	21.411	20.123	0	0.991
ECM_S12B	375.117	0.015	11.587	-32.312	0	0.993
ECM_S8C-M1	108.301	0.0113	12.2977	12.441	0	0.997
ECM_S8C-M2	-82.18	-0.043	18.18	34.252	0	0.992
ECM_S12C-M1	467.397	0.025	15.48	26.097	0	0.995
ECM_S12C-M2	67.426	-0.00079	21.47	75.604	0	0.997

Calculations for the series FPTU when in CAV mode

Figure 4-2 shows a flow chart of the algorithm used to model operation of the series FPTU when operated in the CAV mode. The following sections discuss the details of the calculation process as outlined in Figure 4-2.

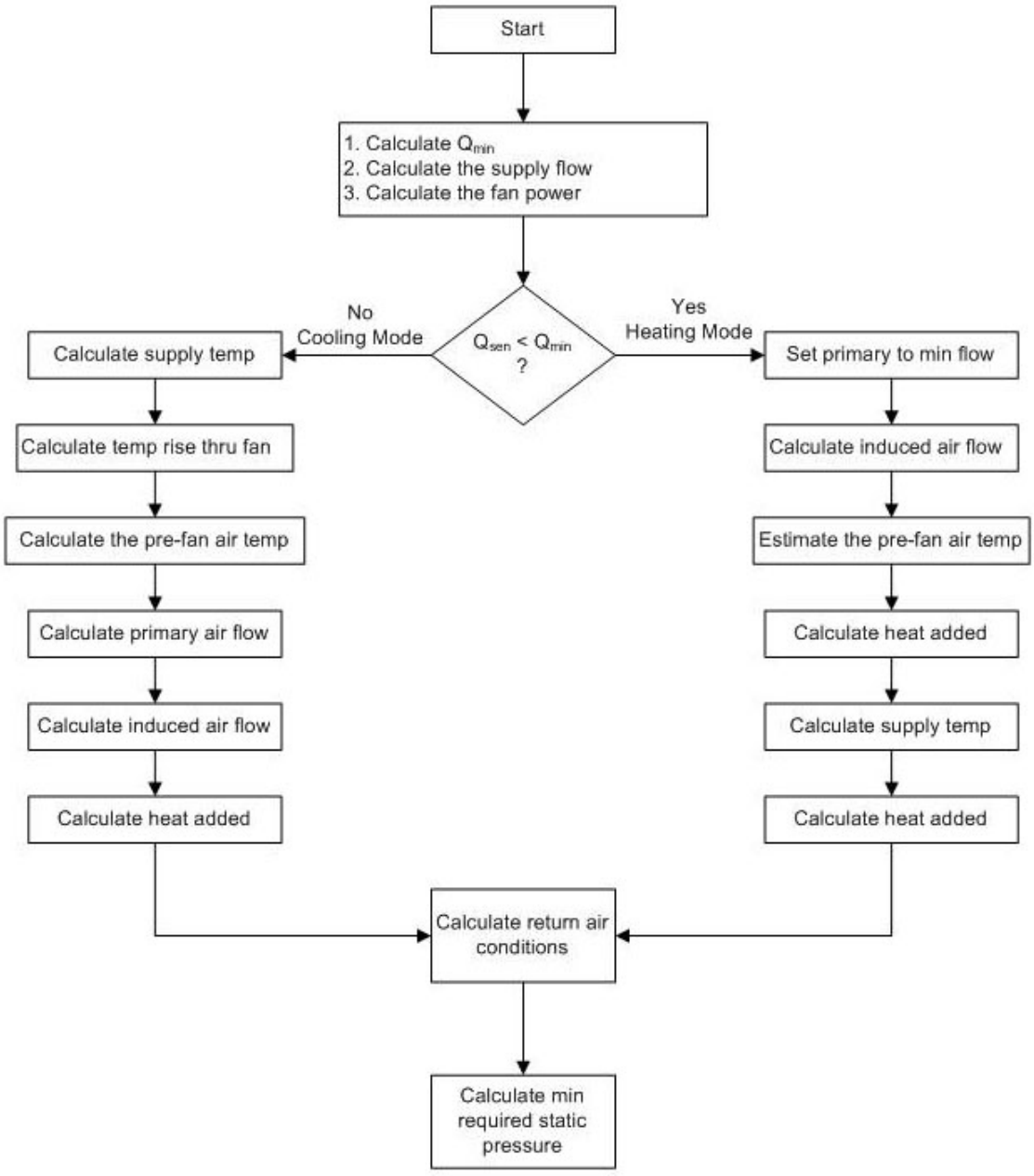

Figure 4-2: Flowchart of the Series FPTU operation.

One of the energy-saving strategies for the series FPTU was to turn the unit off if the space was not actively controlled. The process diagram shown in Figure 4-2 applies when the zone is in an operating mode and the space conditions are actively controlled by the building energy management system.

Since the supply air flow was both fixed and known for all operating conditions, the first step in the analysis was to use equation 4-1 to calculate the supply flow rate from the user inputs and to use equation 4-2 to calculate the power consumed by the fan, $\dot{W}_f$.

Equation 4-2 was developed by Furr et al. (2007). The coefficients for the SCR motors are from Furr et al. (2007) and are presented in Table 4-3. The coefficients for the ECM motors are from Edmondson (2009) and are presented in Table 4-4. As with equation 4-1, V varies from 0n to 277 Volts AC for the SCR controlled FPTUs and 0 – 10 Volts DC for the ECM controlled FPTUs.

$$\dot{W}_f = C_1 + C_2V^2 + C_3V + C_4P_{dwn} + C_5P_{iav} \quad (4\text{-}2)$$

Table 4-3: Fan power coefficients for SCR Series FPTUs. (Furr et al. 2007)

FPTU	C1	C2	C3	C4	C5	R2
SCR_S8A	-732.7	-0.0114	7.13	-2.12	0	0.989
SCR_S12A	-269.4	0.00854	1.8	19.05	0	0.997
SCR_S8B	-595.7	-0.0111	6.96	-13.25	0	0.983
SCR_S12B	125.9	0.00534	0.736	-16.36	0	0.87
SCR_S8C	-455.5	-0.00817	5.32	1.91	0	0.994
SCR_S12C	-917	-0.0129	9.86	97.73	0	0.99

Table 4-4: Fan power coefficients for ECM Series FPTUs. (Edmondson 2009)

FPTU	C1	C2	C3	C4	C5	R2
ECM_S8A	70.343	0.049	-2.602	2.338	0	0.968
ECM_S12A	197.65	0.161	-9.589	24.376	0	0.989
ECM_S8B	8.89	0.061	-0.221	21.258	0	0.985
ECM_S12B	112.278	0.074	-3.657	-31.915	0	0.978
ECM_S8C-M1	78.998	0.07045	-3.1497	-12.993	0	0.998
ECM_S8C-M2	46.608	0.045	-1.165	-4.711	0	0.993
ECM_S12C-M1	145.834	0.111	-4.31	-45.401	0	0.998
ECM_S12C-M2	179.663	0.131	-7.303	-18.473	0	0.996

The next step in the analysis was to use equation 4-3 to calculate the minimum amount of cooling, Q_{min}, that was supplied to the space at minimum primary flow, $\dot{Q}_{pmin}$. The minimum primary flow was calculated by using the minimum flow setting that was input by the user of the simulation program. For this project, the minimum primary flow a rate was 20% of the cooling design flow rate as per the recommendation from the industry advisory board. The design flow rate was also a user input and was based on the design cooling (primary flow rate) capacity of the FPTU as per the manufacturer's specifications for the FPTU.

$$Q_{min} = C_s \dot{Q}_{pmin}(T_{sp} - T_p) \tag{4-3}$$

The sensible space load, Q_{sens}, that was supplied by the building loads simulation (DOE2) was then compared to Q_{min} and if it was lower, then the zone was in heating mode, otherwise the zone was in cooling mode.

Calculations for the series FPTU when in heating mode

When in heating mode, the primary air flow, $\dot{Q}_p$, was set to the minimum flow rate and the induced air flow, $\dot{Q}_{ind}$, was calculated by subtracting the primary flow, $\dot{Q}_p$, from the supply flow rate, $\dot{Q}_s$. After the induced air flow was calculated, a mass and energy balance on the mixing chamber was done and the pre-fan mixed-air temperature was calculated using equation 4-4.

$$T_{pfest} = \frac{\dot{Q}_p T_p + \dot{Q}_{ind} T_p}{\dot{Q}_s} \tag{4-4}$$

After the pre-fan temperature was calculated, the heat added to maintain space conditions was calculated using equation 4-5.

$$Q_{aux} = Q_{min} - Q_{sens} \tag{4-5}$$

The estimated supply temperature was then calculated using equation 4-V-

$$T_s = T_{pfest} + \frac{Q_{aux} + 3.412\dot{W}_f}{C_{ps}\dot{Q}_s} \tag{4-6}$$

In 4-6, C_s was the constant that related sensible heating or cooling to temperature on an hourly rate basis as defined in Chapter I and Appendix I. The constant 3.412 was the constant used to convert Watts to BTUs per hour. The return air conditions were then

calculated where the return air temperature was the same as the space setpoint temperature and the return air humidity ratio was calculated using equation 4-7.

$$\omega_r = \omega_p + \frac{Q_{lat}}{C_{pl}\,\dot{Q}_p} \tag{4-7}$$

In 4-7, C_{pl} was the constant that related change in moisture in the air and the flow rate in ft^3/min to the heat transfer in BTUs/hr as defined in Chapter I and Appendix I.

Calculations for the series FPTU when in cooling mode

The first task in cooling mode was to calculate the required supply temperature using equation 4-8.

$$T_s = T_{sp} - \frac{Q_{sen}}{C_s\,\dot{Q}_s} \tag{4-8}$$

The required pre-fan, mixed air temperature was calculated using equation 4-9.

$$T_{rpf} = T_s - \frac{3.412\dot{W}_f}{C_s\dot{Q}_s} \tag{4-9}$$

After the required pre-fan mixed air temperature was calculated, the amount of primary air that was required to obtain the correct pre-fan mixed air temperature was calculated using equation 4-10.

$$\dot{Q}_p = \left(\frac{T_{rpf} - T_{sp}}{T_p - T_{sp}}\right) \dot{Q}_s \quad (4\text{-}10)$$

When equation 4-10 was derived, the temperature of the return air, T_r, was considered to be equal to the space temperature, T_{sp}, because in all operating cases the supply air temperature was adjusted to meet the space load for both heating and cooling modes which resulted in a return air temperature that is the same as the space setpoint temperature.

After the primary air flow was calculated, the induced air was calculated by subtracting the primary air flow from the supply air flow. For the case where the zone was in cooling mode, the supply temperature and humidity conditions were known and the return air humidity ratio, ω_r, was calculated using equation 4-7 and the return air flow was the same as the primary air flow.

Pressure calculations – minimum static pressure

One advantage of VAV systems is the ability to reduce fan power as a result of the reduced air flow requirements at part-load conditions. When the flow rate decreases, there is a related drop in the amount of static pressure required to move the primary air through the system and to deliver the air to the space. The static pressure requirement for the zone was defined as the static pressure required at the inlet of the primary air valve to move the air through the FPTU. To be able to optimize the operation of the system, it would be valuable to know the minimum static pressure requirement for each

of the zones. With this information, the operator could reduce the primary fan speed to supply the proper air flow at the minimum pressure required by the system.

The procedure for estimating the minimum required static pressure consisted of using the previously described process to determine the required amount of primary air flow to meet the space loads. Once the primary air flow rate was known, the minimum static pressure could be calculated.

Equation 4-11 developed by Furr et al. (2007) can be used to calculate the flow rate for the primary air for both the SCR and ECM FPTUs for a given damper setting and differential pressure. The coefficients for SCR series FPTUs were from Furr et al. (2007) and are presented in Table 4-5. The coefficients for ECM series FPTUs were from Cramlet (2008) and Edmondson (2009) and are presented in Table 4-6.

$$\dot{Q}_p = C_1(1 + C_2S + C_3S^2)\sqrt{\Delta P + 0.27} \quad (4\text{-}11)$$

Table 4-5: Primary air flow coefficients for SCR Series FPTUs. (Furr et.al 2007)

FPTU	C1	C2	C3	R2
SCR_S8A	1644	-1.94E-02	8.46E-05	0.970
SCR_S12A	4350	-2.24E-02	1.29E-04	0.963
SCR_S8B	2127	-2.53E-02	1.78E-04	0.987
SCR_S12B	5903	-3.11E-02	2.67E-04	0.934
SCR_S8C	2137	-3.17E-02	2.82E-04	0.920
SCR_S12C	4022	-1.85E-02	-9.5E-.05	0.964

Table 4-6: Primary air flow coefficients for ECM Series FPTUs. (Cramlet 2008 and Edmondson 2009)

FPTU	C1	C2	C3	R2
ECM_S8A	1637	-1.95E-02	7.80E-05	0.955
ECM_S12A	5109	-2.15E-02	1.14E-04	0.946
ECM_S8B	2094	-2.83E-02	2.06E-04	0.962
ECM_S12B	5886	-3.17E-02	2.54E-04	0.895
ECM_S8C-M1	2344	-3.84E-02	4.15E-04	0.977
ECM_S8C-M2	1895	-3.58E-02	3.70E-04	0.951
ECM_S12C-M1	5125	-3.09E-02	1.28E-04	0.927
ECM_S12C-M2	4561	-1.86E-02	-1.71E-04	0.909

The pressure differential was calculated by using a binary search algorithm for the ΔP needed to calculate the primary flow, $\dot{Q}_p$, required to meet space conditions. The minimum static pressure required that the damper be in a fully open position, so the value of "S" was zero (0) degrees for this calculation. Once ΔP was determined, the upstream static pressure was determined by adding ΔP to the downstream static pressure. For this research, the downstream static pressure was a constant 0.25 in. w.g., which meant that it was possible that the minimum upstream static pressure could be less than 0 in. w.g.

The performance of the system was a function of the operating characteristics of the zones. Figure 4-3 shows the primary air flow rate and the upstream static pressure as a function of the space load from maximum heating to maximum cooling for a series FPTU. The primary air flow rate is the amount of primary air that is required to provide the proper supply temperature to maintain space conditions.

Figure 4-3 shows that the upstream static pressure for the series terminal unit dropped with the space loads and that it stayed at the minimum value when the primary flow rate was at a minimum. The primary fan can be operated at minimal speeds to reduce system static pressure as the loads decreased to minimum values.

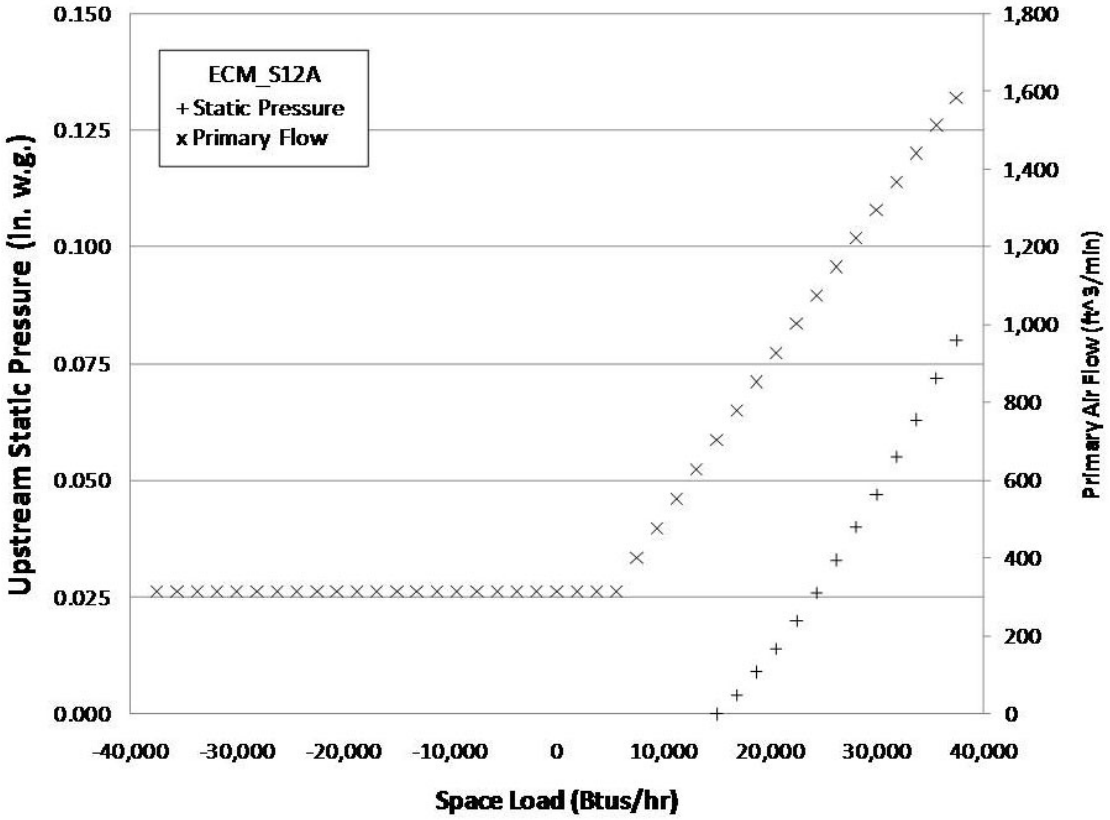

Figure 4-3: Graph of the Series Primary Air Flow Rate and Upstream Static Pressure as a Function of Space Load.

Harmonics

Modeling the harmonics of the series FPTU followed the same procedure as modeling harmonics from the parallel FPTU. Although not previously reported,

Edmondson measured the power factor for series ECM FPTU and the average values are presented Table 4-7 along with the average current THD (%) (Edmondson 2009).

Table 4-7: Power factor and current THD for series ECM FPTUs. (Edmondson 2009)

	THD_i [%]	PF
S8A	90.1	0.40
S8B	89.7	0.42
S8C-M2	85.7	0.49
S12A	85.8	0.51
S12B	89.7	0.45
S12C-M1	162.2	0.50
S12C-M2	153.5	0.54

The voltage THD at the PCC was calculated at the system level and required the harmonic currents from the zones. Measurements taken by Edmondson (2009) provided harmonic currents as a percentage of the fundamental current, I_1. The data from Edmondson (2009) were used to calculate average harmonic ratios for series FPTUs and is presented in Table 4-8. The procedure for calculating the THD at the PCC was included in Chapter V.

Table 4-8: Harmonic current multiplication factors, I_n/I_1, in percent (%) for series ECM FPTU derived from measurements by Edmondson. (Edmondson 2009)

	S8A	S8B	S8C-M2	S12A	S12B	S12C-M1	S12C-M2
2	6.6	5.0	3.3	3.5	5.0	2.0	2.7
3	89.7	93.1	81.3	90.1	91.5	92.6	87.3
4	7.6	5.3	2.7	3.8	4.9	1.8	2.0
5	84.7	87.2	73.2	79.6	82.4	82.9	77.0
6	8.9	6.3	3.0	4.3	5.7	2.0	1.9
7	79.6	80.2	62.6	65.6	71.0	70.7	62.9
8	10.5	7.7	3.6	5.0	7.5	2.2	1.7
9	72.0	70.8	50.5	49.8	57.9	56.7	46.1
10	12.2	9.3	4.4	6.0	9.7	2.2	1.6
11	63.7	60.6	37.6	34.7	45.2	44.0	32.0
12	13.9	11.1	5.7	7.4	11.9	2.1	1.4
13	55.7	50.5	26.9	22.3	34.7	32.2	19.9
14	15.4	12.7	7.1	8.8	13.8	1.8	1.3
15	48.2	40.9	19.4	16.5	27.3	22.7	13.0
16	17.0	14.2	8.8	10.4	15.1	1.5	1.1
17	40.2	31.8	14.5	17.5	23.0	16.0	10.5
18	17.6	14.9	9.6	11.4	15.3	1.3	0.9
19	33.8	24.4	14.3	19.5	21.3	12.1	9.6
20	18.2	15.4	10.3	12.1	15.1	1.0	1.0
21	28.5	18.9	14.8	19.5	19.7	10.2	7.9
22	17.3	14.7	9.0	11.8	13.5	0.9	1.0
23	24.2	15.1	14.3	17.5	17.5	9.1	5.9
24	18.1	14.9	10.4	11.8	12.3	0.8	0.6
25	21.7	13.3	13.6	14.4	15.0	7.6	4.5

The value of the currents for the first twenty-five harmonics were calculated at the zone level by using the multipliers in Table 4-8 with equation 4-12. The current at each frequency was stored and returned as information for use by the system level calculations.

$$I_n = \frac{{}^{I_n}/_{I_1}}{100} I_1 \tag{4-12}$$

I_{rms} was calculated with equation 4-13 using the power consumed by the FPTU and the average power factor from Table 4-7.

$$I_{rms} = \frac{P}{V_{rms}PF} \tag{4-13}$$

For this analysis, V_{rms} was the same as the fundamental harmonic voltage, V_1, and was a user input. For the simulations, 277 V was used because it is a common line voltage used in commercial buildings in the United States and it was the nominal line voltage used during the laboratory testing.

I_1 was calculated with equation 4-14 using I_{rms} and the current THD from Table 4-V-

$$I_1 = \frac{I_{rms}}{\sqrt{1+THD_I{}^2}} \tag{4-14}$$

The value for the triplen currents from a series ECM FPTU were calculated using equation 4-15 using the multipliers presented in Table 4-8 which were derived from measurements made by Edmondson (2009).

$$I_{Ti} = M_i I_1 \tag{4-15}$$

In equation 4-15, I_{Ti} was the triplen current at a specific harmonic and M_i was the multiplier from Table 4-9. The total triplen current was the summation of the four harmonics from Table 4-9 and was $I_{TT} = 1.93I_1$.

Table 4-9: Multipliers for estimating the triplen current for series ECM FPTU.

Triplen	%
3	89
9	58
15	27
21	17

CHAPTER V

SYSTEM MODEL

This chapter describes the model and operation of the Single-Duct Variable Air Volume (SDVAV) air distribution system that supplies air to multiple zones controlled by either SCR or ECM fan-powered terminal units.

Background

One of the objectives of the research was to verify the accuracy of the model using laboratory experiments. The details of the model verification procedure and the experimental results can be found in a paper by Davis et al (2009). The model described in this chapter was based on the verified calculation procedure and was implemented as a Windows program written in C++.

Calculations for the SDVAV system

Figure 5-1 shows a block diagram of the multi-zone single SDVAV system using FPTUs. The components of the SDVAV system consisted of FPTUs that control the zones, return air ducts, exhaust and fresh air ducts, a pre-heat coil (PHC), the primary air fan (Fan), the primary air cooling coil (CC), and the primary air distribution ducts. Figure 5-2 shows a diagram that identifies the calculation sequence used in the simulation program.

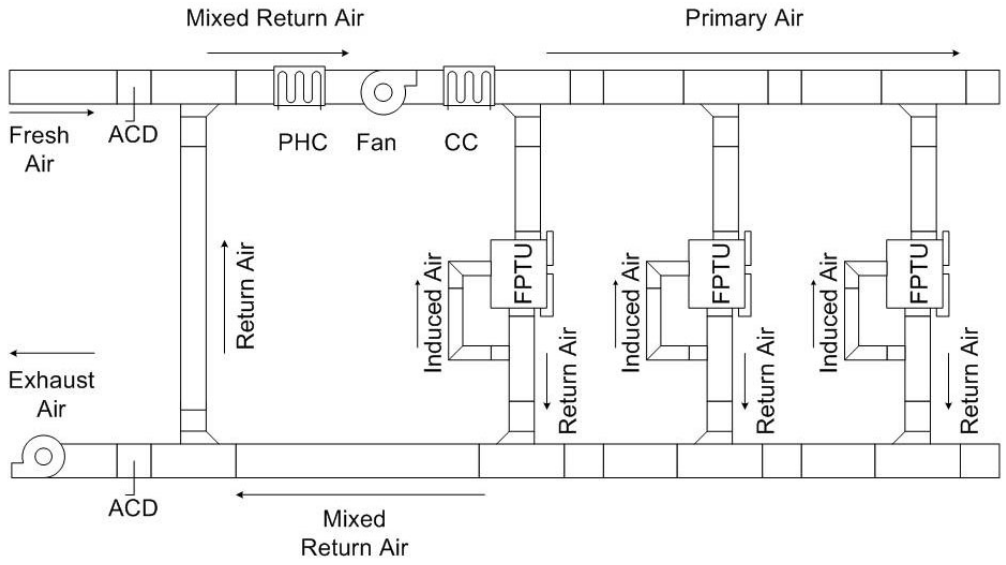

Figure 5-1: Block diagram of a SDVAV system using FPTU.

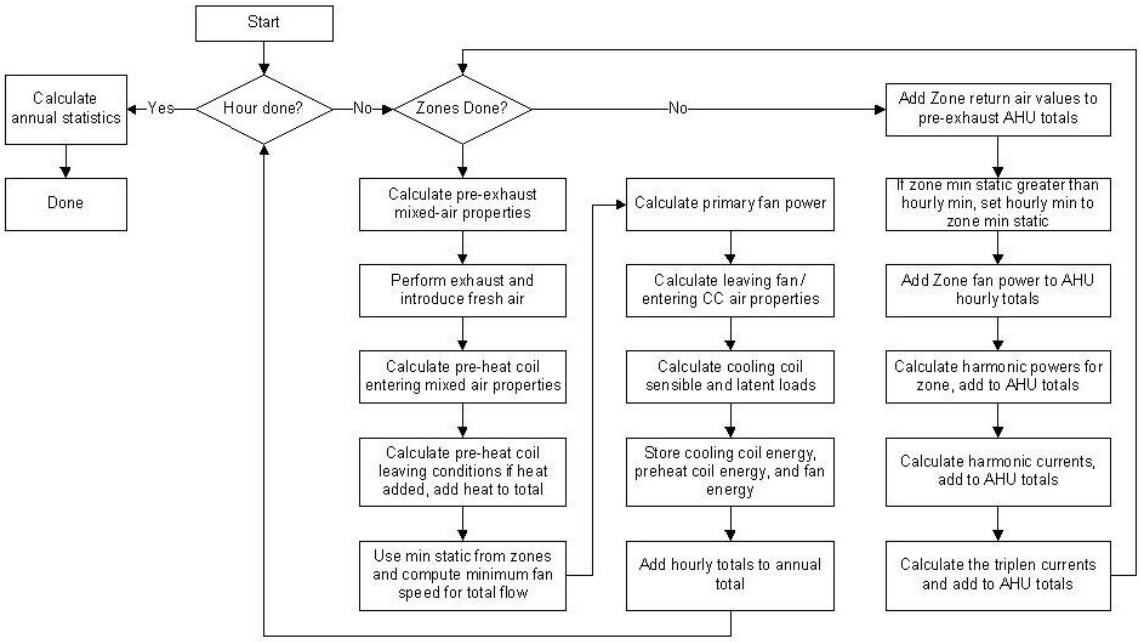

Figure 5-2: SDVAV system simulation flow chart.

The system simulation procedure began with the calculation of the zone level conditions which included the primary air flow rate, the return air flow rate, and the return air temperature and humidity ratio. At each step along the flow path, the temperature and moisture content of the air was calculated. In the cases where air streams were mixed, the mixed air properties of temperature and humidity ratio were calculated.

Once the zone calculations were completed, the mixed return air properties of temperature and humidity ratio were calculated. The mixed return air temperature and humidity ratio were calculated after the introduction of fresh air. The temperature and humidity ratio were estimated for the mixed air after leaving the pre-heat coil which were the conditions of the air entering the primary fan. The temperature and humidity ratio for the primary fan were calculated which were the entering conditions for the primary cooling coil. The temperature and humidity ratio of the air leaving the primary cooling coil were assumed to be the same as the primary air entering the FPTUs.

Zone calculations

The system control algorithm started at the first hour of the year and on an hour-by-hour basis it executed the zone simulation procedure. The zone level calculations were done using methods described in the Chapter III for series FPTU and Chapter IV for parallel FPTU. The hourly procedures provided information such as the required primary flow, return air flow, minimum static pressure, heat added, FPTU fan power, and information about the harmonics that resulted from the operation of the zone. After

all of the zone calculations were completed, the system return air properties were calculated.

Return air

The properties for the system return air were evaluated by performing an energy and mass balance on the return air duct. Equation 5-1 was used to calculate the return air mixed air temperature and was based on an energy balance of the return air stream.

$$T_{ra} = \frac{\sum_i^n \mathrm{Q}_i \times T_i}{\sum_i \dot{V}_i} \tag{5-1}$$

The return air moisture content was calculated using a mass balance. Equation 5-2 was used to calculate the mixed return air humidity ratio based on a mass balance of the return air duct.

$$\omega_{ra} = \frac{\sum_i^n \omega_i \dot{Q}_i}{\sum_i \dot{V}_i} \tag{5-2}$$

Exhaust/fresh air

The properties of the return air after the exhaust and introduction of fresh air was based on energy and mass balances similar to the calculations for the air streams entering the return system from the zones.

The temperature after the exhaust/fresh air intake was calculated using equation 5-3.

$$T_{rapf} = XT_{oa} + (1 - X)T_{ra} \quad (5\text{-}3)$$

In equation 5-3, X is the fraction of fresh air introduced into the return air stream and it is the same as the fraction of the return air that was exhausted from the system. The humidity ratio of the mixed air stream after the exhaust and fresh air intake was calculated using equation 5-4.

$$\omega_{rapf} = X\omega_{oa} + (1 - X)\omega_{ra} \quad (5\text{-}4)$$

Primary fan

Using data from a fan manufacturer, a model was developed that provided a correlation for the flow provided by the fan, $\dot{Q}$, as a function of the fan speed (RPM) and static pressure (Eq. 5-5). A separate correlation provided the fan power as a function of the speed of the fan (Eq. 5-6).

$$\dot{V}_p = a_1 + a_2P + a_3P^2 + a_4S + a_5S^2 + a_6PS + a_7P^2S^2 \quad (5\text{-}5)$$

$$\dot{Q}_f = 746\left(\frac{S}{1631}\right)^3\left(\frac{1}{\eta_{fan}}\right) \quad (5\text{-}6)$$

where $a_1 \ldots a_7$ were constants that were inputs by the user of the model and η_{fan} was the user defined efficiency of the fan in percent. The fan speed was first determined from

the required combination of the air flow and the primary static pressure using a binary search algorithm combined with equation 5-5. Equation 5-6 was used to calculate the power consumed by the fan using the results from equation 5-5.

The binary search algorithm held the static pressure, P, constant and searched for the fan speed, S, that would produce the required amount of flow, $\dot{V}_p$. When the zone calculations were completed, one of the results returned by the zone model was the minimum static pressure required to operate the zone. The static pressure used in equation 5-5 was the maximum value, of the minimum required static pressure for all of the zones.

Pre-heat coil

The return air entered the pre-heat coil after the fresh air was introduced into the system. If the temperature of the pre-fan return air, T_{rapf}, was below the pre-fan minimum temperature, T_{pfm}, then heat energy was added so that the pre-fan return air temperature was at the minimum. Equation 5-7 was used to calculate the amount heat required to warm the return air to the minimum pre-fan temperature.

$$Q_{ph} = C_s \dot{V}_{ra}(T_{pfm} - T_{rapf}) \tag{5-7}$$

The minimum entering fan temperature was calculated by subtracting the fan temperature rise from the cooling coil leaving air temperature. If the temperature of the return air was above the minimum entering air temperature for the fan, then no heat was

added and the temperature of the air entering the fan was the pre-fan return air temperature, T_{rapf}.

The increase in the temperature of the air, ΔT_f, as it passed through the fan was calculated with equation 5-8 using the power consumed by the fan, $\dot{Q}_f$, which was calculated using equation 5-V-

$$\Delta T_f = \frac{3.412\dot{Q}_f}{C_s\dot{V}_{ra}} \tag{5-8}$$

The humidity ratio of the air entering the fan was the same as the humidity ratio of the mixed air after the fresh air was added to the air stream.

Primary cooling coil

The return air cooling coil entering temperature, T_{raec}, was calculated by adding the temperature rise across the fan to the pre-fan return air temperature, T_{rapf}. The sensible cooling load, Q_{ccsen}, handled by the cooling coil was calculated using equation 5-9.

$$Q_{ccsen} = C_s\dot{V}_p(T_{raec} - T_p) \tag{5-9}$$

The latent load, Q_{cclatt}, on the primary cooling coil was calculated using equation 5-10.

$$Q_{cclatt} = C_l\dot{V}_p(\omega_{raec} - \omega_p) \tag{5-10}$$

The total load on the cooling coil was the sum of the sensible and latent loads.

Cooling system model

The operation of the cooling plant was not modeled as a specific type of equipment such as a direct-expansion (DX) packaged rooftop or centrifugal chiller. In order to support an EnergyPlus type of analysis package, the hourly loads were returned to the user as data that could be input for a plant model. For this project the primary cooling coil loads were summed over the course of the year for each location for the purpose of comparing the impact on the operation of the cooling and heating plant that was from the combination of weather and the type of FPTU used in the model.

System level harmonic calculations

The system level calculations were used to estimate the impact of the harmonics from the FPTUs on the power supplied at the PCC. The system model estimated the total power that passed through the PCC. The total power included estimates for non-FPTU fan loads such as the primary fan, lights, and internal loads. The annual energy consumption of the loads on the PCC was calculated because the objective was to estimate the impact of the harmonics from the FPTUs, not to estimate the energy consumption of the loads.

The THD for power was defined by equation 5-11.

$$THD_p = \frac{P_2+P_3+P_4 \ldots P_\infty}{P_1} = \frac{P_{total}-P_1}{P_1} \quad (5\text{-}11)$$

P_{total} at the PCC included all of the power, including harmonics, that passed through the PCC. Non-FPTU loads were input by the user and were treated as constant power loads only at the fundamental frequency. P_1 through P_{25} were generated for each FPTU and were added to the system PCC total for each frequency on an hourly basis. The THD_p was calculated using equation 5-11 from the system totals.

The voltage THD at the PCC was a function of the capacity of the system to supply power and the magnitude of the current THD (Mohan et. al.). Calculation of the voltage THD (THD_V) was not straight-forward and some background is required before the calculation method can be presented. Mohan defined the harmonic voltage with equation 5-12 where V_n, and I_n, were the voltage and current for the n^{th} order harmonic.

$$V_n = (h\omega L_s)I_n \tag{5-12}$$

L_s was the internal inductance of the system at the PCC and is often specified in terms of the short-circuit current, I_{sc}, using equation 5-13 where V_s was the rms value of the per-phase internal voltage of the ac source.

$$I_{sc} = \frac{V_s}{\omega L_s} \tag{5-13}$$

For this analysis, V_s was the same as the fundamental harmonic voltage, V_1. The definition of the THD_v was given by equation 5-14.

$$THD_V = \frac{\sqrt{\sum_{n=2}^{\infty} {V_n}^2}}{V_1} \quad (5\text{-}14)$$

Solving 5-13 for ωL_s and substituting the results into 5-12 resulted in equation 5-15.

$$V_n = nV_s \frac{I_n}{I_{sc}} \quad (5\text{-}15)$$

Equation 5-15 was substituted into equation 5-14 to obtain equation 5-16 which was an expression for THD_V in terms of the harmonic currents and the RMS phase voltage.

$$THD_V = \frac{\sqrt{\sum_{n=2}^{\infty} (nV_s \frac{I_n}{I_{sc}})^2}}{V_s} = \frac{\sqrt{\sum_{n=2}^{\infty} (nI_n)^2}}{I_{sc}} \quad (5\text{-}16)$$

Equation 5-17 defined I_n where I_{nk} was the contribution of terminal unit k to the total harmonic current I_n.

$$I_n = I_{n1} + I_{n2} + I_{n3} + \ \ldots \ I_{nk} = \sum_{k=1}^{\infty} I_{nk} \quad (5\text{-}17)$$

The values of I_n were calculated for the PCC by summing the harmonic current at each frequency from the FPTU in each zone. An alternative method is presented in Appendix II.

The current THD was defined by equation 5-18.

$$THD_I = \frac{\sqrt{\sum_{n=2}^{\infty} {I_n}^2}}{I_1} \quad (5\text{-}18)$$

The fundamental current, I_1, in equation 5-18 was the total current supplied by the PCC as defined by equation 5-19. I_{PCC} was entered by user to calculate the total power.

$$I_1 = I_{PCC} + \sum_{z=1}^{\infty} I_{1z} \quad (5\text{-}19)$$

The total triplen current for the system was a result of the summation of the triplen currents from each FPTU.

CHAPTER VI

MODEL RESULTS

This chapter reported the results of selected cases that were simulated using the SDVAV system. The model predicted the operation of a SDVAV air distribution system that supplied air to multiple zones controlled by either SCR or ECM fan-powered terminal units.

Background

The system model was used to predict the operation of a commercial building for one year for both series and parallel fan powered terminal units at five different geographical locations around the United States. The first part of the chapter covers the results from the base case operating conditions and used Houston weather data for the analysis. Following the base case operation, a sensitivity analysis was done that investigated changes in the FPTU manufacturer, primary air leakage rate, and location. The case variations include the following:

1. Base case with Houston weather.
2. Base case with Houston weather and a change in manufacturer for ECM FPTU.
3. Base case settings at five locations around the United States.
4. Base case parallel FPTU with Houston weather and primary air leakage rates of 5%, 10% and 20%.
5. Impact of continuous leakage rate of 20% at five locations around the United States.

Base case

The base case settings were intended to mimic the theoretical best case operating patterns of buildings that used fan powered terminal units. The leakage rate was set to zero to mimic perfect back-draft damper operation and flawless manufacturing. The operating schedule was for 24 hours a day for the entire year.

Table 6-1 shows the annual totals for total plant energy, cooling plant energy, primary fan energy, terminal unit fan energy, heat added to maintain space temperature, the maximum upstream static pressure required to supply air to the zones, and the minimum upstream static pressure required to supply air to the zones. The simulation used ECM_S12A, SCR_S12A, ECM_P12A, and SCR_P12A terminal units.

Table 6-1: Simulation results summary for the base case Houston location.

	SCR_S12A	ECM_S12A	SCR_P12A	ECM_P12A
Total Plant Energy (MMBtus)	592	551	533	532
Total Cooling Plant (MMBtus)	207	197	193	193
Primary Fan Energy (MMBtus)	12.8	10.8	11.1	11.5
Terminal Unit Fan Energy (MMBtus)	111	39	32	11
Heat Added (MMBtus)	262	304	297	317
Fan + Heat (MMBtus)	373	343	329	328
Max Static (in)	0.117	0.072	0.261	0.368
Min Static (in)	0.000	0.000	0.026	0.036

The total plant energy was the summation of the cooling plant, primary fan energy, terminal unit fan energy and heat added. The total cooling energy was the cooling BTUs supplied by the primary cooling coil over the entire year. Because the model developed during project was intended to be used within a simulation program such as EnergyPlus,

neither detailed cooling nor heating plant simulations were done and the energy quantities used by the mechanical systems were not estimated by the simulation.

Instead of a plant simulation an average plant energy use estimate was done after the SDVAV model completed the annual simulation. The cooling plant energy was estimated using an annual average EER of 11.0 to calculate an average COP of 3.2 that was divided into the total cooling energy to estimate the energy used by the cooling plant. The EER of 11.0 was taken from the minimum efficiency standards for package rooftop air-conditioning units (Energy Star 2010). The heat added was treated as electric resistance heating and was the heating plant energy.

The ECM_P12A FPTU used 0.2% less total plant energy than the SCR_P12A unit. This made sense because the parallel terminal unit fans operated only during heating mode and any heat energy not added to the space from the more efficient ECM motor was replaced by space heating as shown by the total of the FPTU fan energy plus the space heat added for the two units which was 328 MMBTUs for the ECM_P12A and 329 MMBTUs for the SCR_P12A.

The total plant energy used by the ECM_S12A was V-9% less than the total plant energy used by the SCR_S12A terminal unit. The drop in total plant energy consumption was due to the decreased terminal unit fan energy (64.8%) which resulted in a drop in cooling energy of 4.8% and was net decrease after including the increased heat added (1V-0%) during the winter operation.

The primary fan energy used by the ECM_P12A was 3.6% higher than the SCR_P12A. The higher energy can be attributed to the increase in the static pressure

required by the ECM terminal unit compared to the pressure required for the SCR unit. This was a difference solely due to the performance of the units.

Table 6-1 shows that the primary fan used more energy for the SCR_S12A system than for either of the parallel systems. A commonly held expectation was that a primary fan would use less energy for a series system than for a parallel system because the series primary fan does not have to work against as much static pressure as the parallel primary fan. The results clearly show that this was not the case for series SCR FPTU. The reason the primary fan energy was higher for the series SCR system than the parallel systems was because the series SCR FPTU required more primary air flow during cooling conditions.

For example, the SCR_S12A terminal unit fans used 743 W. The total power consumption by the terminal unit fans in the series system was 3,715 W or a cooling load of 12,700 Btu/hr and is approximately equal to one ton (thermal) of air-conditioning. Because of the extra heat load in the zones from the terminal unit fans, the primary fan was forced to supply an extra 500 CFM (240 l/s) against the highest peak static pressure requirement for all five of the zones.

$$CFM = \frac{12{,}700\ Btus/hr}{C_{ps}\left(T_{setpoint} - T_{primary}\right)} = \frac{12{,}700\ Btus/hr}{1.1\frac{Btus/hr}{F - cfm}(78 - 55)F} = 500\ cfm$$

Figure 6-1 shows the primary air flow rate as the normalized space load varies from heating to the maximum cooling load. Figure 6-1 shows that the primary air flow for the

SCR_S12A system was higher than the primary air flow rates for all other systems while handling the same space loads.

Figure 6-2 shows the upstream static pressure for all four ideal case terminal units as a function of space load. From Figure 6-2, the upstream static pressure for the parallel terminal units increased from 0.025 in.wg. (V-2 Pa) just before the terminal unit fan turned on to 0.22 in.wg. (54.8 Pa) just after the terminal fan unit turned on. The peak primary air flow rate through the terminal units in Figure 6-2 was 1,575 CFM (units) which was the rated capacity of the unit.

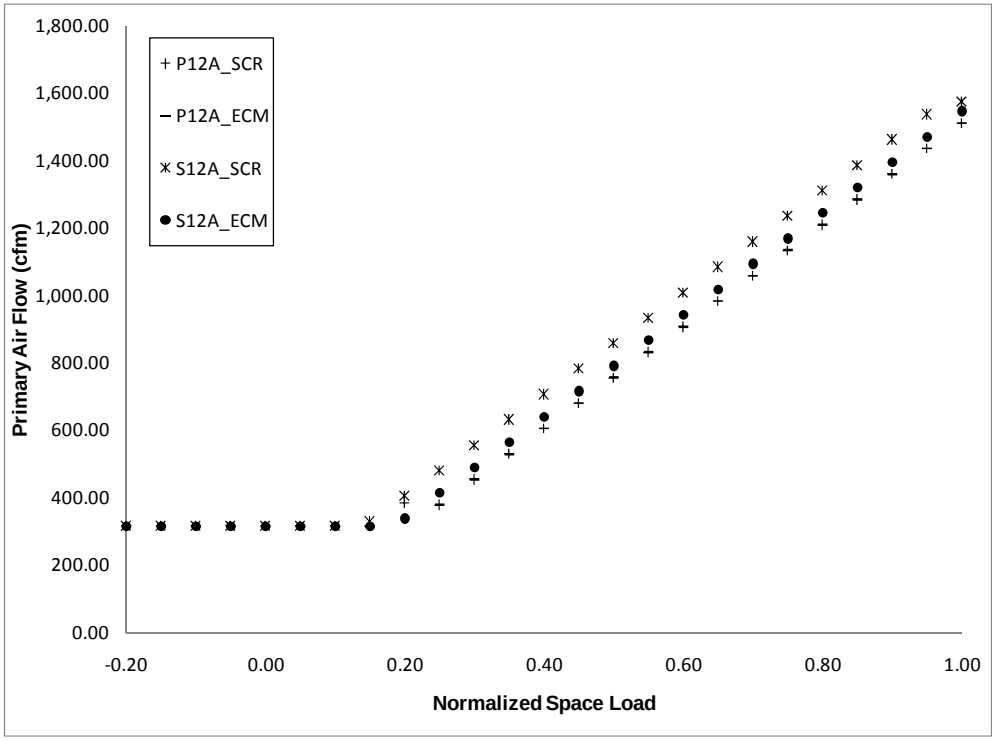

Figure 6-1: Primary air flow rate as function of the space load for the base FPTU.

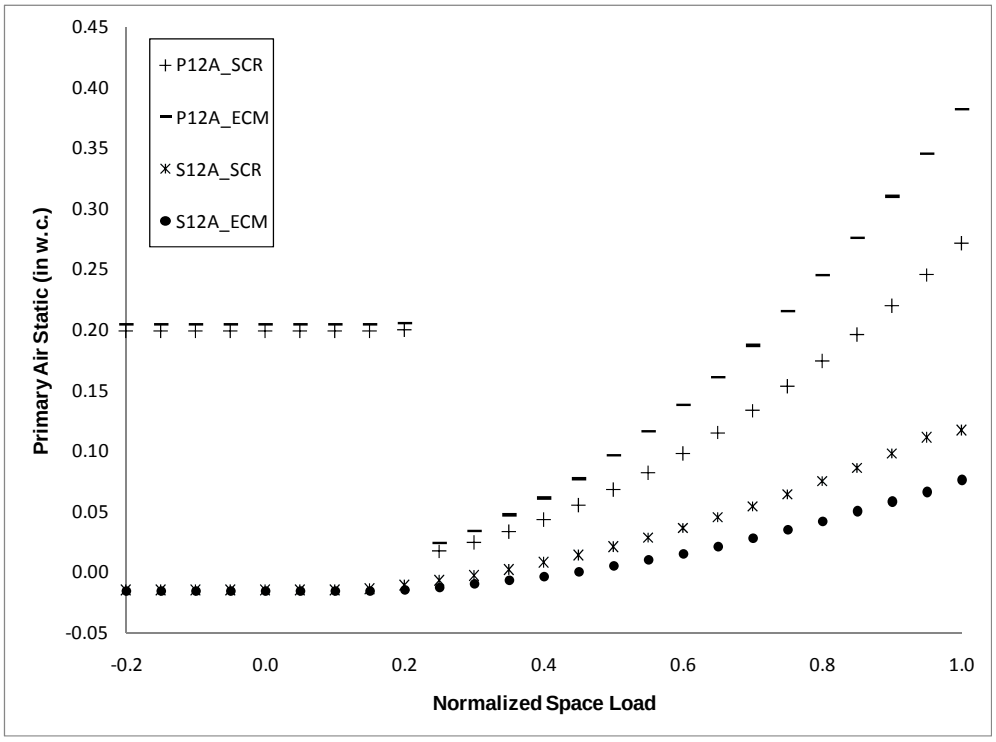

Figure 6-2: Primary static pressure as a function of space load for the base FPTU.

As a result of the parallel terminal unit fan starting, the upstream static pressure increased to 0.22 in.wg. (54.8 Pa) which resulted in a total system pressure increase to 0.22 in.wg. (54.8 Pa). At minimum flow conditions of 0.02 in.wg. static pressure (5.0 Pa) before the fan turned on and 315 CFM (149 l/s) of primary air, the primary fan required 0.26 hp (194 W). When the fan turned on, the static pressure was 0.21 in.wg. (52.3 Pa) and the primary fan required 0.30 hp (224 W) to deliver the flow of 315 CFM (149 l/s).

Case 1 - sensitivity to unit manufacturer

Table 6-2 shows the simulation summary results for the ideal case simulation using parallel ECM FPTUs P12A, P12B and P12C. The replacement of the ECM_P12A terminal unit with either of the other two manufacturer's units had no significant impact on the total cooling plant energy. ECM_P12B used 2.6% less primary fan energy and 27.3% more terminal unit fan energy than the ECM_P12A. ECM_P12C used 1.7% more primary fan energy than ECM_P12A. Although both P12B and P12C used more primary fan energy than ECM_P12A, the difference was not enough to affect the total cooling energy. Both ECM_P12B and ECM_P12C used more terminal unit fan energy than ECM_P12A; the additional energy was used during heating mode and was offset by the reduced amount of added heat required by the zone so there was no net increase in the energy consumed by the system as shown by the value of the "fan + heat" which was 324 MMBTUs for all three units.

The sensitivity of the simulation to unit manufacturer for the SCR parallel units was previously documented in the final report for ASHRAE RP 1292 (Davis, et. al., 2007) and showed no difference in the results based on the selection of the manufacturer.

Table 6-2: Simulation Results for the ECM P12A, P12B, and P12C FPTUs.

	Parallel ECM		
	P12A	**P12B**	**P12C**
Total Energy (MMBtus)	532	532	532
Total Cooling (MMBtus)	193	192	193
Primary Fan Energy (MMBtus)	11.5	11.2	11.7
Terminal Unit Fan Energy (MMBtus)	11.0	14.0	11.0
Heat Added (MMBtus)	317	314	317
Fan + Heat (MMBtus)	328	328	328
Max Static (in)	0.368	0.273	0.414
Min Static (in)	0.036	0.027	0.041

Table 6-3 shows the simulation summary results for the base case simulation using series ECM FPTUs S12A, S12B and S12C. The total plant energy consumed by the ECM_S12A system when replaced by the ECM_S12B and ECM_S12C increased by 2.2% and 0.9%, respectively. The terminal unit fan for the S12B and S12C was 56% and 28% higher, respectively, than the S12A.

Overall, the slight change in energy consumed by the system was due to the decreased amount of heat energy added during low load conditions. The combination of the heat added and the terminal unit fan energy for the S12B and S12C were 2.6% and 1.2% more than for the ECM_S12A.

With less than a 2.2% difference in total plant energy, cooling energy, total plant energy, and cooling plant energy, the impact of the selection of the unit from a particular manufacturer had no significant impact on the performance of the system.

The sensitivity of the simulation to unit manufacturer for the SCR series units was previously documented in the final report for ASHRAE RP 1292 (Davis, et. al., 2007) and also showed no significant difference in the results based on the selection of the

manufacturer because a generic equation that was developed from the measured data was used to perform the simulations.

Table 6-3: Simulation results for the ECM S12A, S12B, and S12C FPTUs.

	Series ECM		
	S12A	**S12B**	**S12C**
Total Energy (MMBtus)	551	563	556
Total Cooling (MMBtus)	197	200	198
Primary Fan Energy (MMBtus)	10.8	11.2	11.1
Terminal Unit Fan Energy (MMBtus)	39.0	61.0	50.0
Heat Added (MMBtus)	304	291	297
Fan + Heat (MMBtus)	343	352	347
Max Static (in)	0.072	0.053	0.075
Min Static (in)	0.000	0.000	0.000

Case 2 – base case operation at five locations in the United States

The detailed results from the simulations for the five locations were included in Appendix III. The results from the five locations were extracted from tables in the appendix and were consolidated into Tables 6-4 through 6-8.

Table 6-4 shows a summary of the change in total plant energy consumption for all five locations when one type of FPTU was replaced with another type of FPTU. The first column shows the location and the next six columns show the percent change of total plant energy consumed when the operation of the first FPTU listed in the column heading was compared to the operation the second FPTU listed in the column heading. For example, the first column with data shows that when the ECM_S12A was compared to the SCR_S12A, the total plant energy decreased by 7.0%. From the results included

in the appendix, the total plant energy consumed by ECM_S12A and SCR_S12A was 551 MMBTUs and 592 MMBTUs respectively which was a V-9% decrease in energy consumption ((551 – 592)/592*100% = -V-9%).

Table 6-4: Change in total plant energy usage by location and unit type for 24 hour operation.

	Change (%)					
	Compare ECM_S12A to SCR_S12A	Compare SCR_P12A to SCR_S12A	Compare ECM_P12A to SCR_S12A	Compare SCR_P12A to ECM_S12A	Compare ECM_P12A to ECM_S12A	Compare ECM_P12A to SCR_P12A
Houston	-7.0	-10.1	-10.2	-3.2	-3.4	-0.1
Phoenix	-8.5	-12.3	-12.5	-4.1	-4.3	-0.2
Chicago	-5.9	-8.0	-8.2	-2.3	-2.5	-0.1
New York	-6.7	-9.2	-9.3	-2.7	-2.9	-0.2
San Francisco	-6.7	-9.3	-9.3	-2.7	-2.8	-0.1
Average	-7.0	-9.8	-9.9	-3.0	-3.2	-0.1

The change in energy consumption from the SCR_S12A unit to the ECM_S12A unit resulted in an average drop of in total plant energy consumption of 7.0% for all locations. The drop in consumption was higher for locations that had a higher cooling load such as Houston (-7.0%) and Phoenix (-8.5%) when compared to cooler climates such as Chicago (-5.9%).

When the SCR_S12A unit was replaced with either the SCR_P12A or the ECM_P12A, the energy was essentially the same for both replacements and averaged -9.9% which was a decrease of 9.9% in consumption. The decrease was greater for hotter climates such as Phoenix than for cooler climates such as San Francisco. When the ECM_S12A was compared to both the ECM_P12A and the SCR_P12A the average drop

in consumption was 3.1%. The last column shows that there was no significant difference in the operation of the ECM_P12A and the SCR_P12A.

Table 6-5 shows a summary of the change in cooling plant energy consumption for all five locations when one type of FPTU was replaced with another type of FPTU. The change in cooling plant energy consumption from the SCR_S12A unit to the ECM_S12A unit resulted in an average drop of in total plant energy consumption of 4.5% for all locations. The drop in consumption was higher for locations that had a higher cooling load such as Houston (-4.8%) and Phoenix (-5.2%) when compared to cooler climates such as San Francisco (-4.1%).

Table 6-5: Change in cooling plant energy usage by location and unit type for 24 hour operation.

	Change (%)					
	Compare ECM_S12A to SCR_S12A	Compare SCR_P12A to SCR_S12A	Compare ECM_P12A to SCR_S12A	Compare SCR_P12A to ECM_S12A	Compare ECM_P12A to ECM_S12A	Compare ECM_P12A to SCR_P12A
Houston	-4.8	-6.8	-6.8	-2.1	-2.2	-0.1
Phoenix	-5.2	-7.5	-7.5	-2.4	-2.5	-0.1
Chicago	-4.2	-5.9	-6.0	-1.8	-1.8	0.0
New York	-4.4	-6.2	-6.2	-1.9	-1.9	0.0
San Francisco	-4.1	-5.8	-5.9	-1.7	-1.8	-0.1
Average	-4.5	-6.4	-6.5	-2.0	-2.0	-0.1

When the SCR_S12A unit was replaced with either the SCR_P12A or the ECM_P12A, the change in the cooling plant consumption was essentially the same for both replacements and averaged -V-5%. The decrease was greater for hotter climates such as Phoenix than for cooler climates such as San Francisco.

When the ECM_S12A was compared to both the ECM_P12A and the ECM_P12A the average drop in cooling plant consumption was 2.0%. This was a significant result because it shows that the ECM_S12A uses nearly the same amount of cooling plant energy as the parallel FPTU, within 2%. The last column shows that there was no significant difference in the operation of the ECM_P12A and the SCR_P12A for the no leakage case.

Table 6-6 shows a summary of the change in primary fan energy consumption for all five locations when one type of FPTU was replaced with another type of FPTU. The change in primary fan energy consumption from the SCR_S12A unit to the ECM_S12A unit resulted in an average drop of 14.9% for all locations. The drop in consumption was only slightly higher for locations that had higher cooling requirements; Phoenix required only 1.2% more primary fan energy than San Francisco.

Table 6-6: Change in primary fan energy usage by location and unit type for 24 hour operation.

	Change (%)					
	Compare ECM_S12A to SCR_S12A	Compare SCR_P12A to SCR_S12A	Compare ECM_P12A to SCR_S12A	Compare SCR_P12A to ECM_S12A	Compare ECM_P12A to ECM_S12A	Compare ECM_P12A to SCR_P12A
Houston	-15.1	-12.6	-9.5	2.9	6.6	3.6
Phoenix	-15.6	-13.1	-10.0	2.9	6.5	3.5
Chicago	-14.3	-9.7	-6.4	5.3	9.3	3.7
New York	-14.7	-10.6	-7.3	4.8	8.6	3.7
San Francisco	-14.8	-4.4	-6.2	12.2	10.2	-1.8
Average	-14.9	-10.1	-7.9	5.6	8.2	2.5

When the SCR_S12A unit was replaced with the SCR_P12A or the ECM_P12A, the change in the primary consumption changed by an average of -10.1% and -7.9% respectively. The difference in the primary fan consumption was a result of the higher static pressure requirements of the ECM_P12A (0.382 in. w.g.) when compared to the SCR_P12A (0.271 in. w.g.).

When the ECM_S12A was compared to both the SCR_P12A and the ECM_P12A the average drop in primary fan energy consumption was 5.6% and 8.2% respectively. One again, this was a direct result of the higher static pressure requirement of the ECM_P12A. The last column shows that there was an average of 2.5% difference in the operation of the primary fan when the ECM_P12A was compared to the SCR_P12A.

Table 6-7 shows a summary of the change in terminal unit fan energy consumption for all five locations when one type of FPTU was replaced with another type of FPTU. The change in primary fan energy consumption from the SCR_S12A unit to the ECM_S12A unit resulted in an average drop of 65.4% for all locations. The drop in consumption was only slightly higher for locations that had higher heating requirements; San Francisco required only 0.9% more terminal unit fan energy than Phoenix.

Table 6-7: Change in terminal unit fan energy usage by location and unit type for 24 hour operation.

	Change (%)					
	Compare ECM_S12A to SCR_S12A	Compare SCR_P12A to SCR_S12A	Compare ECM_P12A to SCR_S12A	Compare SCR_P12A to ECM_S12A	Compare ECM_P12A to ECM_S12A	Compare ECM_P12A to SCR_P12A
Houston	-64.9	-71.2	-90.1	-17.9	-71.8	-65.6
Phoenix	-64.9	-73.0	-91.0	-23.1	-74.4	-66.7
Chicago	-65.8	-67.6	-89.2	-5.3	-68.4	-66.7
New York	-65.8	-68.5	-89.2	-7.9	-68.4	-65.7
San Francisco	-65.8	-82.9	-89.2	-50.0	-68.4	-36.8
Average	-65.4	-72.6	-89.7	-20.8	-70.3	-60.3

When the ECM_S12A was compared to both the ECM_P12A, the average drop in consumption was only 13.5%. This was a direct result of the increased efficiency of the ECM motor. This shows that the ECM_S12A used about the same amount of terminal unit fan energy, within 13.5%, as the SCR_P12A even though the SCR_P12A only ran when the system was in heating mode.

Table 6-8 shows a summary of the change in heat added to maintain space conditions for all five locations when one type of FPTU was replaced with another type of FPTU. The change in heat added from the SCR_S12A unit to the ECM_S12A unit resulted in an average increase of 18.4% for all locations. The increase in heat added was higher for locations that had longer heating seasons; San Francisco required 5.2% more heat added than Houston.

Table 6-8: Change in heat added by location and unit type for 24 hour operation.

	Change (%)					
	Compare ECM_S12A to SCR_S12A	Compare SCR_P12A to SCR_S12A	Compare ECM_P12A to SCR_S12A	Compare SCR_P12A to ECM_S12A	Compare ECM_P12A to ECM_S12A	Compare ECM_P12A to SCR_P12A
Houston	16.0	13.4	21.0	-2.3	4.3	6.7
Phoenix	19.5	16.0	25.5	-2.9	5.0	8.2
Chicago	16.9	14.1	22.2	-2.4	4.5	7.1
New York	18.4	15.2	24.0	-2.7	4.7	7.6
San Francisco	21.2	24.8	27.9	3.0	5.6	2.5
Average	18.4	16.7	24.1	-1.5	4.8	6.4

When the SCR_P12A was compared to the SCR_S12A, the average increase in heat added was only 1V-7% but when the ECM_P12A was compared to the SCR_S12A, the heat added was 24.1%. This was a direct result of the increased efficiency of the ECM motor which added less heat to the space when the zone load was at or below the cooling load handled by the minimum primary flow set-point. The heat input lost from the efficiency increase of the ECM motors was replaced by heat added. In most cases, even though the heat added increased by switching to a more efficient motor, the reduced load during cooling was more than the added heating loads during the winter.

Case 3 – Impact of leakage rates of 5%, 10% and 20%

The previous cases were for systems that used parallel FPTU that did not have leakage of primary air into the return air stream. Series FPTU did not have an issue of primary air leaking into the return air stream so series leakage was not included in this simulation.

The leakage problem consisted of primary air that passed through the air valve into the mixing chamber where most of the air exited through the supply air duct and some of

the air exited either through the seams of the FPTU or through the back-draft damper that covered the terminal unit fan port.

Case 3 consisted of analyzing the impact of leakage rates of 5%, 10% and 20% on the base case operation using Houston weather data. The analysis was done for both SCR and ECM parallel FPTU. 5%, 10% and 20% leakage for this case was included in the parallel terminal unit models because a significant amount of leakage was measured during the laboratory measurements in some ECM and SCR parallel terminal units. Table 6-9 shows the results of the simulation when leakage was added to the base case (Houston) operation for SCR_P12A. Table 6-10 shows the results of the simulation when leakage was added to the base case (Houston) operation for ECM_P12A. Using data from Tables 6-9 and 6-10, the total plant energy increased by 3.0%, 5.8% and 11.7% over the base case when leakage was 5%, 10% and 20%, respectively, for both the ECM_P12A and SCR_P12A units.

Table 6-9: Simulation results for SCR_P12A for 24 hour operation with 5%, 10% and 20% leakage rates.

	SCR_P12A			
	Base	**5%**	**10%**	**20%**
Total Plant Energy (MMBtus)	533	548	563	595
Total Cooling Plant (MMBtus)	193	197	201	210
Primary Fan Energy (MMBtus)	11.1	12.5	13.9	17.2
Terminal Unit Fan Energy (MMBtus)	32.0	32.0	32.0	32.0
Heat Added (MMBtus)	297	307	316	336
Fan + Heat (MMBtus)	329	338	348	368
Max Static (in)	0.261	0.265	0.270	0.279
Min Static (in)	0.026	0.026	0.026	0.027

Table 6-10: Simulation results for ECM_P12A for 24 hour operation with 5%, 10% and 20% leakage rates.

	ECM_P12A			
	Base	**5%**	**10%**	**20%**
Total Plant Energy (MMBtus)	532	548	564	596
Total Cooling Plant (MMBtus)	193	197	201	210
Primary Fan Energy (MMBtus)	11.5	13.0	14.5	18.0
Terminal Unit Fan Energy (MMBtus)	11.0	11.0	11.0	11.0
Heat Added (MMBtus)	317	327	337	357
Fan + Heat (MMBtus)	328	338	348	367
Max Static (in)	0.368	0.384	0.399	0.433
Min Static (in)	0.036	0.038	0.039	0.042

For both the ECM_P12A and SCR_P12A units, the cooling plant energy increased by 2.1%, 4.1% and 8.7% over the base case when leakage was 5%, 10% and 20%, respectively. For both the ECM_P12A and SCR_P12A units, the primary fan energy increased by approximately 13.0%, 25% and 55% for 5%, 10% and 20% leakage rates, respectively. The proportional increase in primary fan energy with the increased leakage rates was a direct result of the primary fan handling the additional flow from the leaked air. The terminal unit fan energy was not affected by the leakage rates. For the SCR_P12A unit, the heat added increased by 3.3%, V-5% and 13.0% for 5%, 10% and 20% leakage rates, respectively. For the ECM_P12A unit, the heat added increased by 3.2%, V-5% and 13.0% for 5%, 10% and 20% leakage rates, respectively.

Case 4 – Impact of a leakage rate of 10% at five locations

The detailed results from the simulations for the five locations was included in Appendix III and the results were extracted from tables in the appendix and consolidated into Tables 6-11 through 6-14. The change in the terminal unit fan energy was not

affected by the leakage and since it was previously considered, it was not included with this case. Table 6-11 shows a summary of the change in total plant energy consumption for all five locations when the SCR_S12A and ECM_S12A FPTU were replaced with the ECM_P12A FPTU.

Table 6-11: Change in total plant energy usage by location and unit type for 24 hour operation.

	Total Plant Energy (MMBtus)			Change (%)	
	SCR_S12A	ECM_S12A	ECM_P12A	Compare ECM_P12A to SCR_S12A	Compare ECM_P12A to ECM_S12A
Leakage Rate	NA	NA	10%	10%	10%
Houston	592.4	550.7	563.6	-4.9	2.4
Phoenix	545.2	498.7	508.5	-6.7	2.0
Chicago	562.9	529.9	546.6	-2.9	3.2
New York	537.3	501.6	517.5	-3.7	3.2
San Francisco	504.5	470.4	487.4	-3.4	3.6
			Average	-4.3	2.8

The change from the SCR_S12A unit to the ECM_P12A unit with 10% leakage resulted in an average decrease in total plant energy consumption of 4.3% for all locations. The decrease in consumption was lower for locations that had higher heating loads such as Chicago (2.9%) and San Francisco (3.4%) when compared to warmer climates such as Phoenix where there was a drop in total plant energy of V-7%. These results were significant because they meant that a 10% leakage rate dropped the performance of a parallel FPTU with an ECM motor to a level that close the worst performing series terminal unit.

The change from the ECM_S12A unit to the ECM_P12A unit with 10% leakage resulted in an average increase in total plant energy consumption of 2.8% for all locations. The increase in consumption was higher for locations that had higher heating loads such as Chicago (3.2%) and San Francisco (3.6%) when compared to warmer climates such as Phoenix where there was an increase in total plant energy of 2.0%. These results were significant because they meant that a 10% leakage rate dropped the performance of a parallel FPTU with an ECM motor to a level that was below the worst ECM series terminal unit.

Table 6-12 shows a summary of the change in cooling plant energy consumption for all five locations when the SCR_S12A and ECM_S12A FPTU were replaced with the ECM_P12A FPTU. The change from the SCR_S12A unit to the ECM_P12A unit with 10% leakage resulted in an average decrease in cooling plant energy consumption of 2.6% for all locations. These results were significant because they meant that a 10% leakage rate dropped the performance of a parallel FPTU with an ECM motor to a level that was close to the worst performing series terminal unit.

Table 6-12: Change in cooling plant energy usage by location and unit type for 24 hour operation.

	Cooling Plant Energy (MMBtus)			Change (%)	
	SCR_S12A	ECM_S12A	ECM_P12A	Compare ECM_P12A to SCR_S12A	Compare ECM_P12A to ECM_S12A
Leakage Rate	NA	NA	10%	10%	10%
Houston	206.7	196.9	201.1	-2.7	2.2
Phoenix	221.7	210.2	214.5	-3.3	2.0
Chicago	158.3	151.6	154.4	-2.4	1.8
New York	166.4	159.1	162.1	-2.6	1.9
San Francisco	162.6	155.9	159.1	-2.2	2.1
			Average	-2.6	2.0

The change from the ECM_S12A unit to the ECM_P12A unit with 10% leakage resulted in an average increase in total plant energy consumption of 2.0% for all locations. These results were significant because they meant that a 10% leakage rate dropped the performance of a parallel FPTU with an ECM motor to a level that was below the ECM series terminal unit.

Table 6-13 shows a summary of the change in primary fan energy consumption for all five locations when the SCR_S12A and ECM_S12A FPTU were replaced with the ECM_P12A FPTU. The change from the SCR_S12A unit to the ECM_P12A unit with 10% leakage resulted in an average increase in primary fan energy consumption of 14.8% for all locations. The change from the ECM_S12A unit to the ECM_P12A unit with 10% leakage resulted in an average increase in primary fan energy consumption of 34.9% for all locations.

Table 6-13: Change in primary fan energy usage by location and unit type for 24 hour operation.

	Primary Fan Energy (MMBtus)			Change (%)	
	SCR_S12A	ECM_S12A	ECM_P12A	Compare ECM_P12A to SCR_S12A	Compare ECM_P12A to ECM_S12A
Leakage Rate	NA	NA	10%	10%	10%
Houston	12.8	10.8	14.5	13.7	34.0
Phoenix	12.4	10.5	14.0	12.7	33.5
Chicago	9.6	8.2	11.2	16.4	35.8
New York	9.9	8.5	11.5	15.2	35.1
San Francisco	8.9	7.5	10.3	15.9	36.1
			Average	14.8	34.9

Table 6-14 shows a summary of the change in heat added for all five locations when the SCR_S12A and ECM_S12A FPTU were replaced with the ECM_P12A FPTU. The change from the SCR_S12A unit to the ECM_P12A unit with 10% leakage resulted in an average increase in heat added of 32.8% for all locations. The increase in heat added resulted from a combination of the loss of the heat from the SCR_S12A motors during the heating season as well as the added over-cooling that resulted from the leakage during the heating season.

Table 6-14: Change in heat added by location and unit type for 24 hour operation.

	Heat Added (MMBtus)			Change (%)	
	SCR_S12A	ECM_S12A	ECM_P12A	Compare ECM_P12A to SCR_S12A	Compare ECM_P12A to ECM_S12A
Leakage Rate	NA	NA	10%	10%	10%
Houston	262.0	304.0	337.0	28.6	10.9
Phoenix	200.0	239.0	270.0	35.0	13.0
Chicago	284.0	332.0	369.0	29.9	11.1
New York	250.0	296.0	332.0	32.8	12.2
San Francisco	222.0	269.0	306.0	37.8	13.8
			Average	32.8	12.2

The change from the ECM_S12A unit to the ECM_P12A unit with 10% leakage resulted in an average increase in total plant energy consumption of 12.2% for all locations. The increased heat added for this case was due to the increased over-cooling during the heating season that was a result of the leakage.

Results summary

The interest in using fan powered terminal units was driven by the opportunity to save money by decreasing the energy use and associated operating costs of the primary fan and the cooling load that it added to the system. The significant results from this project were a better understanding of the impact on the cooling plant and primary fan when FPTUs were used.

The parallel fan powered terminal unit consistently used less cooling energy than the series fan powered terminal units when leakage was not taken into account. However, in real systems leakage must be considered. The results from the laboratory measurements (Furr et al. 2007, Cramlet 2008, and Edmondson 2009) showed that parallel terminal

units have a leakage problem. The extent of the leakage was not clear and needs to be studied in greater detail to determine a realistic average leakage rate. The measurements from laboratory experiments combined with the sensitivity analysis indicated that leakage can have a substantial impact on the system performance as well as the overall energy consumption.

The series ECM FPTU was extremely close in operation to the parallel FPTU without leakage but it still used 2% more energy overall, than the parallel FPTU that used SCR motors. When leakage was considered, the series FPTU out-performed the parallel terminal units except for extremely hot climates. When large amounts of leakage were considered, say 10%, the series ECM FPTU outperformed the parallel FPTU by over 2.8%.

Consideration should also be given to what happens to the SDVAV system during low-load conditions when one of the terminal unit fans turns was turned on. The activation of the terminal unit fan caused an increase in the supply flow rate for the zone which increased the downstream static pressure for that zone. This resulted in the increase in the pressure of the primary fan which increased the overall operating cost of the system.

CHAPTER VII

DEVELOPMENT OF A FPTU CFD MODEL

Computational Fluid Dynamics (CFD) is the application of numerical methods to discretize and solve appropriately simplified versions of the Navier-Stokes (NS) equations. The solution of the Navier-Stokes equations required knowledge of the properties of the fluid, the type of flow, and the geometry of the flow path. This chapter detailed the development of the 3-D models that described the geometry of the flow path and the physics models as they were applied to a FPTU CFD analysis.

Introduction

The process of conducting the CFD analysis consisted of building a virtual model that represented both the geometry of the fluid flow path and the physics of the internal interactions of the fluid, as well as the fluid interaction with the physical boundaries.

For this thesis, the physical model referred to the virtual representation of the geometry of the air flow path and the solid components of the FPTU such as the walls of the unit and the damper. The physics model described the properties of the air and its interactions with the boundaries defined by the physical model.

The first part of this chapter described the development of the control volume model and the last part of the chapter described the development of the physics model. SolidWorks (SW) and Star CCM+ (SC) were the two software packages that were used to develop the control volume and the numerical models. SolidWorks was a 3-D graphics modeling program and it was used to create virtual models of the internal

components of the FPTU which consisted of the flow sensor, damper, and porous baffle (PB). Star CCM+ was a CFD numerical analysis program which has a graphical user interface that was used to create the control volume models used as the basis for a CFD analysis. The geometrical modeling tools in Starr CCM+ were used to create the boundaries of inlet air valve, the mixing chamber and to import the internal components created with SW to define the control volume which was the primary air flow path through the FPTU.

Development of the control volume model

A parallel FPTU was determined to be the best type of unit for the CFD study because the pressure drop through the unit could be easily measured. It was noticed during the study of the SCR FPTU that the SCR_P12C had a larger pressure drop through the unit than other FPTUs of the same size for a given primary air flow rate. Figure 7-1 shows the pressure drop through the P12 FPTUs when primary air flows through the units and the damper was fully open. Both of the P12C FPTUs (SCR and ECM) had a porous baffle (PB) at the outlet of the air valve. The PB was suspected as the reason for the larger pressure drop in the SCR_P12C. The ECM_P12C was chosen for use in the CFD model development because when the CFD study was conducted, the ECM_P12C FPTU was being tested in the laboratory.

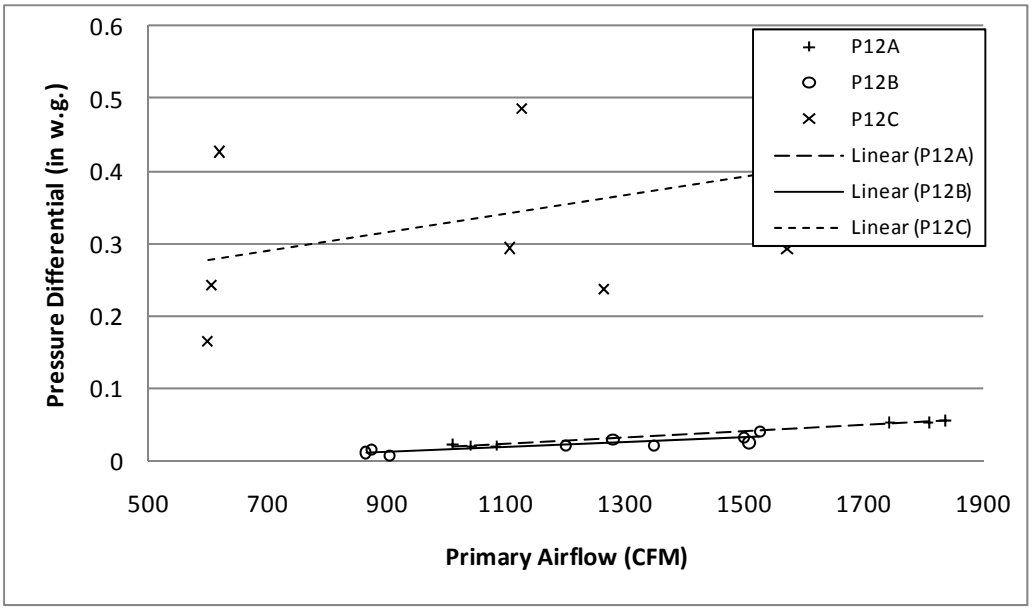

Figure 7-1: Pressure drop through P12 FPTUs as a function of the primary air flow with the damper at the fully open setting.

The geometry of the flow path of the air was different in each of the FPTUs. Figure 7-2 shows a 3-D model of the primary air flow path of P12C FPTU.

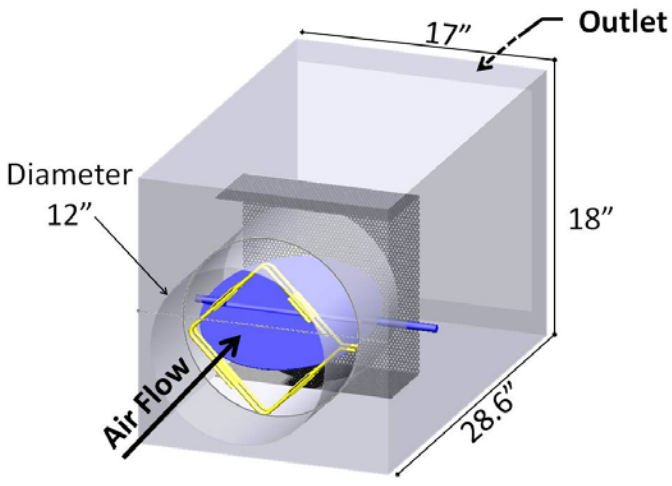

Figure 7-2: P12C FPTU modeled in SolidWorks.

Key features of the model shown annotated in Figure 7-2 formed the boundaries of the flow domain. The flow sensor, flow control damper, and porous baffle can be seen inside the terminal unit. The SW model was created from measurements made on the ECM_P12C FPTU and the accuracy of the dimensions was verified using the manufacturer's published drawings. Table 7-1 shows the dimensions of the components in the ECM-P12C FPTU.

Table 7-1: Dimensions of the components of ECM-P12C FPTU.

		Width/Diameter		Length		Height/Thickness	
	Shape	Inches	mm	Inches	mm	Inches	mm
Inlet Valve	Round	12.0	304.8	13.0	330.2		
Flow Sensor	Round Tube	0.250	6.35	22.0	558.8	0.0625	1.59
Damper	Round Disk	12.0	304.8			0.0625	1.59
Porous Baffle	Rectangle	12.0	304.8	22.0	558.8	0.0625	1.59
Mixing Chamber	Rectangle	17.0	431.8	28.6	726.4	18.0	457.2

The baseline control volume in Star CCM+ was created using the graphical user interface that was integral to the software. It was determined by experience with the software that the internal components that were developed in SW could easily be imported into Star CCM+ but that the inlet duct and terminal unit walls were more easily modeled in the Star CCM+ GUI.

The process of developing the physical model consisted of defining all of the surfaces that interacted with the fluid. In this case, the inside walls of the ducts and the FPTU formed the external boundaries of the control volume for fluid flow. The internal

boundaries that defined the flow path consisted of the flow sensor, the flow control damper and the porous baffle.

The important thing to understand about modeling the flow path is that the analysis performed for the control volume was defined by the flow path of the fluid. The walls of the terminal unit and the internal components did not define a control volume; they only defined surfaces that were part of the boundaries of the control volume. To define a control volume, the ends of the terminal unit had to be "closed" so they could also be defined as surfaces which were later treated as boundaries by the computational model.

The inlet air duct was defined as a round flat surface and the outlet of the FPTU was defined as a flat rectangular surface. During the simulation, these surfaces were defined as boundaries that had a mass flux into or out of the control volume.

Figure 7-3 shows the P12C FPTU after it was imported into Star CCM+. It was known from the operation of the FPTU that the damper position would change as the operation of the terminal unit was modeled. Because of the geometry of the damper as it rotated, the origin, point [0,0,0], was determined to be at the center of the axle of the disk that formed the damper. The initial damper position was at zero degrees (fully open) as shown in Figure 7-3.

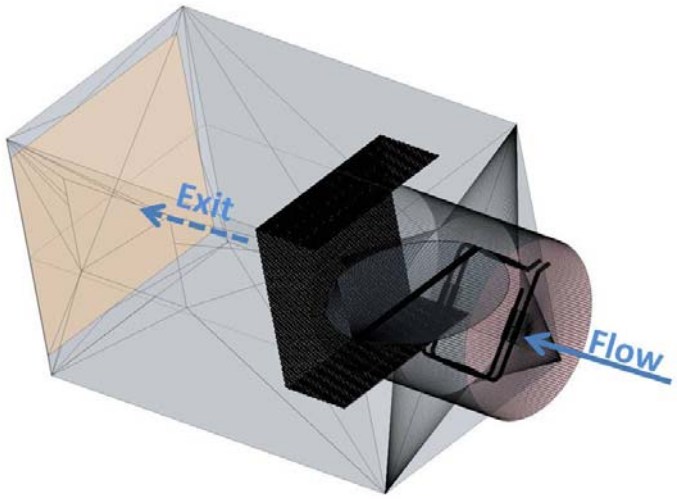

Figure 7-3: The P12C FPTU model created in Star CCM+ from importing the SW model.

The x-axis was along the centerline of the damper axle and the damper rotated about the x-axis. The z-axis was along the centerline of the inlet duct and the air flow into the duct was in the –z direction. After the terminal unit was imported into Star CCM+ from SW, the inlet air duct was "closed" with a flat round surface and the primary air supply port, which was the FPTU outlet, was "sealed" with a flat rectangular surface. The exit port is the back surface of the terminal unit as shown in Figure 7-3. The inlet air supply port is the front surface of the FPTU as shown in Figure 7-3.

After the FPTU was imported and the volume was closed, the surface was meshed using the surface wrapper utility built into the CFD software. The surface wrapper utility traced the surfaces defined by the control volume model and generated a grid of points that defined the surface boundaries of the control volume. When the surface meshes were generated, problems were encountered with the porous baffle.

Figure 7-4 shows a close up of the porous baffle after it was imported into the GUI.

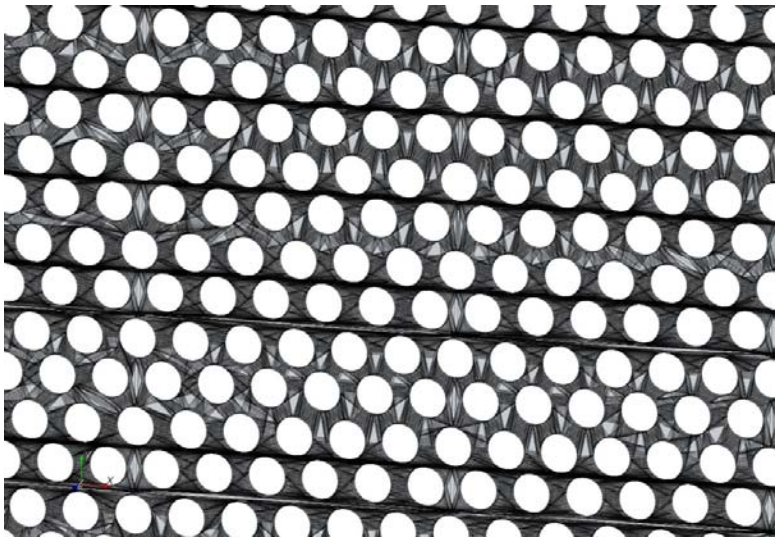

Figure 7-4: Porous baffle after it was imported into the GUI.

The 0.0625” (1.59 mm) thickness of the baffle combined 0.187” (4.76 mm) holes in the baffle that were spaced 0.25” (V-35 mm) apart, center to center, required the surface mesh to have a minimum grid resolution of 0.03937” (0.9 mm) or better, otherwise, there was a significant loss in the features of the baffle.

The thickness of the baffle and hole sizes were small when compared to the 12 inch (304 mm) diameter damper. The porous baffle was constructed from a 22 inch (558.8 mm) x 12 inch (304 mm) piece of sheet metal that was 0.0625 inches (1.59 mm) thick.

Figure 7-5 shows a close up of the surface mesh that was generated when relative target size of 0.03937 inches (1 mm) was used in combination with the relative minimum size of 0.03543 inches (0.9mm). Figure 7-6 shows the mesh that was

generated when relative minimum size setting was changed to 0.03937 inches (1.0 mm). The inputs that were used to generate the surface mesh and a description of their meaning was included in Appendix IV.

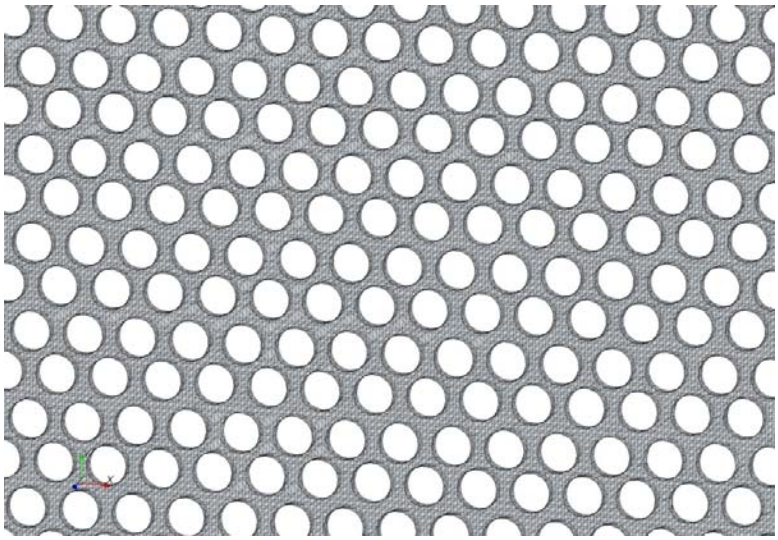

Figure 7-5: PB surface mesh using 0.03543 inches (0.9 mm) minimum setting.

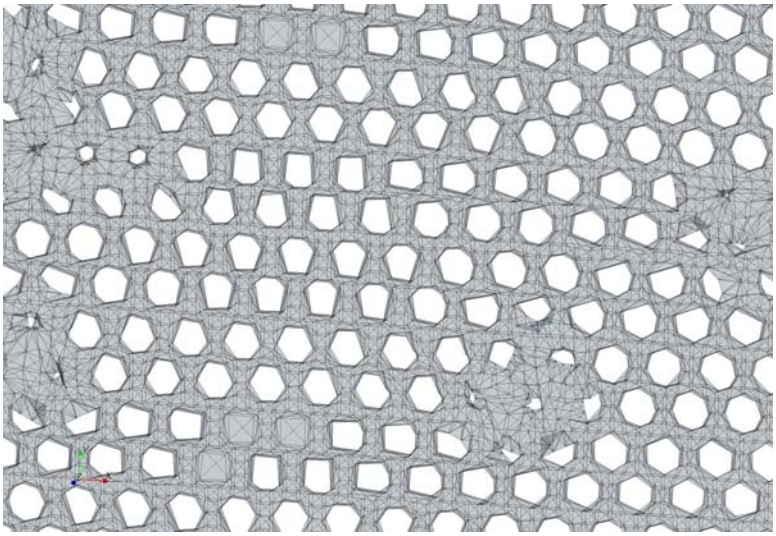

Figure 7-6: PB surface mesh using 0.03937 inches (1.0 mm) minimum setting.

Problems were encountered during initial attempts to model the geometry by importing the FPTUs created with SolidWorks. The problems were the result of the requirement that to generate a surface mesh, the 3-D geometric model had to be a completely closed volume and all external surfaces had to be completely closed.

When the SW model was imported, the internal and external surfaces of the FPTU were created in the CFD GUI interface. To create the surface mesh, the user had to distinguish between the internal FPTU walls that were part of the boundaries and the external FPTU walls that were not relevant to the simulation. Due to the import process, it was very difficult to remove unnecessary features and quite often the surface wrapping utility became confused by the extra surfaces. By experience with the software, the best solution was to delete all of the imported geometry except the internal components. The GUI interface for the CFD software had built-in utilities that allowed the user to easily add the boundaries required to complete the surfaces included in the simulation.

The process evolved to where the flow sensor, damper, and porous baffle were designed in SW and were then exported to a standard format one component at a time and were then imported into the Star CCM+. As each internal component (flow sensor, damper, porous baffle) was imported into the Star CCM+ model, it was placed at the proper xyz location using the appropriate GUI tools.

After the flow sensor, damper, and porous baffle were imported, the control volume was enclosed and the surface mesh was generated using the GUI tools built into the Star CCM+. The process consisted of selecting various options and letting the software develop the meshes. Star CMM+ used the Finite Volume (FV) method for solving the

NS equations. The FV method can be used with both structured and unstructured grids. Star CMM+ used unstructured grids for surface and volume meshes.

The term "unstructured grid" applies when the cells within the computational domain are allowed to be freely assembled based on the geometry of the control volume. The cells are usually constructed using triangles in two dimensions or tetrahedrons in three dimensions (Tu et al 2008).

Although the Star CCM+ software handled a lot of the details during mesh generation, the user had to guide the program through the process. For example, if the user-selected inputs led to a course grid, then a lot of the detailed surface features were ignored and their impact on the solution was lost, as demonstrated in Figures 7-4 through 7-V- The user had to be careful to ensure that surface features were not lost at locations where surfaces intersected or where surfaces were in close proximity to each other. For example, the flow sensor was in close proximity to the surface of the round duct inside the inlet air valve. Using features built into the program, care was taken to ensure that the flow path between the sensor and the duct wall was not covered during the surface meshing process.

After the surface meshing was complete and the entire flow path was enclosed by a closed surface, the volume mesh was generated. In a manner similar to the surface generation utility, the program provided built-in utilities that allowed the user to define an unstructured volume mesh that was based on user-controllable parameters and the previously generated surface mesh.

Experience showed that the control volume mesh generation process was the bottle-neck in the process. The mesh generation algorithms did not use parallel processing and, as a result, the process was slow. The mesh generation process was also very memory intensive. If a large volume mesh was generated, the mesh algorithms would often run for several days before the program crashed due to some internal memory error.

A volume mesh was achieved at one point during this process but unfortunately, when the physics model was added and the simulations were performed, convergence was never achieved. The conditions that were used to determine convergence are discussed with the physics model.

Because the simulation never converged, a finer grid resolution was required to properly model the porous baffle. The failure to achieve convergence with the whole unit simulation is discussed in greater detail in the section that describes the convergence criteria and grid independence.

After numerous attempts to generate volume meshes with different levels of detail, experience with the software showed that the porous baffle was going to require a finer grid than the rest of the FPTU. The fine mesh of the baffle then required a fine mesh over the remainder of the volume, which was not practical for a graphics workstation used by the average engineer. At this point, the best strategy was to investigate other options for handling the baffle.

Several options were available for handling the porous baffle which consisted of using the PB interface built into the software and/or breaking the FPTU into several distinct regions that could be joined together to perform the simulation. A region was

defined as a volume enclosed by specific boundaries in 3-D space. An interface was a mechanism that allowed multiple boundaries to be joined together. The software had six interface types which consisted of the baffle, contact, fan, fully developed, internal, and the porous baffle. The PB interface (PBI) was chosen as a model for the PB mesh.

The two interface types of interest for this thesis were the internal and the porous baffle. The internal interface allowed two regions to exchange mass and energy as if there were no boundary between the regions. The porous baffle interface allowed mass and energy to flow through the boundary between the two regions with a pressure drop that was a function of the velocity of the fluid normal to the face of the boundary. The internal interface was used to join free-flow boundaries together and the PBI was used to model the porous baffle mesh.

Multiple regions with the PBI

The FPTU was divided into two regions: the inlet air valve (IAV) and the mixing chamber (MC). Figure 7-7 shows the IAV region after the surface mesh was generated. The PBI interface can be seen in the figure and consisted of the front face of the volume plus the small rectangular surfaces connected at the top and bottom. The free flow areas were the rectangular surfaces connected to the sides of the PBI. The velocity inlet face was identified as the flat round surface that was connected to the inlet duct walls. The flow sensor and flow control damper can be seen inside the IAV. The mixing chamber was a rectangular volume that had a surface region that matched the end of the IAV.

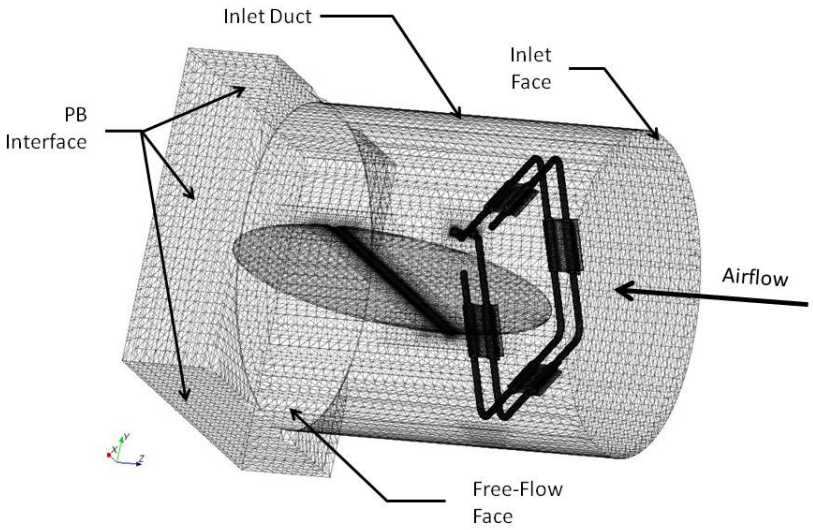

Figure 7-7: The IAV surface mesh.

After breaking the FPTU up into distinct regions, the surface and volume meshing was done for each region one at a time, which required fewer computational resources than for the entire FPTU as single volume.

Although the CFD software literature claimed the PB boundary condition could be used, it did not describe the flow patterns after the baffle except to say that it was assumed by the CFD software that the direction of the fluid flow remained unchanged as it crossed the baffle.

The geometry of the PB as it was installed in the FPTU had fluid flow pathways around the baffle along the sides of the terminal unit. Free flow areas were on both side of the IAV section with the visible side shown in Figure 7-7 and labeled “Free Flow Face.”

To use the PBI, the user had to have a relationship between the pressure drop across the PB and the face velocity of the fluid that passed through the baffle. The user also had to input the porosity of the baffle if it was being used to model heat transfer. Equation 7-1 was used by the CFD software to calculate the pressure drop across the PBI.

$$\Delta p = -\rho(\alpha|v_n| + \beta)v_n \tag{7-1}$$

In equation 7-1, ρ was the fluid density at the interface, v_n was the velocity of the fluid normal to the baffle surface and α and β were user-specified coefficients.

The initial coefficients for equation 7-1 were estimated from laboratory measured data in combination with the simulations. The laboratory-measured pressure drops for the terminal unit with the inlet air valve full open were used to refine $\propto$ and β. The procedure consisted of running simulations at inlet face velocities of 5 m/s, 10 m/s, and 20 m/s and comparing the results to the measured data for damper position setting of zero degrees. Based on visual inspections of the graphed simulated data and the measured data, adjustments to refine $\propto$ and β were made until the simulated data was along the same line as the measured data.

From the measured data, the coefficients were estimated to be as follows: $\propto$ = 1.441(non-dimensional) and β = 0.750 m/s. From the SolidWorks model the porosity was 0.547, which was also a non-dimensional constant.

Development of the sections used in final analysis

Based on the introduction of the PBI, it was determined that the best strategy to use for creating the control volume model was to divide the FPTU into two sections that were separated by the two interfaces that represented the PBI and a free-flow area that represented the opening around the porous baffle boundary.

The inlet section used in the final analysis shown in Figure 7-7 was created as a stand-alone section so that the disk in the inlet valve could be adjusted to model operation of the terminal unit at various damper settings. After the inlet section was modeled, the surface and volume meshes were generated and it was exported to a volume mesh file for use in the simulation. Each damper setting was modeled and a separate volume mesh file was created for use with the simulations.

The exit section was created in a similar manner to the inlet section except that only one volume mesh file was created.

The physics model

The physics model in the CFD software consisted of the data that described the properties of the fluid, the boundary conditions and the equations that described the fluid flow. The CFD software provided a graphical user interface where the user selected the materials, the boundary conditions, and the equations. As the user worked through the input screens, the choices selected and the data entered determined the application of the appropriately simplified form of the NS equations.

This section focuses only on the selections that were made and the data entered when the final physics model was developed. There were numerous inputs in the physics model and the details of the simulation inputs were included in Appendix 5.

The continuum was the control volume that defined the air flow path through the FPTU. For this research, the continuum was modeled as a three-dimensional, steady-state, non-moving space. The control volume was modeled as three dimensional because of the complex nature of the flow path through and around the porous baffle. All of the laboratory experiments were steady state so the CFD model was also steady state. The non-moving reference frame was chosen because, in each case, no parts were moving within the control volume defined by the body of the FPTU. Although the damper position changed from one simulation to the next, the damper was not moving during an individual simulation.

The choice of the materials was determined by the problem and for this project, air was the working fluid. The conditions for the working fluid as defined during the simulation were standard conditions of temperature and pressure (20 C, 101 kPa, dry air) and the flow was considered to be incompressible with constant properties.

The properties were considered as constant because there was no significant variation in temperature as the air passed through the FPTU. The flow was considered incompressible because at the highest flow rate, the Mach number of the air was 0.06, which was well below 0.3 needed to assume incompressible flow. For the simulations, the density of the air was 1.18415 kg/m^3 and the dynamic viscosity was 1.85508 x 10^{-5} Pa-s.

The flow was modeled as segregated flow using a second order upwind convection scheme. For the flow model, the secondary gradients option was selected. The segregated flow model solved the flow equations for pressure and velocity in an uncoupled manner. The continuity and momentum equations were linked through a predictor-corrector approach using a colocated variable approach and a Rhie-and-Chow-type pressure-velocity coupling combined with a SIMPLE-type algorithm (CD-Adapco, 2009) which handled only incompressible or mildly compressible flows. This model was chosen automatically by the CFD software when the selection of incompressible flow was made by the user.

The flow was modeled as turbulent flow using a Reynolds Averaged Navier Stokes (RANS) approach. RANS was selected by the CFD software after the user selected the standard K-Epsilon (K-Ɛ) turbulent model. The turbulent model was chosen based on the range of Reynolds numbers for the flow rates that were to be modeled. For this project the maximum inlet velocity was 20 m/s ($Re = 3.9x10^5$) and a minimum inlet velocity of 1 m/s ($Re = 1.9\ x10^4$).

Once the user selected the basic turbulence equation, the CFD software automatically made selections for components of the model. With the selection of the standard K-e model, the software selected the Realizable K-Epsilon two-layer model for the wall treatment. In support of this option, the software also selected the two-layer, shear driven Wolfstein (1969) type model with a second order convection model. Other selections made by the software were as follows:

1. The normal stress term was not enabled.

2. Secondary gradients were on (enabled).
3. Buoyancy production of dissipation was boundary layer orientation.
4. Constants for the equations: C_{μ}=0.09, $C_{1\varepsilon}$=1.44, $C_{2\varepsilon}$ =1.9, C_t=1.0, $C_{\varepsilon ta}$=50.0, Sigma_k=1.0, Sarkar=2.0, $T_{k\varepsilon}$ Minimum = $1.0x10^{-10}$, and T_{dr} Minimum = $1.0x10^{-10}$.
5. All wall treatment was two-layer.
6. Minimum allowable wall distance was $1.0x10^{-10}$ m.
7. Reference pressure was 101.325 kPa.

K-Epsilon models are generally well suited to industrial applications that involve complex flow (CD-Adapco 2009) and are popular with many computer codes (Schetz 1993). K-Epsilon models have been studied extensively and one of the more recent developments is the realizable K-Epsilon model developed by Shih et al. (1994). The realizable k-Epsilon model in the CFD software was implemented with a two-layer approach which enabled the models to be implemented with fine meshes that resolved the viscous sub-layer near the boundary. The Realizable Two-Layer K-Epsilon model combines the Realizable K-Epsilon model with the two-layer approach. The coefficients of the models are identical and the model gains the flexibility of an all y^+ wall treatment.

When the realizable K-Epsilon model was selected, the two additional properties that had to be selected were the "two-layer type" and the "convection scheme." Both properties were automatically selected by the software. The two-layer type was selected as the shear driven two-layer formulation of Wolfstein (1969), which is appropriate for flows that are not dominated by buoyancy; the buoyancy-driven model was the other

choice. The convection model selected was the second-order upwind scheme; the first-order scheme was the other choice. The advantage of the second-order scheme over the first-order scheme was that it was nominally more accurate (CD-Adapco 2009).

There were a final set of inputs to the model that were categorized by the CFD software as "expert" inputs. What this meant was that unless the user was enough of an expert that he understood how the software did the calculations at a very detailed level, he should not modify the values. For this project, the expert coefficients were left as the default values supplied by the software.

The Reynolds (Re) numbers for this project were all below $3x10^6$, which meant all of the simulations fell into the region of low-Reynolds number flow (Shames 1992). A low-Reynolds number K-Epsilon model is one that can be used to resolve the viscous sub-layer. The two-layer approach is an alternative to the low-Reynolds number approach that allows the K-Epsilon model to be applied in the viscous sub-layer (CD-Adapco 2009).

Several two-layer formulations have been proposed and the two implemented by the CFD software were the shear-driven and buoyancy-driven methods. The advantage of the two-layer formulations was that they work with low-Reynolds number meshes ($y^+ \sim 1$) and wall-function type meshes ($y^+ > 30$). Due to the nature of the unstructured grids used by the CFD software combined with the refined level of meshes that were required to model components inside the FPTU, the model required both low-Reynolds meshes as well as meshes that were far from the wall. The two-layer, realizable K-Epsilon model seemed to be the appropriate choice for the analysis of the FPTU.

Entrance length and fully developed flow

The primary air flow into the inlet air valve was modeled as a constant face velocity air stream. There were numerous references in the literature that discussed the entry length for turbulent flow. The entry length for the inlet velocities of interest were estimated using $L_e = 1.4\ Re^{1/4}D$ (Denn 1980). With this equation the entrance length at maximum velocity was 35D. Denn (1980) stated that the experimental rule of thumb was 40D for turbulent flow. Fox et al (2004) reported that the mean velocity profile was fully developed within 25 to 40 diameters but that the full details of the flow may not develop for 80 or more diameters.

The length of duct that was used to supply air to the FPTU during the experiments was about 10D, which was substantially lower than 35D to 40D. In addition to the short entrance length to the FPTU, the experimental setup also had a flow control damper that was at the entrance of the straight duct that supplied the primary air to the FPTU. For all cases, the primary air control damper at the inlet of the duct that supplied air to the inlet valve of the FPTU provided some level of disturbance to the primary air flow. Velocity profile measurements for air entering the primary air valve of the FPTU were not made.

To perform the simulations, an entering air velocity profile had to be assumed. Based on the 35D to 40D estimates in combination with the short entry lengths, it was assumed that a fully developed velocity profile did not correctly represent the actual flow when the experimental work was done. For the CFD analysis, it was decided that a constant face velocity at the inlet air valve was the best boundary condition to use for the primary air supply.

The assumed constant face velocity profile was based on the anticipated differences between a fully developed velocity profile and a flat velocity profile. The velocity profile for turbulent flow through a smooth pipe can be approximated with equation 7-2 (Fox et al. 2004).

$$\frac{\bar{u}}{U} = \left(1 - \frac{r}{R}\right)^{1/n} \tag{7-2}$$

where n was approximated with equation 7-3.

$$n = -1.7 + 1.8\log\left(Re_U\right) \tag{7-3}$$

Figure 7-8 shows a graph of the velocity profile for the maximum and minimum entering velocities used to model the FPTUs. It can be seen from Figure 7-8 that fully developed velocity profiles are relatively flat. Equation 7-4 was used to estimate the ratio of the average velocity to the centerline velocity for the maximum and minimum entering velocities used in the CFD analysis.

$$\frac{\bar{V}}{U} = \frac{2n^2}{(n+1)(2n+1)} \tag{7-4}$$

For the maximum velocity, V=20 m/s, the ratio was 0.84 and for the minimum velocity, V=1 m/s, the ratio was 0.79. The equations show that the higher the Reynolds number, the flatter the velocity profile and that in the range of flow for this project, the

velocity profiles were nearly flat. If the velocity profile was exactly flat, then the average velocity would be the same as the centerline velocity. In the absence of a velocity profile measurement and since the velocity profiles for fully developed flow are nearly flat and the centerline velocity for fully developed flows is only slightly higher than the average velocity for the range of flows used during this project, it was decided that using a flat velocity profile at the entrance to the FPTU would be a reasonable approximation.

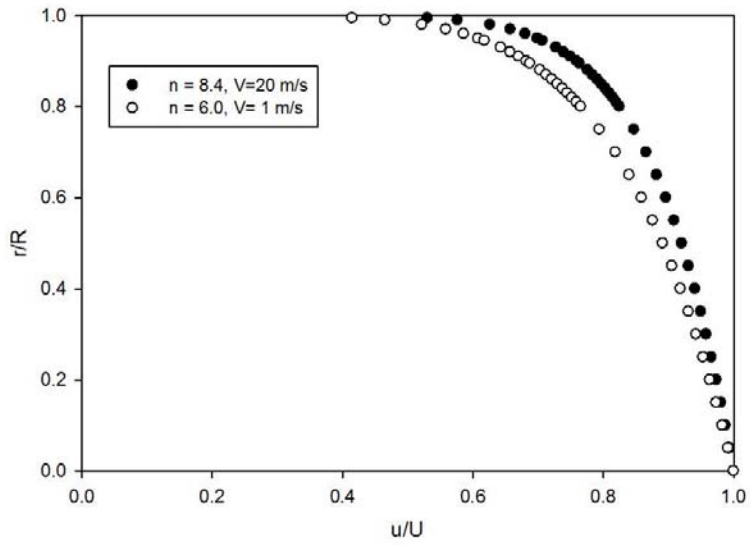

Figure 7-8: Velocity profiles for fully developed turbulent flow for maximum inlet velocity of 20 m/s (n=8.4) and 1.0 m/s (n=V-0).

Achieving grid independence and convergence

Grid independence was achieved when the simulation results did not improve when the size of the cells in the mesh were reduced beyond a certain point. Convergence was

achieved when certain user-determined simulation performance criteria were met based on the judgment of the user as to what was appropriate for the application under study. Grid independence and convergence were related and quite often the convergence criteria cannot be met without a sufficiently refined grid that enabled an accurate approximation to the NS equations.

Grid independence was achieved after numerous runs of the basic physics model in combination with refinements to the space model. The procedure was to start out with a rough grid and then run the simulation. The convergence criteria were the residuals from the equations in the physics models and the pressure drop through the FPTU. The residuals for the equations were determined and displayed automatically by the software. The residuals that were related to equations included Tdr, Tke, X-momentum, Y-momentum, Z-momentum, and continuity. The residuals represented the summation of errors in the equations over the simulation domain. For example, the continuity residual represented the loss of mass flow through the system from the entrance of the FPTU to exit of the FPTU.

There were not a lot of guidelines in the literature regarding the meaning of the residuals or a determination as to when a simulation could be considered as "converged." The CFD software user's manual recommended letting the simulation run until the residuals had dropped several orders of magnitude (CD-Adapco 2009). Tu et al. (2008) recommended that when the residuals had dropped three orders of magnitude, the simulation could be considered as qualitatively converged. It was further recommended that scaled energy residuals should converge to a tolerance of 10^{-6}, while

scaled species only needed to converge to a tolerance of 10^{-5}. For this project the equations were considered converged when the residuals converged to the tolerances suggested by Tu el al (2008).

Because the laboratory measurements consisted of pressure drops across the FPTU, an additional constraint for convergence was the when the pressure at the entrance and the exit of the FPTU stabilized and did not change more than 0.1 Pa between iterations. The exit pressure was set at 125 Pa and the inlet pressure was always higher than the exit pressure. Using a monitored field value as additional criteria for convergence was a practice recommended by Tu et al (2008).

Boundary conditions and initial conditions

The major boundary conditions for this project were defined by the inlet face velocity, the outlet pressure, and the internal & external surfaces of the FPTU. The CFD software required a significant number of detailed inputs to describe the physics of the boundary conditions. The detailed inputs for all boundary conditions were included in the appendix. The inlet face velocity was set to the particular value of interest for each simulation. The exit was treated as a pressure exit and was set for 125 Pa (0.5 in. w.c.) for all operating cases and was chosen because it was the downstream static pressure used when the parallel FPTUs were tested in the laboratory. The detailed initial conditions were included in the appendix and the major initial conditions consisted of setting the velocity throughout the FPTU to zero m/s.

CHAPTER VIII

CFD MODEL RESULTS

This chapter describes the results of the CFD simulation and includes the output from the major steps that led to the final model. The "whole unit" simulation results are presented first and are followed by the final model. The final section includes a discussion of the results and how they compare to the measured data.

The whole unit simulation

The initial attempts to model the FPTU consisted of trying to build a single control volume model of the FPTU and to then build a CFD model that would converge over the whole region of the control volume. The problem with the single control volume model was that it was not possible to achieve the minimum resolution of the surface meshes that would adequately resolve the details of the features of the flow path inside the FPTU. The finer the mesh used by the control volume model, the greater the cost of the model in terms of computer resources and computational time. A control volume model was created that was believed to be sufficiently detailed to simulate the operation of the FPTU.

After the control volume model was created, a physics model was created and the simulation was attempted. Initial simulation runs were so unstable they immediately diverged and, even with attempts to bring the simulations under control by reducing the under-relaxation factors for velocity and pressure as well as changing to the first order upwind convection scheme, the simulations were never close to converging.

As a result of the initial simulations, numerous combinations of improved grid resolutions and fluid model options were tried. Improved grid resolutions were tried by adjusting the base size from 100 mm to 10 mm, the relative target size from 10 mm to .1 mm, and the relative minimum size from 10 mm to .1 mm. In addition to adjusting the grid resolution, the K-Omega turbulence model was tried. The case presented here shows the best results of all of the variations.

Figure 8-1 shows the 3-D finite volume mesh of the whole unit simulation. The figure shows air entering the inlet air valve from the right at a face velocity of 10 m/s and includes a section in the x-z plane that shows the velocity vectors of the air as it passed through the terminal unit. The plane section was on the centerline of the terminal unit. The air entered the terminal unit from the right side of the figure through the inlet air valve entrance and then passed through the porous baffle into the mixing chamber, where it exited out of the back of the unit through the exit port.

The grids shown on the walls of the FPTU varied in size and were smaller close to the front of the unit compared to the cells near the exit. Star CCM+ allowed the user to set “high-level” settings for the control volume model that were used automatically when creating the surface and volume meshes. Star CCM+ allowed the user to over-ride the global control volume grid control settings and assign settings for specific surfaces in the model. The dark regions shown in Figure 8-1 are regions where the cells were created from surface grid control settings that were specific to each surface.

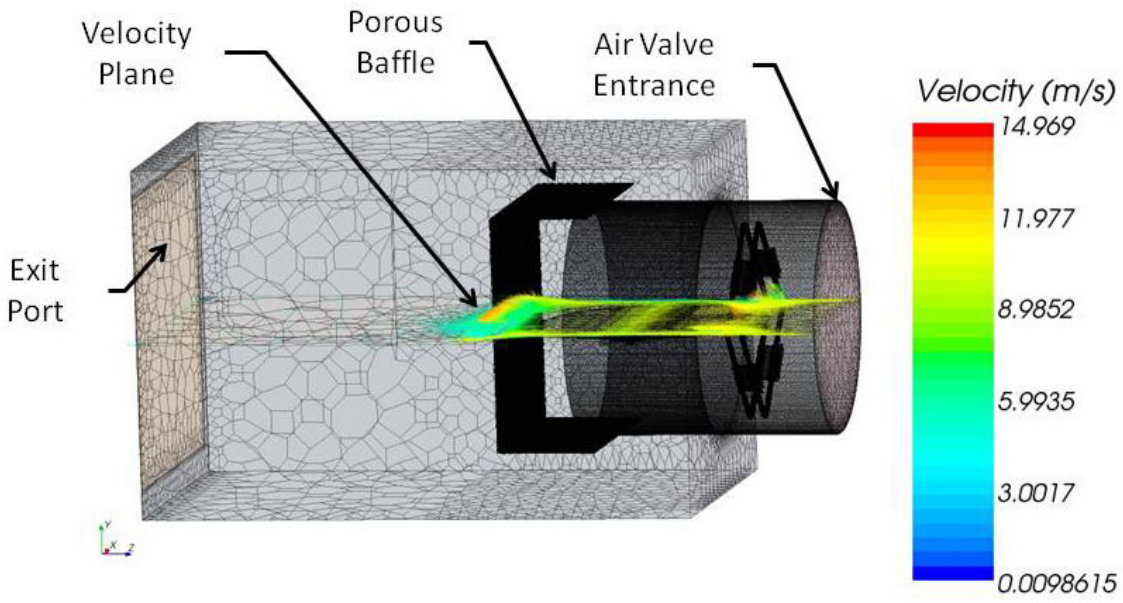

Figure 8-1: Parallel FPTU with primary air entering the inlet valve from the right side at a constant face velocity of 10 m/s.

The surfaces in the inlet air valve used a relative minimum size setting of 0.00394 inches (0.1 mm) and a relative target size of 0.0394 inches (1.0 mm). With these settings, the software automatically generated more refined (smaller) surface meshes for the parts. Star CCM+ had built-in restrictions on the allowable rate of change of the size of cells that were next to each other. When it generated the volume meshes, it automatically controlled the growth rate of the cells that connected the volume between surfaces of different grid resolutions.

The built-in growth controls of Star CCM+ forced higher density grids to be built at the end of the FPTU where the air valve and its components were located and in the region surrounding the porous baffle mesh.

Figure 8-2 shows a top view of the velocity vector plane section. The figure shows that some of the air passed through the porous baffle and that the rest of the air went around the baffle. As the air passed through the baffle, it increased in speed and then slowed down as it expanded into the mixing chamber. The figure shows that the air that went around the baffle accelerated as it entered the mixing chamber and it later slowed to a velocity close to the velocity of the air that had passed through the baffle.

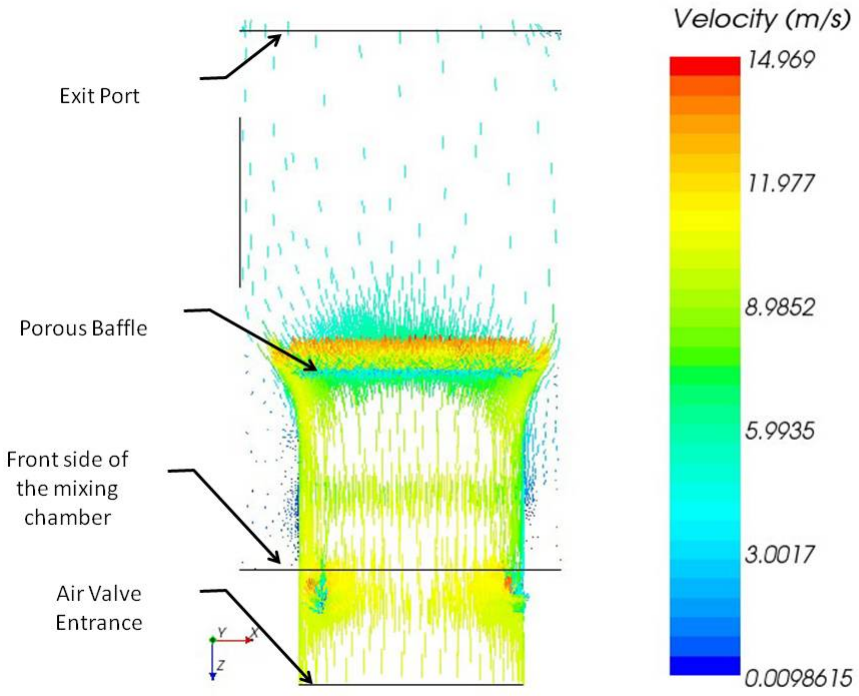

Figure 8-2: Velocity vector distribution of a Parallel FPTU with primary air entering the inlet air valve at a constant face velocity of 10 m/s.

Figure 8-2 shows that after the air crossed into the mixing chamber, its velocity was about half of its velocity when it entered the air valve. The inlet face velocity was 1968

ft/min (10.0 m/s) and the average face velocity at the exit estimated by the CFD software was 4.7 m/s. The drop in velocity was due to the increased cross sectional area of the flow path. The inlet port had a cross-sectional area of 113 in^2 (72,903 mm^2) and the outlet had an area of 240 in^2 (154,838 mm^2). With the constant density assumption the average outlet velocity was estimated by hand calculations to be 925 ft/min (4.7 m/s), which was the same as the average velocity calculated by the CFD software.

Figure 8-2 shows the velocity vectors for the flow as it exited the back of the porous baffle and also shows that the high velocity flow leaving the porous baffle did not extend more than about an inch from the back side of the baffle.

Figure 8-3 shows the static pressure distribution within the Parallel FPTU and also shows that a high pressure region developed in front of and a low pressure region developed behind the porous baffle. Figure 8-3 also shows that the static pressure disturbance caused by the PB extended only a few inches behind the baffle.

Figure 8-3 shows that the pressure gradients were not significant for flow that was a few inches away from the porous baffle and that there was a slight pressure drop as the air passed around the flow sensor.

Figure 8-4 shows a contour map of the velocity of the air as it left the exit port of the FPTU. The figure is a view from the back of the terminal unit where the large region of higher velocity flow was on the side of the FPTU that had the smallest distance between the edges of the porous baffle and the wall of the mixing chamber.

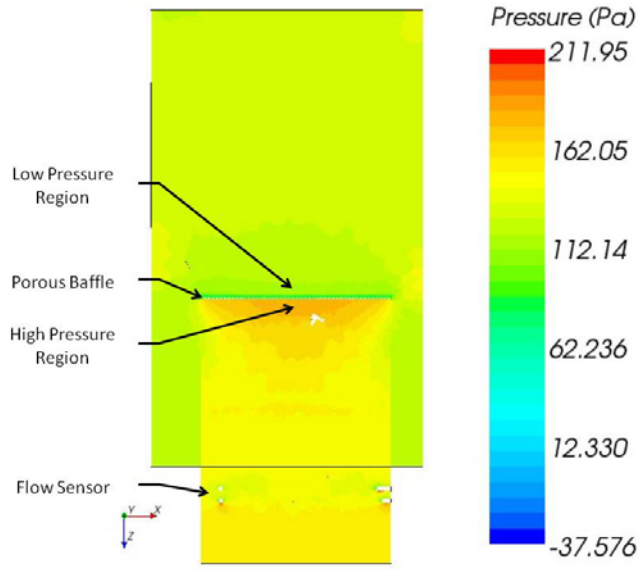

Figure 8-3: Static pressure distribution inside a Parallel FPTU with primary air entering the inlet air valve at a constant face velocity of 10 m/s.

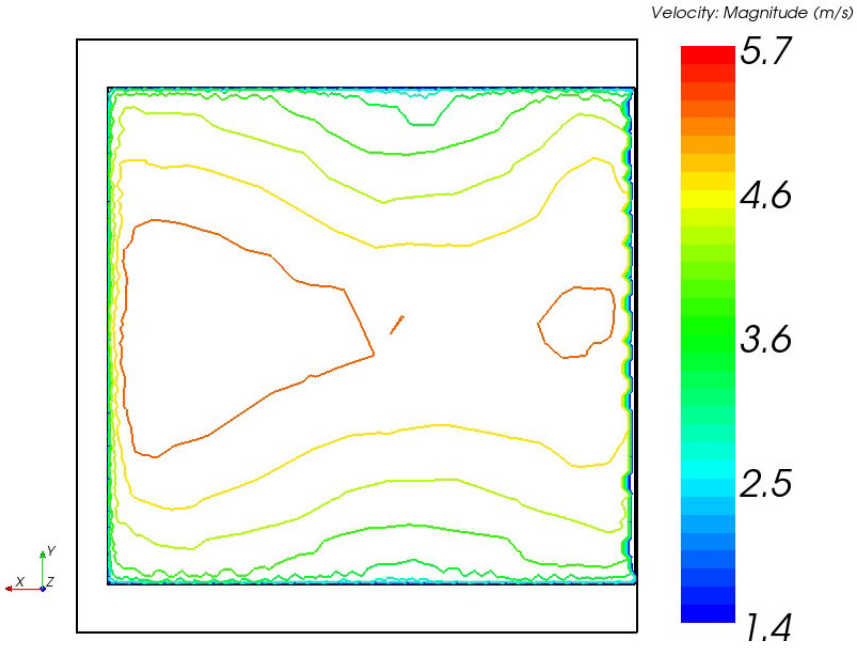

Figure 8-4: Contour map of the velocity of the air as it left the exit port of the Parallel FPTU with primary air entering the inlet air valve at a constant face velocity of 10 m/s.

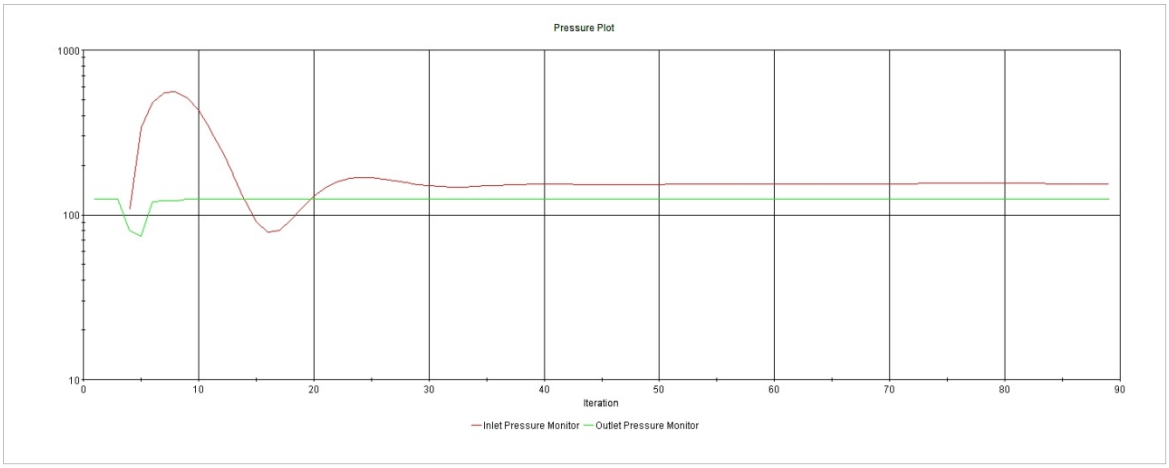

Figure 8-5: Plot of the inlet and outlet pressures as simulation progressed from start until the execution was terminated.

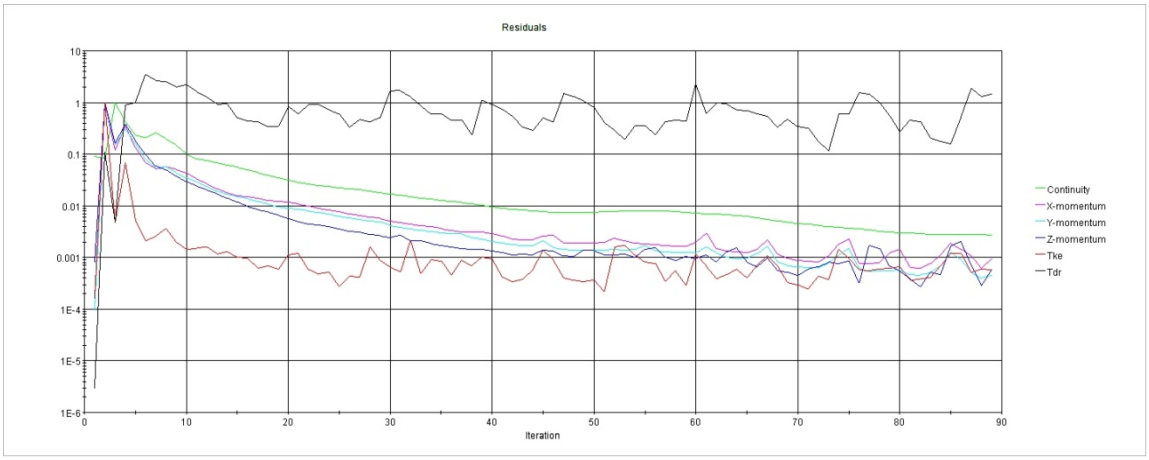

Figure 8-6: Plot of the residuals as the simulation progressed from start until the execution was terminated.

The differences between the inlet and outlet pressures were used to calculate the pressure drop through the FPTU. The pressure drop measured in the laboratory was compared to the pressure drop calculated between the inlet and outlet of the FPTU and was used to verify the CFD model.

Figure 8-5 shows a plot of the inlet and outlet pressures of the FPTU during the execution of the simulation. The stability of the inlet and outlet pressures was considered a key parameter for the determination of when the simulation converged. Figure 8-6 shows a plot of the residuals during the execution of the simulation. The plot of the residuals and the pressures show that the simulation was terminated at 89 iterations.

The residuals from the calculations were also used to determine when the simulation converged and were often used to determine when the simulation either had not converged or was not going to converge. Figure 8-6 shows that the residuals did not drop sufficiently for the simulation to be considered as a converging model. The residual for the turbulence dissipation rate, T_{dr}, never dropped significantly and was actually becoming less stable. At 80 iterations, the residuals for the directional momentums and the kinetic energy, T_{ke}, had dropped only three orders of magnitude and were becoming more unstable. Experience indicated that the trend was toward increasing instability so the simulation was stopped at 89 iterations.

The WUPBI simulation

The WUS was modified and the PB was replaced with the PBI to create the whole unit simulation using the porous baffle interface (WUPBI). The WUPBI used the coefficients developed with the measured data from the laboratory experiments. The physics model used the same equations and parameters that were used with the whole unit simulation that generated the most stable results. After the control volume and

physics models were set up, the simulation was executed; convergence was achieved after additional refinements in the 3-D grid.

Figure 8-7 shows the plot of the inlet and outlet pressures for the WBPBI as the simulation progressed to convergence. Figure 8-8 shows the plot of the residuals for the WBPBI as the simulation progressed to convergence. All of the convergence criteria were met for the residuals and the pressures.

After grid independence was achieved, the model was used to estimate the pressure drop across the FPTU for the case of the damper position of zero degrees (0°) with inlet face velocities that varied from 5 m/s to 20 m/s. The results from the simulations were used to adjust the coefficients of equation 7-1 until the pressure drops matched the measured data. The final value for the coefficients were $\alpha = 1.441$ and $\beta = .750$ m/s.

Figure 8-9 shows a top view of the velocity vector plane section. The figure shows that some of the air passed through the porous baffle and that the rest of the air went around the baffle in a manner similar to that of the WUS. As the air passed through the baffle, its speed did not change significantly. The figure shows that air that went around the baffle accelerated as it entered the mixing chamber and that it later slowed to a velocity close to the velocity of the air that passed through the baffle.

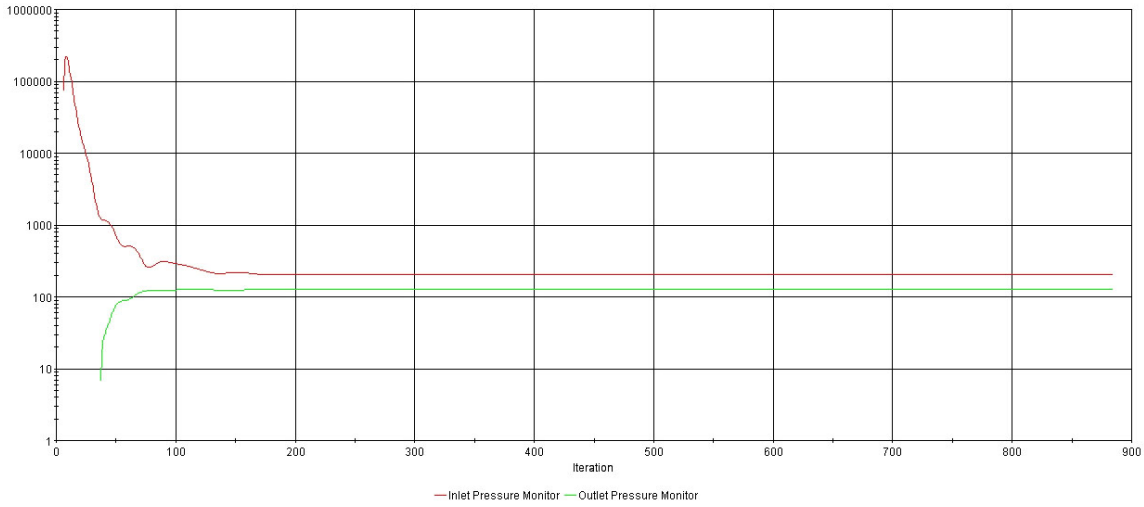

Figure 8-7: Plot of the inlet and outlet pressures as the WBPBI simulation progressed from start until the execution was terminated.

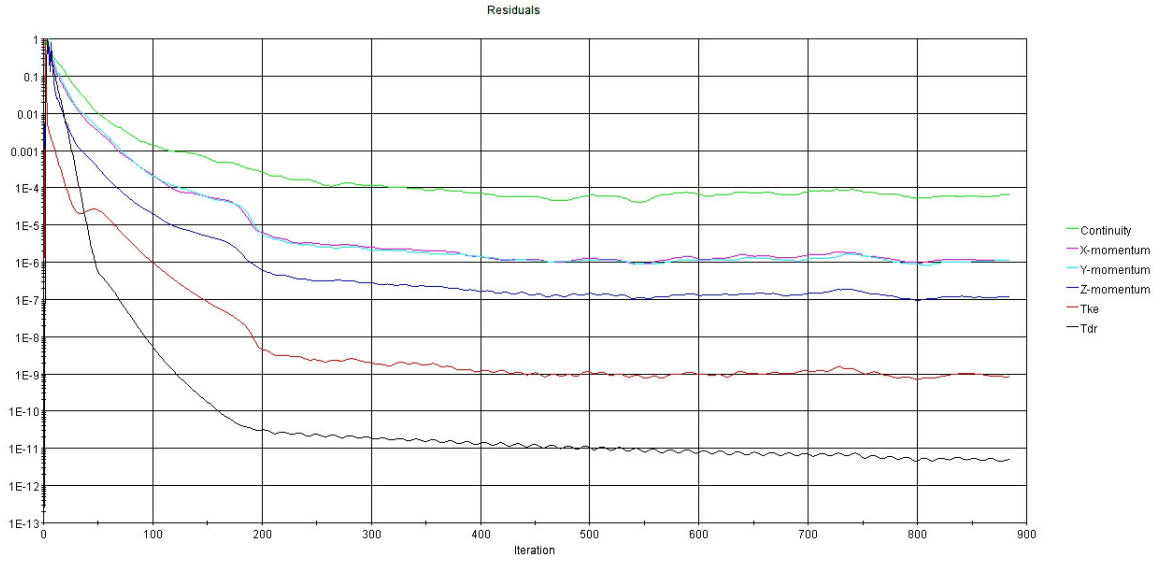

Figure 8-8: Plot of the residuals as the WBPBI simulation progressed from start until it the execution was terminated.

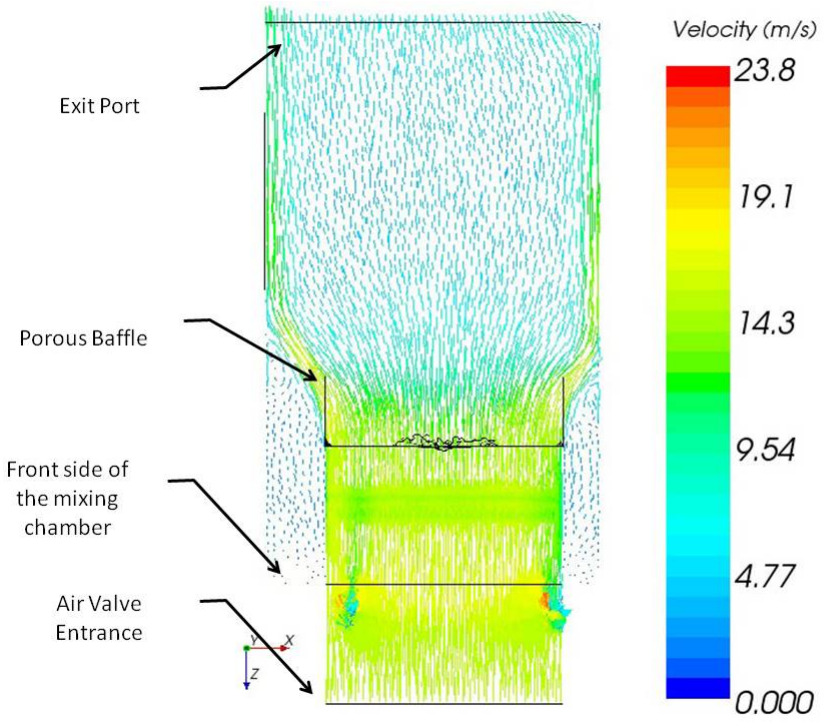

Figure 8-9: Velocity vector distribution of the WBPBI with primary air entering the inlet air valve at a constant face velocity of 15 m/s.

Figure 8-9 shows that after the air crosses into the mixing chamber, the velocity was about half of the velocity of the air when it entered the air valve. The inlet face velocity was 15.0 m/s and the average face velocity at the exit estimated by the CFD software was 7.9 m/s. As with the WUS, the drop in velocity was due to the increased cross-sectional area of the flow path.

Figure 8-10 shows the static pressure distribution within the WBPBI. Figure 8-10 shows the high pressure region that developed in front of and the low pressure region that developed behind the porous baffle interface. The high-pressure regions before and after the PBI have the same distribution as for the PB in the WUS.

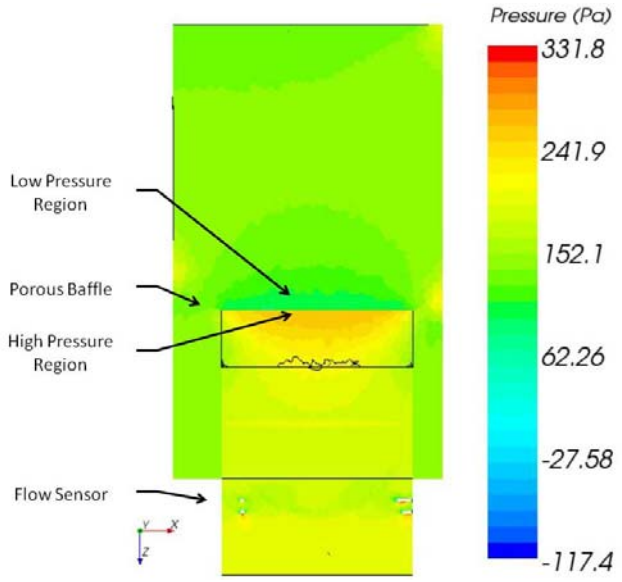

Figure 8-10: Static pressure distribution inside the WUPBI with primary air entering the inlet air valve at a constant face velocity of 15 m/s.

Figure 8-10 shows that there was a slight pressure drop as the air flowed past the flow sensor. The new information from the WUPBI simulation was the small pressure gradient near the exit port.

Figure 8-11 shows a contour map of the velocity magnitude of the air as it left the exit port of the FPTU for the WUPBI simulation. Figure 8-11 shows the flow from the back of the terminal unit and that the contour lines indicated a greater variation of air speed near the walls of the FPTU than were indicated by the WUS results. Figure 8-11 shows a large core of air with a uniform velocity in the center of the exit port.

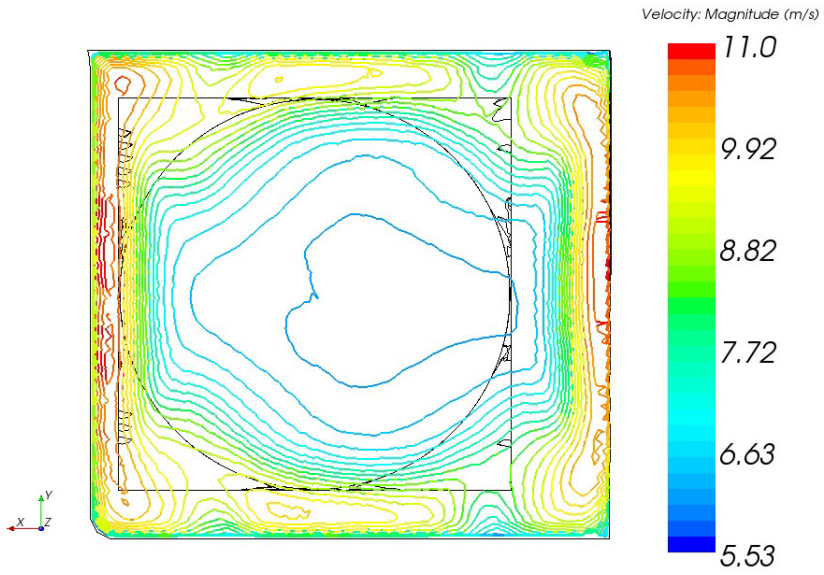

Figure 8-11: Contour map of the speed of the air as it leaves the exit port of the WBPBI with primary air entering the inlet air valve at a constant face velocity of 15 m/s.

The reason the flow was different on one side of the terminal unit relative to the flow on the other side was that the inlet air valve was positioned off-center in the mixing chamber so more air flows along one side of the terminal unit relative to the other side.

Simulation results for damper positions from 0 degrees through 67.5 degrees

Laboratory measurements were taken at various flow rates for damper positions of 0°, 22.5°, 45°, and 67.5°. The WUPBI simulation for a damper position of 0° was considered the baseline for all of the simulations after convergence was achieved, and the PBI coefficients were adjusted so that the pressure drop across the FPTU matched the measured data.

Simulations for each of the required damper positions were created by adjusting the inlet air valve damper positions of the inlet air valve model to positions 22.5°, 45°, and

67.5°. At each damper position, a new volume mesh was generated for the inlet air valve region, and the mesh was exported and saved.

After the inlet air valve volume meshes were created for each of the required damper positions, a new simulation was created for each damper position by using the baseline simulation where the inlet air valve region was replaced with a new region that contained the new damper position. After the new region was imported, the interfaces were set up and the simulation parameters were verified as consistent with the baseline simulation.

After a new simulation had been created for each of the required damper positions, the simulations were used to estimate the pressure drop for the same range of flows that were observed during the laboratory testing at each damper position.

Figure 8-12 shows the laboratory measured pressure drop across the FPTU for the parallel ECM-M1, ECM-M2, and the WBPBI at damper positions of 0°, 22.5°, 45°, and 67.5°.

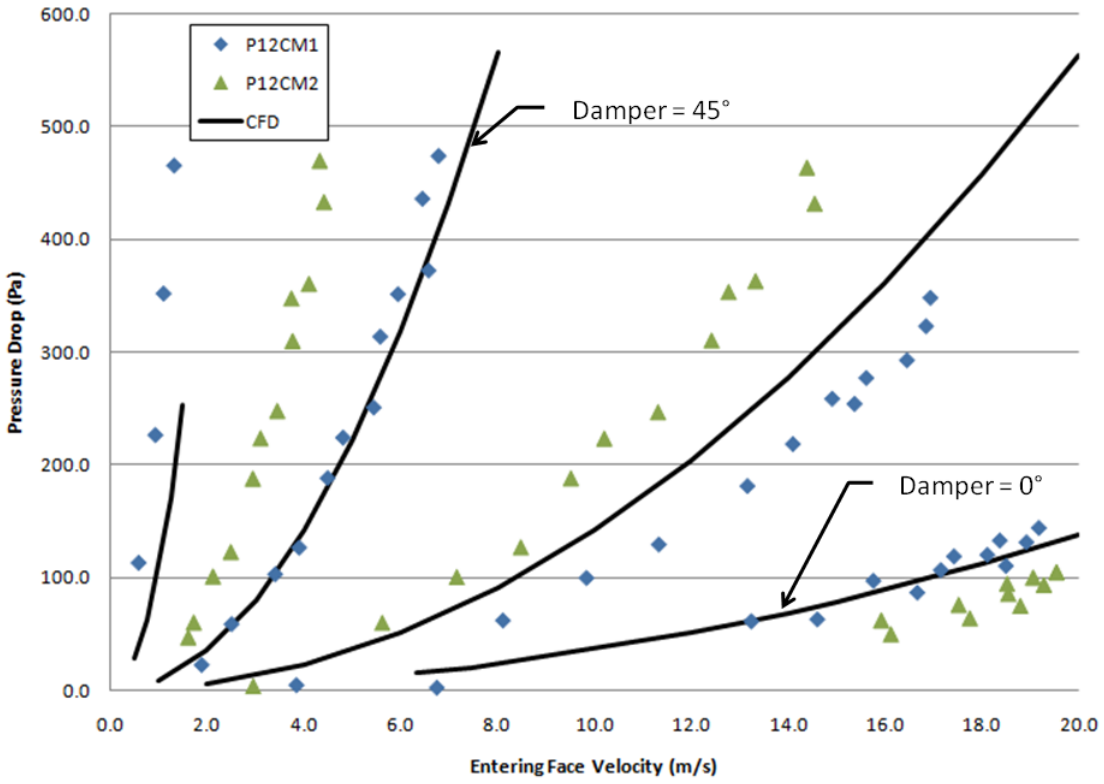

Figure 8-12: Measured pressure drop across P12CM1, P12CM2 and estimated pressure drop from the WUPBI simulation at damper positions of 0°, 22.5°, 45°, and 67.5 °.

Figure 8-12 shows that there was a significant variation in the measured pressure drop for the P12CM1 and P12CM2 FPTUs. According to the manufacturer, the only difference between the two units was the manufacturer of the motor. Since the graph only included the cases where the FPTU fan was not running, then differences in the measured pressure drop cannot be due to differences in the motor.

Figure 8-12 shows that at damper positions of 0°, there was good agreement between the measured pressure drop for P12CM1 and the estimated pressure drop from the WBPBI simulation. The measured pressure drop across P12CM2 was lower than both the measured data for P12CM1 and the simulated pressure drop.

Figure 8-12 shows that at damper position 22.5°, the simulated results were between the measured pressure drop across the P12CM1 and P12CM2 FPTU. For this case, the P12CM1 pressure drop was lower than the P12CM2 pressure drop.

Figure 8-12 shows that at damper position 45°, the simulated data matched the measured data for P12CM1. For this case, the measured pressure drop across P12CM2 was higher than both the measured pressure drop across P12CM1 and the simulated data.

Figure 8-12 shows that at damper position of 67.5°, there was good agreement between the measured pressure drop across the P12CM1 FPTU and the results from the simulation. There was no measured data at 67.5° for the P12CM2 FPTU.

Figure 8-13 shows a graph of the errors between the CFD predicted pressure drop and the measured pressure drop as a function of inlet face velocity for P12C-M1. Figure 8-13 was limited to error values between +/- 20% which excluded all predicted values when compared to the P12C-M2 measured data for all damper positions and the P12C-M1 measured data for damper positions of 22.5° and 67.5°.

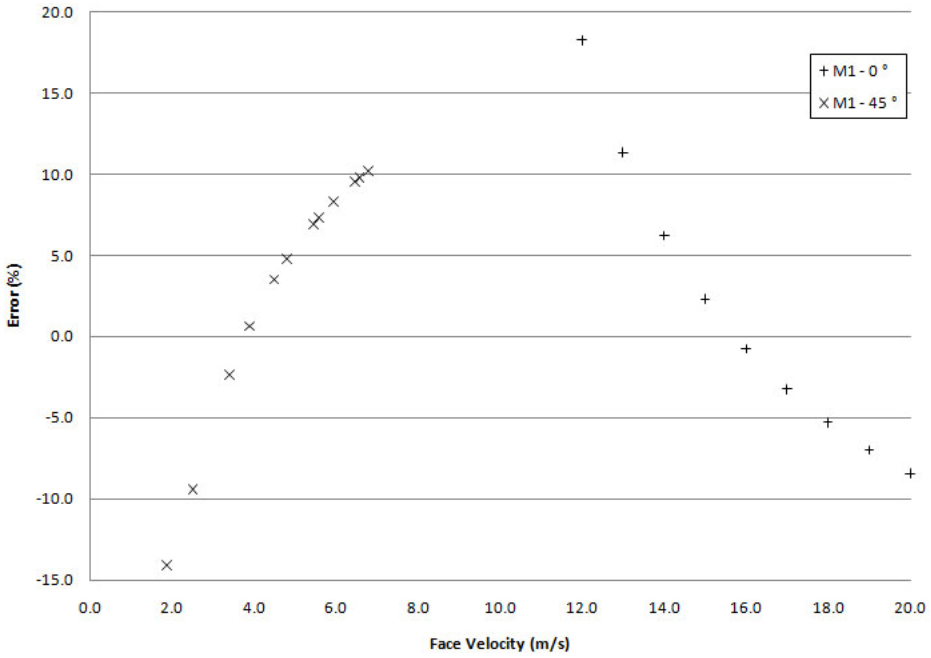

Figure 8-13: A graph of the errors between the CFD predicted pressure drop and the measured pressure drop as a function of inlet face velocity. Only values for P12C-M1 with damper positions of 0° and 45° were within +/- 20%.

When reviewing the differences between the measured data and the CFD predicted data it is important to note that the only difference between P12C-M1 and P12C-M2 was that the ECM motors were from two different manufacturers and that the air flow path for both units was identical excluding normal manufacturing tolerances. Since the CFD model did include the motor, there should have been similar errors between the predicted results and both of the two sets of measured data.

Figure 8-12 shows that there were significant differences between the two sets of measurements for the P12C-M1 and P12C-M2 FPTUs. The differences in the measured values indicated that there were significant measurement errors that were from either problems with the instrumentation or the setup of the test stand. The errors could have

been caused by something as simple as an inaccurate measurement of the damper position. P12C-M1 and P12C-M2 should have been retested until there was good agreement between the measured data for both units.

The errors between the predicted values and the measured values indicate that although for two damper settings there is good agreement between the CFD predicted values and the measured data, more work will be required in order use the CFD model to accurately predict the performance of the terminal unit. The large errors between the predicted values and the measured values for P12C-M2 for all damper positions and flow rates indicates that there were some significant measurement errors and that P12C-M2 should have been retested. There were significant errors between the CFD predictions and the measured values for P12C-M1 for damper positions of 22.5° and 67.5°. Because of the good agreement between the CFD and measured data for damper positions of 0° and 45° the measurements at damper positions of 0° and 22.5° should be redone.

The errors between the CFD predicted values and the measurements indicates that CFD could be used to not only predict the performance of the terminal units but when used interactively with laboratory tests, the quality of the experiment work could be improved. If the experimental work had been done in combination with the CFD analysis, then errors in the CFD model and the laboratory measurements could have been identified at a point where corrections could have been made that would have resulted in improvements to both the CFD model and the experimental results.

CHAPTER IX

SUMMARY AND CONCLUSIONS

Air conditioning systems in large commercial office buildings typically utilize single duct variable air volume (SDVAV) air distribution systems. SDVAV systems vary the primary (conditioned) airflow into the conditioned zones in a building in response to the change in the cooling or heating loads. SDVAV systems provide significant energy savings over conventional constant volume systems. A critical component in SDVAV systems is the Fan Powered Terminal Unit (FPTU.

First generation FPTUs had constant speed fans where the fan motor speed was regulated with a silicon controlled rectifier (SCR) controller. In recent years, manufacturers have begun to make available electronically commutated motors (ECM) in FPTUs. ECM motors also use about one-third of the energy of a similar sized SCR controlled motor and they have the potential to reduce the cooling and fan energy use in commercial buildings. However, they cost more than conventional single speed motors in FPTUs and have the undesirable side-effect of introducing harmonic distortions into the buildings' electrical power grid.

A study sponsored by the California Energy Commission included a comparison of parallel and series terminal units operating in perimeter zones (Kolderup et al. 2003). The study was based on running a simulation with DOE 2.2 (LBNL 1998) and attempted to account for the reduced static pressure of the main supply fan in a series system. The main supply fan static pressure was reduced from 4.0 to 3.67 in. w.g. (996 to 914 Pa) for

the series systems. The findings concluded that, for the case studied, a parallel system would have 9% less energy costs than a series system. The bulk of the energy savings was in the difference in total power consumption of the fans. The explanation given for the energy difference was that since the series fans were in constant operation, and they were less efficient than the larger primary supply fan, a series system had greater energy consumption than a parallel system. However, the study only simulated a single building in California. A building located in a cooler climate could expect larger supplemental heating requirements, in which the parallel terminal unit fans would be required to operate longer hours, and use more energy.

There was no experimental evidence to support the computer simulations by Elleson (1993) and Kolderup et al. (2003) who claimed that parallel VAV systems are more energy efficient than a series system. There was a need to develop a better understanding of systems using parallel and series fan powered VAV terminal units. To model the system properly, it is important to be able to characterize the individual units.

The performance of single speed FPTUs has recently been characterized by Furr et al. (2007). In a follow-on project, the characterization of ECM based FPTU was started by Cramlet (2008) and completed by Edmondson (2009). Leakage is when the primary air flows directly through the FPTU into the return air stream without passing through the conditioned space. Both of the studies by Furr and Edmondson (2009) showed that parallel terminal units can and do leak and that some parallel FPTUs can have primary air leakage rates in excess of 10%. Previous system level studies did not include leakage.

A system level study was done by Davis et al. (2007) that included the effects of leakage in parallel FPTU. The study evaluated the energy consumption of SCR controlled series and parallel FPTU at five weather locations around the United States. The study showed that when leakage rates for parallel FPTU were below 10%, the parallel units used less energy. The problem is that laboratory measurements by Furr et al. (2007) and Edmondson (2009) showed that leakage rates of 10% were possible and that depending on the how the units are installed, maintained, and operated there may be no significant difference between the annual energy consumption of either series or parallel units.

This research project had six main objectives:

1. Develop a system model of a single-duct VAV system using fan-powered terminal units based on the characteristics of currently manufactured FPTUs.
2. Develop a software model that can be used to evaluate the operation of a single-duct VAV system based on either series or parallel terminal units.
3. Use the software model to estimate the total overall energy consumption of series and parallel based systems.
4. Compare the total energy use of series and parallel based systems at five distinct weather locations within the continental United States.
5. Develop a fan-powered terminal unit model that could be offered to the Department of Energy (DOE) as an upgrade to the model that is used in EnergyPlus.
6. Demonstrate that Computational Fluid Dynamics can be used as a design tool that can be used to improve the performance of FPTU.

All of the research objectives were achieved. A system model was developed that used the performance characteristics of ECM and SCR FPTUs that were measured by Furr et al. (2007), Cramlet (2008) and Edmondson (2009). The SDVAV system model developed during this project was based on the calculation procedures that were verified during the ASHRAE RP1292 project (Davis et al 2007). After the system model was developed it was used to model the operation of a generic commercial building at five locations around the United States.

The SDVAV system model was developed using object oriented programming techniques in order to facilitate its use with commercial building simulation programs such as EnergyPlus (U.S. Department of Energy 2008). The full source code for the model was placed in Appendix IV.

The results from the simulation showed:

1. The series SCR FPTU was the worst performing FPTU and used more energy than any other system. It was also shown that the anticipated primary fan savings that resulted from the reduced primary static pressure requirements was offset by the higher required primary air flow rate which resulted in a net increase in the primary fan energy consumption.
2. There was no significant difference in the operation of a SCR parallel FPTU and an ECM parallel FPTU. In other words, paying the premium for an ECM motor for a parallel FPTU was a waste of money.
3. For the ideal case (no leakage), the ECM series FPTU used about 3% more energy than the parallel FPTUs. This is a significant improvement particularly

when the fact that the ECM series unit ran 24 hours a day and the ECM parallel unit only ran about 15% of the year. The increased energy efficiency from the ECM motor reduced the heat load on the system enough that the primary air flow required to handle the motor load was small and a net decrease in primary fan energy was realized.

4. When leakage was considered, the ECM series FPTU outperformed the parallel FPTUs. The decrease in system performance was linear with the leakage rate and at a 10% leakage rate the ECM series outperformed the ECM parallel by 5%.

A computation fluid dynamic model was developed for the primary air flow path of the P12C terminal unit. Initial efforts to model the P12C FPTU as a whole unit simulation were unable to achieve a converged model due to the complexity of the porous baffle that was located inside the unit. After efforts were made to create a finite volume grid with enough resolution to model the baffle failed, it was decided that the porous baffle interface (PBI) built into Star CCM+ would be a reasonable alternative to a more refined grid. After the PBI was introduced the CFD model converged and results at various flow rates and damper settings were obtained. The results from the CFD simulation matched the measured data from the laboratory experiments. The CFD results demonstrated that a combination of CFD modeling and laboratory experiments could be used to build a verified numerical model that could be used to predict the performance of the FPTUs over a broad range of operating conditions and flow rates.

Additional work that needs to be done includes the development of a laboratory verified model of the VAV terminal unit (non-fan powered) and the development of a

laboratory verified model of the ECM series FPTU when operated as a supply air VAV unit with varying downstream static pressure.

REFERENCES

Ardehali, M.M., Smith, T.F. 199V- Evaluation of variable volume and temperature HVAC system for commercial and residential buildings. *Energy Conversion Management* 37(9): 1469-1479.

CD-Adapco. 2009. User Guide Star-CCM+ Version 4.04.011. *CD-Adapco Corporation*.

Cengal, Y. A., Turner, R. H. 2005. Fundamentals of Thermal-Fluid Sciences, 2nd Edition. New York, NY: McGraw-Hill.

Cramlet, A. 2008. Performance of ECM controlled VAV fan powered terminal units. M. S. Thesis, Mechanical Engineering, Texas A&M University - College Station.

Davis, M., Bryant, J., O'Neal, D., Cramlet, A. 2007. ASHRAE Project 1292-RP, Phase II Final Report. Energy Systems Laboratory, Texas A&M University - College Station.

Denn, M. M. 1980. Process Fluid Mechanics. New Jersey: Prentice Hall Inc.

Department of Energy (DOE). 1982. DOE-2 Engineers manual, v 2.1A. U.S. Department of Energy.

Department of Energy (DOE). 2009. EnergyPlus - 4.0 Engineering reference. U.S. Department of Energy.

Edmondson, J. 2009. Modeling of ECM Controlled VAV Fan Powered Terminal Units. M. S. Thesis, Mechanical Engineering, Texas A&M University - College Station.

Elleson, J.S. 1993. Energy use of fan-powered mixing boxes with cold air distribution. *ASHRAE Transactions* 99(1):1349-1358.

Energy Star. 2010. Energy Star Building Manual, Table 9.3: Federal efficiency standards for commercial packaged air-cooled air conditioners and heat pumps. http://www.energystar.gov/ia/business/EPA_BUM_CH9_HVAC.pdf

Fox, R. W., McDonald, A. T., Pritchard, P. J. 2004, Introduction to Fluid Mechanics, 6th Edition. New York: John Wiley & Sons.

Furr, J, O'Neal, D., Davis, M., Bryant, J., Cramlet, A. 2007. ASHRAE Project 1292-RP, Phase I Final Report. Energy Systems Laboratory, Texas A&M University, College Station, TX.

Gosbell, V. J. 2000. Power Quality Centre. Technical Note No.3. University of Wollongong, NSW Australia.

Inoue, U., Matsumoto, T. 1979. A study on energy savings with variable air volume systems by simulation and field measurement. Energy and Buildings 2:27-3V-

Int-Hout, Dan, 2008, A Comparison of Operating Conditions and Associates Costs for Parallel and Series Fan Powered VAV Terminal Units.

Kennedy, Barry W. 2000. Power Quality Primer. New York: McGraw-Hill Professional.

Khoo, I., Levermore, G.J., Letherman, K.M. 1998. Variable-air-volume terminal units I: steady state models. *Building Services Engineering Research & Technology* 19(3):155-162.

Kolderup, E., Hong, T., Hydeman, M., Taylor, S., Stein, J. 2003. Integrated design of large commercial HVAC systems. *Integrated energy systems: productivity and building science.* San Francisco: California Energy Commission.

Kreider, J. F., Curtis, P. S., Rabl, A. R. 2002, Heating and Cooling of Buildings, 2nd Edition. New York: McGraw-Hill.

LBNL. 1998. DOE-2, Version2.2. Lawrence Berkeley National Laboratory. Berkeley, CA.

Schetz, J. A. 1993. Boundary Layer Analysis. New Jersey: Prentice Hall Inc.

Sekhar, S.C. 1997. A critical evaluation of variable air volume system in hot and humid climates. *Energy and Buildings* 26: 223-232.

Shames, I. 1992. Mechanics of Fluids, 3rd Edition. New York: McGraw-Hill Inc.

Shih, T. H., Liou, W. W., Shabbir, A., Yang, Z., Zhu, J. 1994. A New k-Eddy Viscosity Model for High Reynolds Number Turbulent Flow – Model Development and Validation. *NASA TM* 106721.

TRACE® 600: Load Design and Economics Simulation Program. 1993. La Cross, WI: The Trane Company, American Standard Company.

Tu, J., Yeoh, G.H., Liu, C. 2008, Computational Fluid Dynamics: A Practical Approach. New York: Elsevier, Inc.

Wolfstein, M 1969. The Velocity and Temperature Distribution in One-dimensional Flow with Turbulence Augmentation and Pressure Gradient. *Int. J. Heat and Mass Transfer* 12:301-318

APPENDIX I

This appendix documents the coefficients of the equations that relate sensible and latent cooling to the respective flow rates and heat and mass transfer rates.

Sensible Heat Transfer

Equation I-1 was used in various forms throughout the thesis to relate the flow rate of air and the transfer of sensible heat to the change in temperature of the air.

$$Q_{sen} = C_{ps}\dot{Q}_s(T_{hi} - T_{low}) \tag{I-1}$$

where $\dot{Q}_s$ is the flow rate in cubic feet per minute, T_{hi} and T_{low} are the temperatures of the air at the beginning and end of the process and Q_{sen} is the heat transfer associated with the change in temperature. The sensible specific heat, C_{ps}, in the equation is a conversion factor that relates mass flow, specific heat of the moist air, and a change in temperature to a change in enthalpy. Over the range of temperatures that were of interest to this project, the enthalpy of the air can be calculated using a formula from *"Heating and Cooling of Buildings"* by Kreider et al (2002).

$$h = 0.240T_d + \omega(1061.2 - 0.444T_d)\ \frac{Btu}{lb_{da}} \tag{I-2}$$

in which T_d is the dry-bulb temperature in degrees Fahrenheit, ω is the humidity ratio in lb_{water}/lb_{air} and

$$h = 1.0T_d + \omega(2501.3 - 1.86T_d)\ \frac{kJ}{kg_{da}} \tag{I-2B}$$

in which T_d is the dry-bulb temperature in degrees Celsius, ω is the humidity ratio in kg_{water}/kg_{air}. These equations are based on the reference values of enthalpy for saturated water at 0°F and 0°C of $1061.2\,\frac{Btu}{lb_{da}}$ and $2501.3\,\frac{kJ}{kg_{da}}$ respectively. The value of C_{ps} = 1.1 BTUs/hr-F-CFM and C_{pl} = 4840 BTUs-lb_{air}/hr-lb_{water}-CFM was derived by using equation I-1 with dry bulb temperatures and relative humidity's used over the range of conditions simulated during this project. The average specific heats were derived as follows:

For air at leaving cooling coil conditions of 55°F and 95% RH, the air properties are ω = 0.0087 lb/lb, v=13.15 ft^3/lb.

For sensible heating or cooling, using equation I-1

$$h = 0.240T_d + \omega(1061.2 + 0.444T_d) \tag{I-3}$$

For the case of sensible heating or cooling, using constant $\omega = 0.0087$

$$h = 0.240T_d + 0.0087(1061.2 + 0.444T_d) \tag{I-4}$$

$$h = 0.240T_d + 9.23 + 0.0039T_d \tag{I-5}$$

$$h = 0.244T_d + 9.23 \tag{I-6}$$

Performing and energy balance provides and assuming constant density.

$$\dot{Q} = \dot{m}(h_{out} - h_{in}) \tag{I-7}$$

$$\dot{Q} = \dot{m}(h_{out} - h_{in}) = \dot{V}\rho(0.244T_{out} + 9.23 - 0.244T_{in} - 9.23) \tag{I-8}$$

$$\dot{Q} = 0.244\dot{V}\rho(T_{out} - T_{in}) \tag{I-9}$$

At 55°F on an hourly basis (ft^3/min x 60min/hr)

$$\dot{Q} = 0.244\dot{V}\frac{ft^3}{min}\frac{60min/hr}{13.15\frac{ft^3}{lb_{air}}}(T_{out} - T_{in}) \quad \text{(I-10)}$$

$$\dot{Q} = 1.1\dot{V}(T_{out} - T_{in}) \quad \text{(I-11)}$$

For constant temperature humidity change we need the heat of vaporization for water at the estimated dew-point temperature where condensation will occur. The indoor room setpoint conditions for this project were 78 F dry-bulb and 50% RH. The estimated dew-point temperature is 58 F and the heat vaporization for this temperature is1061 Btu/lb_m.

$$\dot{Q} = 1061\dot{m}(\omega_2 - \omega_1) \quad \text{(I-12)}$$

For the case of constant temperature humidity change, using the constant density assumption as before with v=13.15 ft^3/lb

$$\dot{Q} = 1061\dot{m}(\omega_2 - \omega_1) \quad \text{(I-13)}$$

$$\dot{Q} = 1061\dot{V}\frac{ft^3}{min}\frac{60min/hr}{13.15\frac{ft^3}{lb_{air}}}(\omega_2 - \omega_1) \quad \text{(I-14)}$$

$$\dot{Q} = 4840\dot{V}(\omega_2 - \omega_1) \quad \text{(I-15)}$$

APPENDIX II

This appendix documents an alternative procedure for estimating the contribution of the FPTUs to the harmonics at the PCC.

System Level Harmonic Calculations

The calculation of the harmonics at the PCC was done using the definition of the type of harmonic that was modeled. The triplen currents from each zone were simply added to the total for the PCC.

The THD for power is defined by equation II-1.

$$THD_p = \frac{P_2+P_3+P_4 \ldots P_\infty}{P_1} = \frac{P_{total}-P_1}{P_1} \quad \text{(II-1)}$$

At the system level the harmonic powers, P_2 through P_∞ consists of the sum of all of the harmonic power passing through the PCC. When the zone level calculations were done, P_{total} was returned as data from the zone along with P_1. At the system level, the total power from each zone was summed to a system total with a P_1 total for the system. THD_p was then calculated using equation II-1 from the system totals.

The voltage THD at the PCC is a function of the capacity of the system to supply power and the magnitude of the current THD (Mohan et. al.). Calculation of the voltage THD (THD_V) is not straight-forward and some background is required before the calculation method can be presented. Mohan defined the harmonic voltage with equation II-2 where V_n, and I_n, are the voltage and current for the n^{th} order harmonic.

$$V_n = (h\omega L_s)I_n \tag{II-2}$$

L_s is the internal inductance of the system at the PCC and is often specified in terms of the short-circuit current, I_{sc}, using equation II-3 where V_s is the rms value of the per-phase internal voltage of the ac source.

$$I_{sc} = \frac{V_s}{\omega L_s} \tag{II-3}$$

For this analysis, V_s is the same as the fundamental harmonic voltage, V_1. The definition of the THD_v is given by equation II-4.

$$THD_V = \frac{\sqrt{\sum_{n=2}^{\infty} V_n{}^2}}{V_1} \tag{II-4}$$

Solving II-3 for ωL_s and substituting the results into II-12 results in equation II-5.

$$V_n = nV_s \frac{I_n}{I_{sc}} \tag{II-5}$$

Equation II-5 is substituted into equation II-4 to obtain equation II-6 which is an expression for THD_V in terms of the harmonic currents and the RMS phase voltage.

$$THD_V = \frac{\sqrt{\sum_{n=2}^{\infty}(nV_s\frac{I_n}{I_{sc}})^2}}{V_s} = \frac{\sqrt{\sum_{n=2}^{\infty}(nI_n)^2}}{I_{sc}} \tag{II-6}$$

Equation II-7 results from multiplying the right side of equation II-6 by I_1/I_1.

$$THD_V = \frac{I_1}{I_{sc}}\left(\frac{\sqrt{\sum_{n=2}^{25}(nI_n)^2}}{I_1}\right) \quad \text{(II-7)}$$

The quantity in parentheses on the right side of equation II-7 resembles the definition for the current THD, THD_I, and can be used to define a modified current THD, THD_{IM}, as shown in equation II-8.

$$THD_{IM} = \frac{\sqrt{\sum_{n=2}^{\infty}(nI_n)^2}}{I_1} = \sqrt{\sum_{n=2}^{\infty}\left(\frac{nI_n}{I_1}\right)^2} \quad \text{(II-8)}$$

In equation II-8 the fundamental current I_1 represents the summation of the fundamental current for all of the terminal units on the system and I_n is the total of harmonic currents at frequency n from all of the terminal units on the system. Equation II-9 defines I_1 where I_{1k} is the contribution of terminal unit k to the total fundamental current I_1.

$$I_1 = I_{11} + I_{12} + I_{13} + \ \ldots\ I_{1k} = \sum_{k=1}^{\infty} I_{1k} \quad \text{(II-9)}$$

Equation II-10 defines I_n where I_{nk} is the contribution of terminal unit k to the total harmonic current I_n.

$$I_n = I_{n1} + I_{n2} + I_{n3} + \ \ldots\ I_{nk} = \sum_{k=1}^{\infty} I_{nk} \tag{II-10}$$

An average value of the ratio of the harmonic current to the fundamental current for all ECM FPTU tested was obtained for all harmonics from the second through the twenty-fifth. Using the average values of the ratio of the harmonic current to the fundamental current for a single terminal unit we define the harmonic current ratio, A_n, where the harmonic current at a particular frequency is given by equation II-11.

$$I_{nk} = \frac{I_{nk}}{I_{1k}} I_{1k} = A_n I_{1k} \tag{II-11}$$

A_n in equation II-11 did not have a k subscript because using the average value meant that A_n was the same for all FPTU. The total harmonic current at the nth frequency is defined by equation II-12 which resulted from substituting II-11 into II-10.

$$I_n = A_n I_{11} + A_n I_{12} + A_n I_{13} + \ \ldots\ A_n I_{1k} = \sum_{k=1}^{\infty} A_n I_{1k} \tag{II-12}$$

Equation II-13 was an expression for the modified current THD and was obtained by substituting equations II-12 and II-9 into equation II-8.

$$THD_{IM} = \sqrt{\sum_{n=2}^{\infty} \left(\frac{n\left(\sum_{k=1}^{\infty} A_n I_{1k}\right)}{\sum_{k=1}^{\infty} I_{1k}}\right)^2} = \sqrt{\sum_{n=2}^{\infty} \left(\frac{nA_n \sum_{k=1}^{\infty} I_{1k}}{\sum_{k=1}^{\infty} I_{1k}}\right)^2} \tag{II-13}$$

Equation II-13 was simplified to yield equation II-14.

$$THD_{IM} = \sqrt{\sum_{n=2}^{\infty}(nA_n)^2} = 14.74 \quad \text{(II-14)}$$

The value of THD_{IM} was calculated from experimental data. In equation II-12 the short circuit current, I_{sc}, is specific to the PCC and for the simulations it was a user defined input. The fundamental current, I_1, in equation II-7 is the total current at the fundamental frequency and was a summation of the I_1 currents from the zone calculations. Equation II-15 resulted from combining equation II-7 with equation II-14.

$$THD_V = \frac{I_1}{I_{sc}} THD_{IM} = 14.74 \frac{I_1}{I_{sc}} = 15 \frac{I_1}{I_{sc}} \quad \text{(II-15)}$$

APPENDIX III

This appendix includes tables of output from the system simulations

Table III-1: Ideal case in Houston.

	SCR_S12A	ECM_S12A	SCR_P12A	ECM_P12A
Total Plant Energy (MMBtus)	592	551	533	532
Total Cooling Plant (MMBtus)	207	197	193	193
Primary Fan Energy (MMBtus)	12.8	10.8	11.1	11.5
Terminal Unit Fan Energy (MMBtus)	111	39	32	11
Heat Added (MMBtus)	262	304	297	317
Fan + Heat (MMBtus)	373	343	329	328
Max Static (in)	0.117	0.072	0.261	0.368
Min Static (in)	0.000	0.000	0.026	0.036

Table III-2: Series ECM in Houston for three manufacturers.

	Series ECM		
	S12A	S12B	S12C
Total Energy (MMBtus)	551	563	556
Total Cooling (MMBtus)	197	200	198
Primary Fan Energy (MMBtus)	10.8	11.2	11.1
Terminal Unit Fan Energy (MMBtus)	39.0	61.0	50.0
Heat Added (MMBtus)	304	291	297
Fan + Heat (MMBtus)	343	352	347
Max Static (in)	0.072	0.053	0.075
Min Static (in)	0.000	0.000	0.000

Table III-3: Parallel ECM in Houston for three manufacturers.

	Parallel ECM		
	P12A	**P12B**	**P12C**
Total Energy (MMBtus)	532	532	532
Total Cooling (MMBtus)	193	192	193
Primary Fan Energy (MMBtus)	11.5	11.2	11.7
Terminal Unit Fan Energy (MMBtus)	11.0	14.0	11.0
Heat Added (MMBtus)	317	314	317
Fan + Heat (MMBtus)	328	328	328
Max Static (in)	0.368	0.273	0.414
Min Static (in)	0.036	0.027	0.041

Table III-4: SCR_P12A in Houston with leakage.

	SCR_P12A			
	Base	**5%**	**10%**	**20%**
Total Plant Energy (MMBtus)	533	548	563	595
Total Cooling Plant (MMBtus)	193	197	201	210
Primary Fan Energy (MMBtus)	11.1	12.5	13.9	17.2
Terminal Unit Fan Energy (MMBtus)	32.0	32.0	32.0	32.0
Heat Added (MMBtus)	297	307	316	336
Fan + Heat (MMBtus)	329	338	348	368
Max Static (in)	0.261	0.265	0.270	0.279
Min Static (in)	0.026	0.026	0.026	0.027

Table III-5: ECM_P12A in Houston with leakage.

	ECM_P12A			
	Base	**5%**	**10%**	**20%**
Total Plant Energy (MMBtus)	532	548	564	596
Total Cooling Plant (MMBtus)	193	197	201	210
Primary Fan Energy (MMBtus)	11.5	13.0	14.5	18.0
Terminal Unit Fan Energy (MMBtus)	11.0	11.0	11.0	11.0
Heat Added (MMBtus)	317	327	337	357
Fan + Heat (MMBtus)	328	338	348	367
Max Static (in)	0.368	0.384	0.399	0.433
Min Static (in)	0.036	0.038	0.039	0.042

Table III-6: Ideal case in Phoenix.

	SCR_S12A	ECM_S12A	SCR_P12A	ECM_P12A
Total Plant Energy (MMBtus)	545	499	478	477
Total Cooling Plant(MMBtus)	222	210	205	205
Primary Fan Energy (MMBtus)	12.4	10.5	10.8	11.2
Terminal Unit Fan Energy (MMBtus)	111.0	39.0	30.0	10.0
Heat Added (MMBtus)	200	239	232	251
Fan + Heat (MMBtus)	311	277	262	261
Max Static (in)	0.117	0.072	0.261	0.368
Min Static (in)	0.000	0.000	0.026	0.036

Table III-7: SCR_P12A in Phoenix with leakage.

	SCR_P12A			
	Base	5%	10%	20%
Total Plant Energy (MMBtus)	478	493	509	539
Total Cooling Plant(MMBtus)	205	210	215	224
Primary Fan Energy (MMBtus)	10.8	12.1	14.1	17.4
Terminal Unit Fan Energy (MMBtus)	30.0	30.0	27.0	27.0
Heat Added (MMBtus)	232	241	253	271
Fan + Heat (MMBtus)	262	271	280	299
Max Static (in)	0.261	0.265	0.399	0.433
Min Static (in)	0.026	0.026	0.028	0.029

Table III-8: ECM_P12A in Phoenix with leakage.

	ECM_P12A			
	Base	5%	10%	20%
Total Plant Energy (MMBtus)	477	493	508	539
Total Cooling Plant(MMBtus)	205	210	214	224
Primary Fan Energy (MMBtus)	11.2	12.5	14.0	17.4
Terminal Unit Fan Energy (MMBtus)	10.0	10.0	10.0	10.0
Heat Added (MMBtus)	251	261	270	288
Fan + Heat (MMBtus)	261	271	280	298
Max Static (in)	0.368	0.384	0.399	0.433
Min Static (in)	0.036	0.038	0.039	0.042

Table III-9: Ideal case in Chicago.

	SCR_S12A	ECM_S12A	SCR_P12A	ECM_P12A
Total Plant Energy (MMBtus)	563	530	518	517
Total Cooling Plant(MMBtus)	158	152	149	149
Primary Fan Energy (MMBtus)	9.6	8.2	8.7	9.0
Terminal Unit Fan Energy (MMBtus)	111	38	36	12
Heat Added (MMBtus)	284	332	324	347
Fan + Heat (MMBtus)	395	371	360	359
Max Static (in)	0.117	0.072	0.261	0.368
Min Static (in)	0.000	0.000	0.026	0.036

Table III-10: SCR_P12A in Chicago with leakage.

	SCR_P12A			
	Base	5%	10%	20%
Total Plant Energy (MMBtus)	518	539	547	577
Total Cooling Plant(MMBtus)	149	153	154	160
Primary Fan Energy (MMBtus)	8.7	14.5	10.7	13.8
Terminal Unit Fan Energy (MMBtus)	36	32	36	33
Heat Added (MMBtus)	324	339	346	370
Fan + Heat (MMBtus)	360	371	382	403
Max Static (in)	0.261	1.494	0.270	0.433
Min Static (in)	0.026	0.075	0.026	0.040

Table III-11: ECM_P12A in Chicago with leakage.

	ECM_P12A			
	Base	5%	10%	20%
Total Plant Energy (MMBtus)	517	537	547	577
Total Cooling Plant(MMBtus)	149	153	154	160
Primary Fan Energy (MMBtus)	9.0	14.2	11.2	13.8
Terminal Unit Fan Energy (MMBtus)	12	11	12	12
Heat Added (MMBtus)	347	359	369	391
Fan + Heat (MMBtus)	359	370	381	403
Max Static (in)	0.368	1.494	0.399	0.433
Min Static (in)	0.036	0.075	0.039	0.042

Table III-12: Ideal case in New York.

	SCR_S12A	ECM_S12A	SCR_P12A	ECM_P12A
Total Plant Energy (MMBtus)	537	502	488	487
Total Cooling Plant (MMBtus)	166	159	156	156
Primary Fan Energy (MMBtus)	9.9	8.5	8.9	9.2
Terminal Unit Fan Energy (MMBtus)	111	38	35	12
Heat Added (MMBtus)	250	296	288	310
Fan + Heat (MMBtus)	361	335	322	322
Max Static (in)	0.117	0.072	0.261	0.368
Min Static (in)	0.000	0.000	0.026	0.036

Table III-13: SCR_P12A in New York with leakage.

	SCR_P12A			
	Base	5%	10%	20%
Total Plant Energy (MMBtus)	488	503	517	546
Total Cooling Plant (MMBtus)	156	159	162	168
Primary Fan Energy (MMBtus)	8.9	9.9	11.0	13.5
Terminal Unit Fan Energy (MMBtus)	35	35	35	35
Heat Added (MMBtus)	288	299	309	330
Fan + Heat (MMBtus)	322	333	344	365
Max Static (in)	0.261	0.265	0.270	0.279
Min Static (in)	0.026	0.026	0.026	0.027

Table III-14: ECM_P12A in New York with leakage.

	ECM_P12A			
	Base	5%	10%	20%
Total Plant Energy (MMBtus)	487	502	518	547
Total Cooling Plant (MMBtus)	156	159	162	168
Primary Fan Energy (MMBtus)	9.2	10.3	11.5	14.1
Terminal Unit Fan Energy (MMBtus)	12	12	12	12
Heat Added (MMBtus)	310	321	332	353
Fan + Heat (MMBtus)	322	333	343	364
Max Static (in)	0.368	0.384	0.399	0.433
Min Static (in)	0.036	0.038	0.039	0.042

Table III-15: Ideal case San Francisco.

	SCR_S12A	ECM_S12A	SCR_P12A	ECM_P12A
Total Plant Energy (MMBtus)	504	470	458	457
Total Cooling Plant(MMBtus)	163	156	153	153
Primary Fan Energy (MMBtus)	8.9	7.5	8.5	8.3
Terminal Unit Fan Energy (MMBtus)	111.0	38.0	19.0	12.0
Heat Added (MMBtus)	222	269	277	284
Fan + Heat (MMBtus)	333	308	296	296
Max Static (in)	0.117	0.072	0.368	0.368
Min Static (in)	0.000	0.000	0.055	0.055

Table III-16: SCR_P12A in San Francisco with leakage.

	SCR_P12A			
	Base	5%	10%	20%
Total Plant Energy (MMBtus)	458	472	487	516
Total Cooling Plant(MMBtus)	153	156	159	165
Primary Fan Energy (MMBtus)	8.5	8.9	9.8	11.9
Terminal Unit Fan Energy (MMBtus)	19.0	35.0	35.0	35.0
Heat Added (MMBtus)	277	272	283	304
Fan + Heat (MMBtus)	296	307	318	339
Max Static (in)	0.368	0.265	0.270	0.279
Min Static (in)	0.055	0.040	0.040	0.042

Table III-17: ECM_P12A in San Francisco with leakage.

	ECM_P12A			
	Base	5%	10%	20%
Total Plant Energy (MMBtus)	457	472	487	517
Total Cooling Plant(MMBtus)	153	156	159	165
Primary Fan Energy (MMBtus)	8.3	9.2	10.3	12.5
Terminal Unit Fan Energy (MMBtus)	12.0	12.0	12.0	12.0
Heat Added (MMBtus)	284	295	306	327
Fan + Heat (MMBtus)	296	307	318	339
Max Static (in)	0.368	0.384	0.399	0.433
Min Static (in)	0.055	0.057	0.060	0.065

APPENDIX IV

This appendix contains a listing of the source code for the SDVAV system model. The full source code is attached as a zip file that contains the entire project file and directory required to compile and run the model code.

APPENDIX V

This appendix contains Chapter 6 from ASHRAE RP1292 Phase II report (Davis et al 2007) which describes the verification of the system model. The chapter appears here with modification of the figure, table, and equation numbers.

CHAPTER 6

The Three Zone Test Stand and Model Verification

INTRODUCTION

A three zone system was constructed at the Energy Systems Laboratory's Riverside testing Facility. The test stand was designed and constructed to support an air distribution system consisting of three VAV zones. The model, as described in Chapter 5, had been used to develop the testing points for use in the experimental test stand.

EXPERIMENTAL SETUP

A diagram of the system is show in Figure V-1. The diagram shows that the test stand was built with a primary air plenum supplying air to three separately controllable duct systems which served as the three zones.

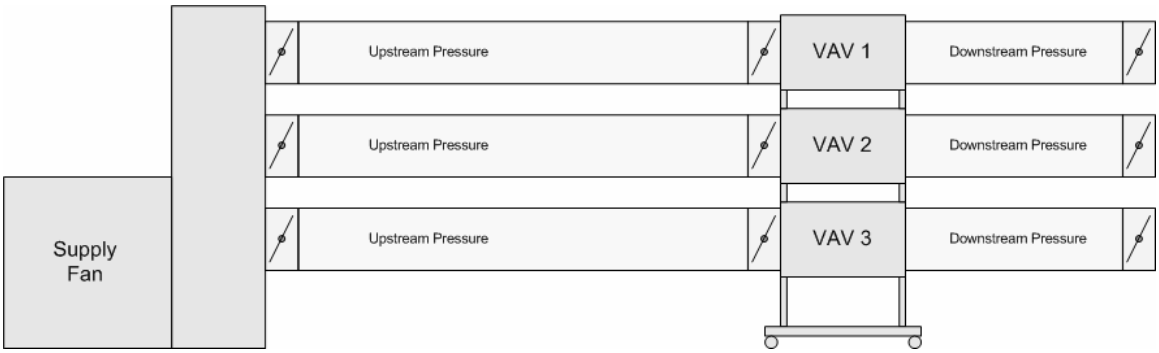

Figure V-1. Diagram of the Three Zone Test Stand.

The plenum that supplied primary air to the three zones was constructed from sheet metal and was connected to the primary air plenum of an 80-ton (281 kW) packaged rooftop air conditioner. The main fan for the packaged rooftop unit served as the primary air fan for the test stand.

Each of the three zones were connected to the primary air plenum with round, sheet metal ducts. A butterfly damper was located in the orifice at the connection point between the primary air plenum and the zone primary air duct. The butterfly damper was used to control the upstream static pressure supplied to each zone.

The VAV terminal unit of each zone was connected to the primary air plenum and to the supply air plenum. The primary air inlet port of the VAV terminal units had an integrated VAV damper to control the amount of primary allowed into the VAV unit. Each VAV terminal unit was connected to the supply register by way of a rectangular duct connected to the terminal unit at the supply port. Return air was pulled into the VAV terminal units at an open return air port that was located at the inlet side of the terminal unit fan.

The supply duct consisted of a rectangular sheet metal duct that connected to a supply register which had an integrated opposed blade damper. The opposed blade damper at the supply register was used to control the downstream static pressure.

CONTROLS

Figure V-2 shows the VAV test stand control points. The upstream static pressure was controlled by an actuator that opened and closed the butterfly damper leading into the primary air duct from the primary air plenum. The downstream static pressure was controlled by an actuator that opened and closed the opposed blade damper at the supply register.

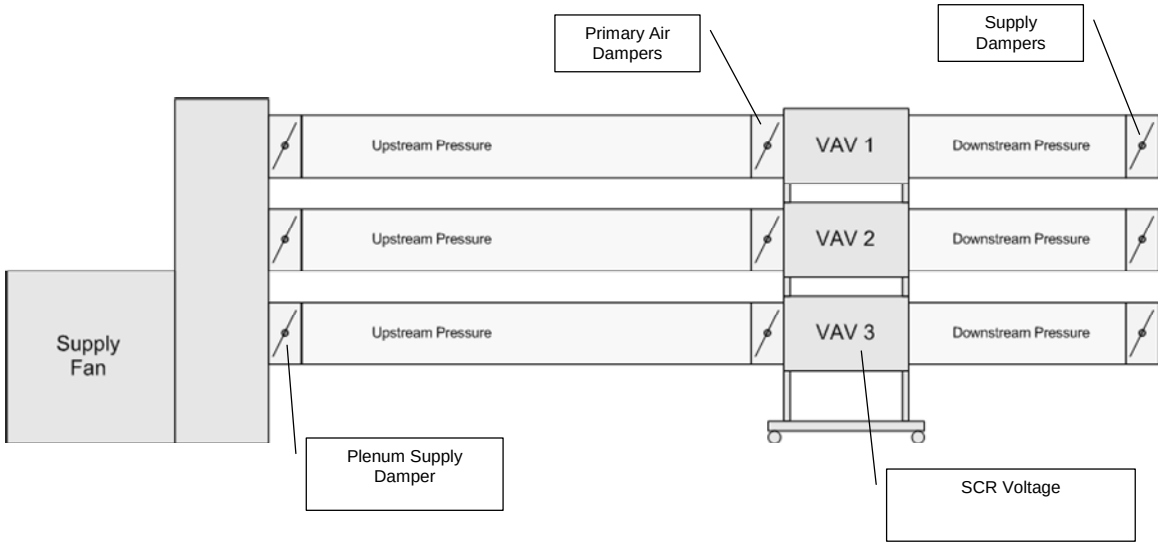

Figure V-2. VAV Test Stand Control Points.

The amount of primary air that passed through the VAV terminal unit was controlled by an actuator that opened and closed the damper that was located in the primary inlet port of the VAV terminal units.

The speed of the terminal unit fans was controlled by adjusting an SCR controller which varied the rotational speed of the motor directly in proportion to the adjustment of the output voltage setting of the SCR controller. The SCR controller was adjusted by an actuator that was attached to voltage controller of the SCR controller.

The entire setup was controlled by an off-the-shelf control system of a type typically used in building control applications. The operator of the test stand adjusted the actuator settings of each of the zones by issuing commands directly through the control system console. When a test was conducted, the actuators at each position in the test stand were set to control values that were pre-determined by the three zone model. The operation of the test stand will be discussed in detail later in this chapter.

INSTRUMENTATION

Figure V-3 shows a diagram of the locations of the sensors that were used to monitor the test stand. The data acquisition equipment consisted of a 16-bit multi-channel PC-based system. The measurements taken for each zone consisted of upstream static pressure, downstream static pressure, the flow sensor pressure, VAV terminal unit fan power, primary air plenum temperature, return air temperature, and supply temperature. Manual measurements were used to verify that the control signal commands to the primary air flow damper were as issued by the control system. Manual measurements

were also taken to verify that the SCR output voltage to the terminal unit fan was the expected value based on the control command.

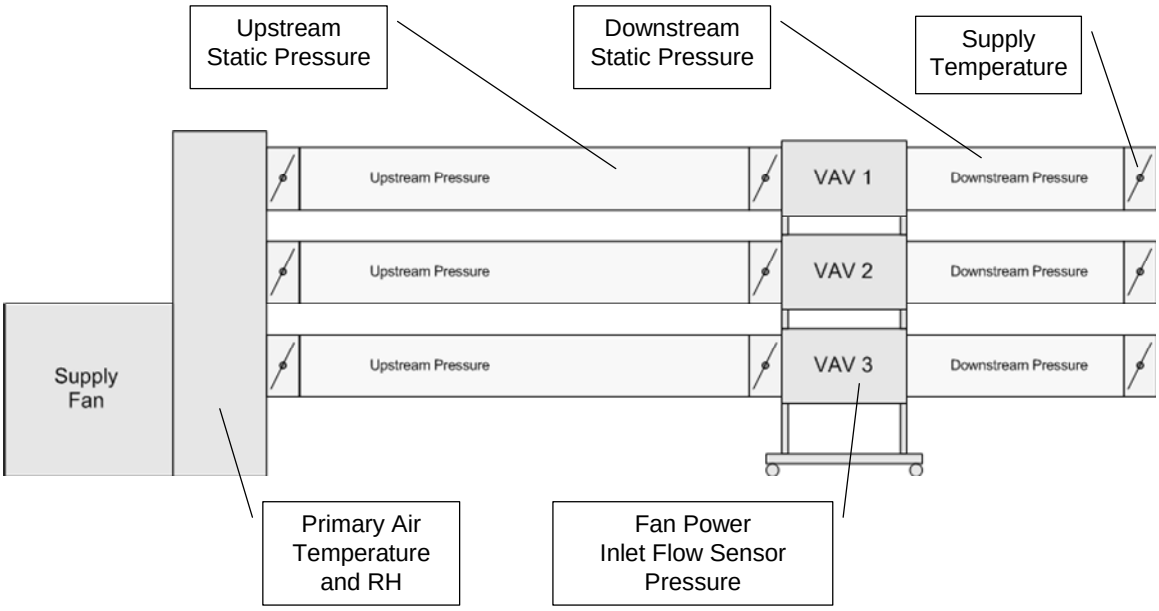

Figure V-3. VAV Test Stand Instrumentation Points.

The sensors used for upstream static pressure, downstream static pressure, and differential pressure measurements had a range of 0 – 2 in.wg. (0 – 0.498 kPa) of differential static pressure and were 0.3% accurate for the range of the sensor.

All sensors used in this project provided outputs in the form of 4-20 milliamp current signals that were linear across the full range of the sensor. The output current signal from each sensor was terminated through a separate 200 Ohm, 1 percent instrumentation quality resistor located on a separate input channel on the data acquisition system. The voltage generated at the input channel through the terminating resistor was converted to

a 16-bit digital value by the data acquisition hardware. The digital value was scaled in software according to the type of signal being measured.

The data acquisition was through a PC-based system using a Pentium computer running Windows 2000 Server as the operating system. Figure V-4 shows a diagram of how the data acquisition process worked. The data was gathered by the computer based data acquisition system and was then sent through the laboratory's network to another computer that stored the data into an SQL database.

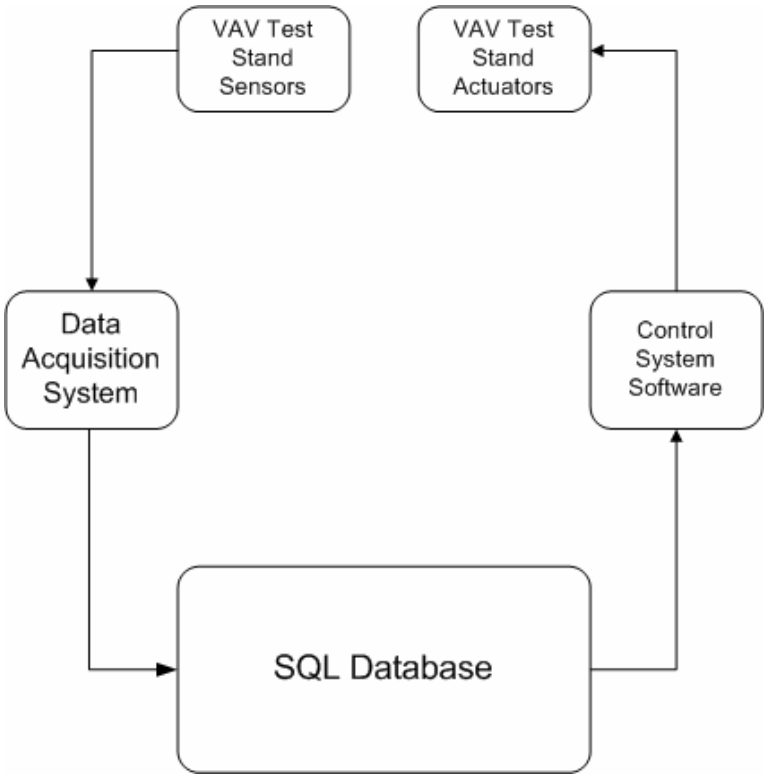

Figure V-4. Diagram of Data Flow During a Test.

The data acquisition system operated continuously and gathered data from the sensors at a rate of 1000 samples per second. The samples were integrated, averaged, and stored each minute. Each set of data was stored with a time stamp that included month, day, year, hour and minute.

Figure V-5 is a photograph of the test stand after it was built. The same test stand was used for both series and parallel fan powered terminal units. The data from those tests were used to verify both the three zone series model and the three zone parallel model. The verification process is described later in this chapter.

Figure V-5. Photograph of the Completed Test Stand.

TEST MATRIX DEVELOPMENT

A test matrix was developed that identified critical test conditions at peak cooling and heating loads as well as moderate operating conditions expected in the spring and summer. The test matrix was developed to supply operational points for the experimental three zone system. The normalized hourly profiles were used to develop a test plan for the various terminal unit sizes used in the Phase I of the project.

The normalized zone loads were used in the development of the test plan to determine which hours out of the year were to be used to verify the model. The hours were selected by adding the normalized hourly sensible values together to create an hourly total sensible load profile which resulted in an hourly value between 0 and 3. The hourly values were then graphed on a monthly basis and the monthly graphs were inspected for the annual maximum daily loads, the annual minimum daily loads, and two intermediate daily profiles. The monthly load profiles are shown in Figures V-6 – V-17. The four daily profiles selected were January 4, April 5, July 6, and September 28.

The four daily profiles that were selected were graphed and the graph was inspected to determine the daily periods that were most likely to result in the operation of the VAV terminal units over their full range. Figure V-18 shows the graph of the four selected daily profiles. Figure V-19 shows the graph of the daily profile of each zone for September 28. The coincident maximum cooling load for all zones for the facility is on this date. Figure V-20 shows the hourly loads of the three zones for April 5, which is a day during the mild cooling season.

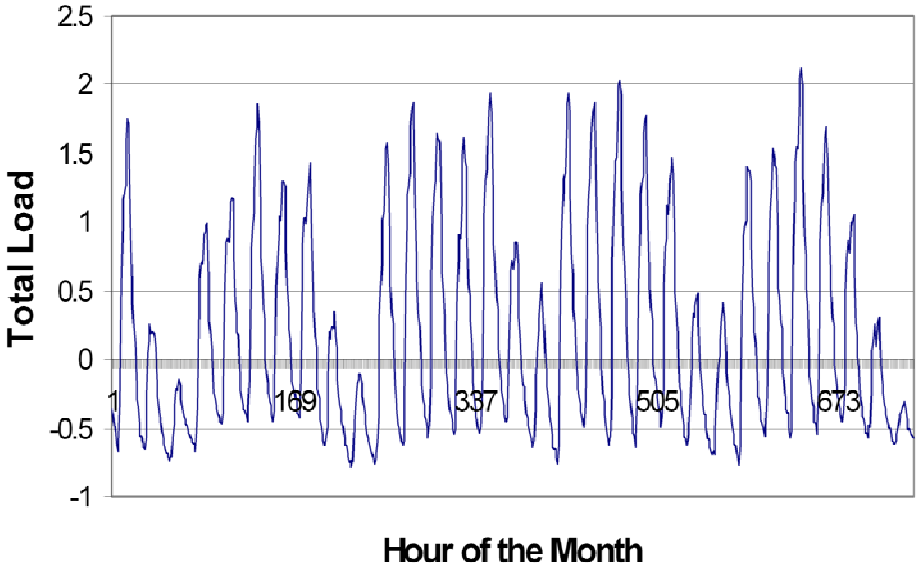

Figure V-6. Normalized Hourly Loads for the Month of January.

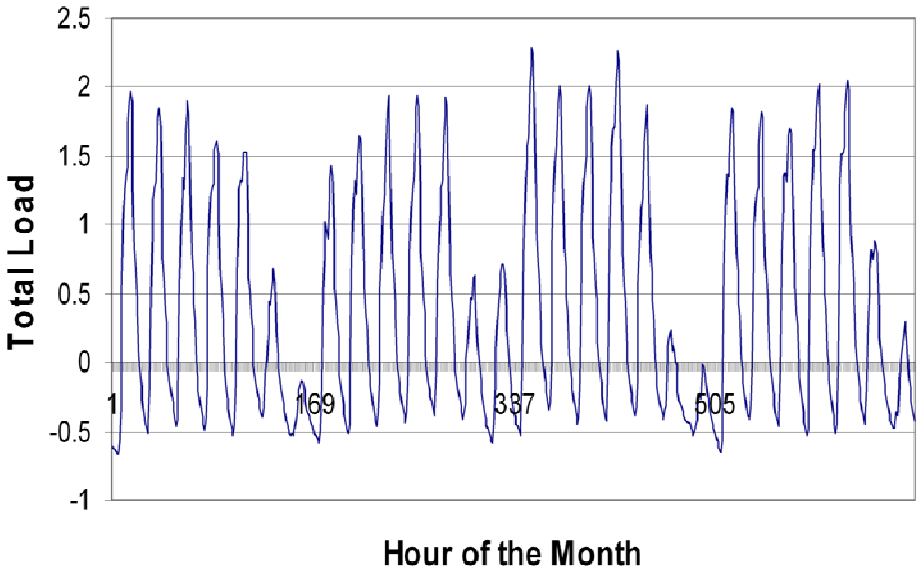

Figure V-7. Normalized Hourly loads for the Month of February.

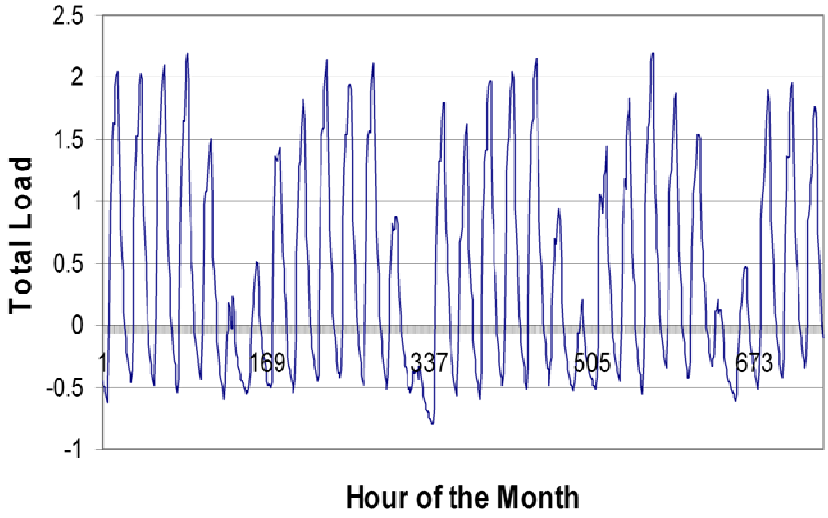

Figure V-8. Normalized Hourly loads for the Month of March.

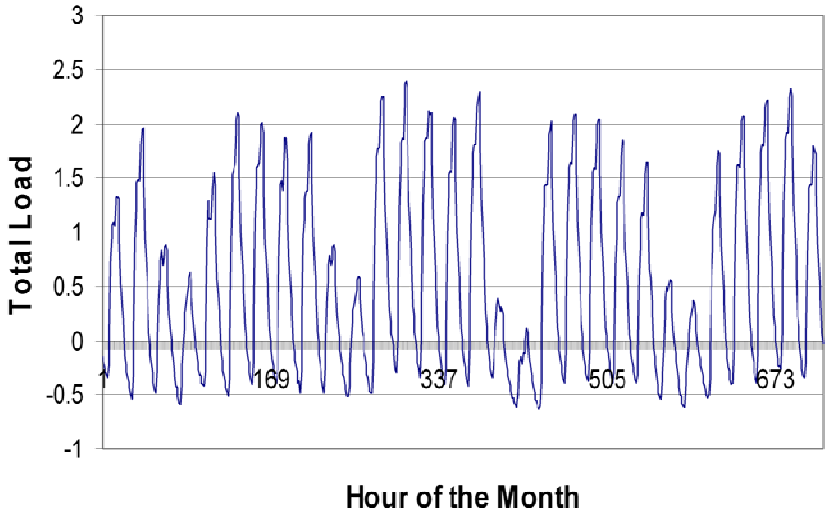

Figure V-9. Normalized Hourly Loads for the Month of April.

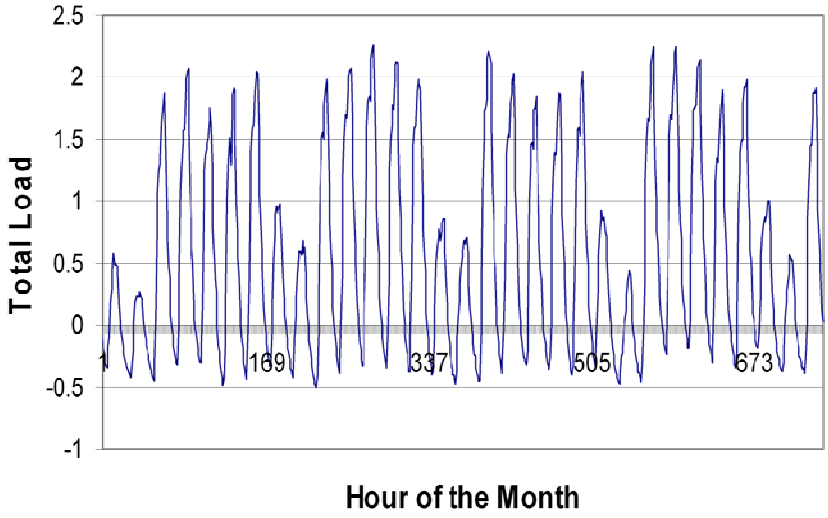

Figure V-10. Normalized Hourly Loads for the Month of May.

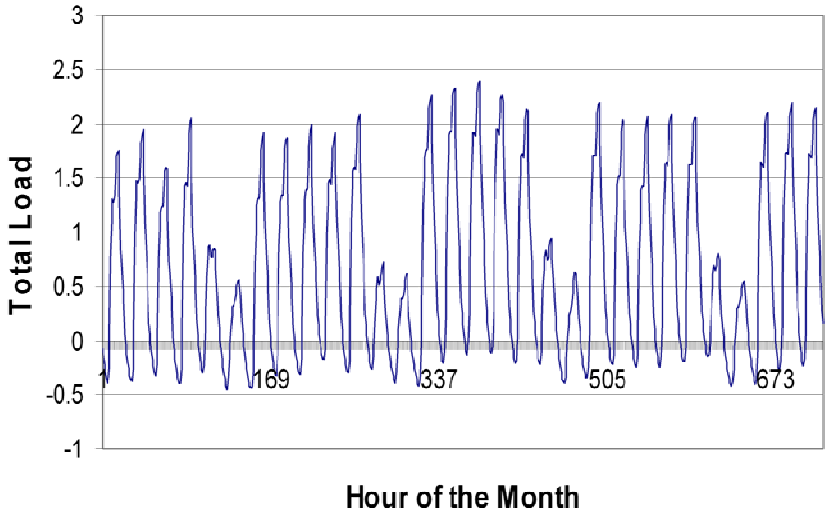

Figure V-11. Normalized Hourly Loads for the Month of June.

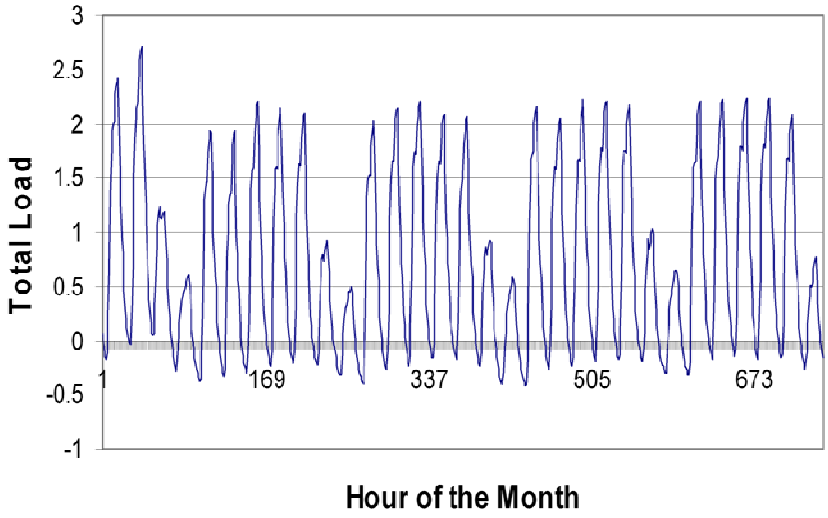

Figure V-12. Normalized Hourly Loads for the Month of July.

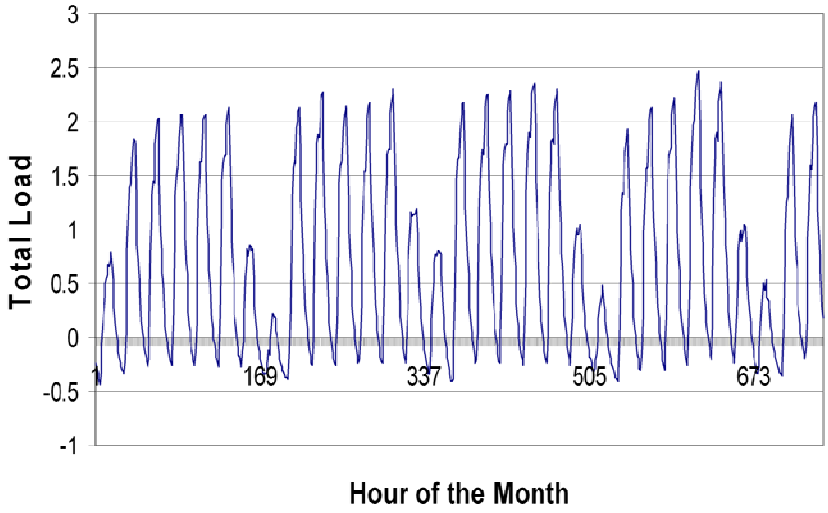

Figure V-13. Normalized Hourly Loads for the Month of August.

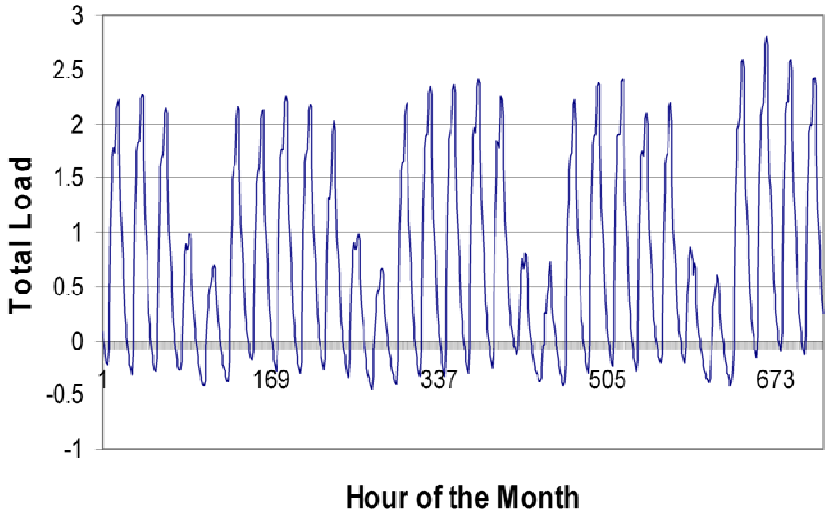

Figure V-14- Normalized Hourly Loads for the Month of September.

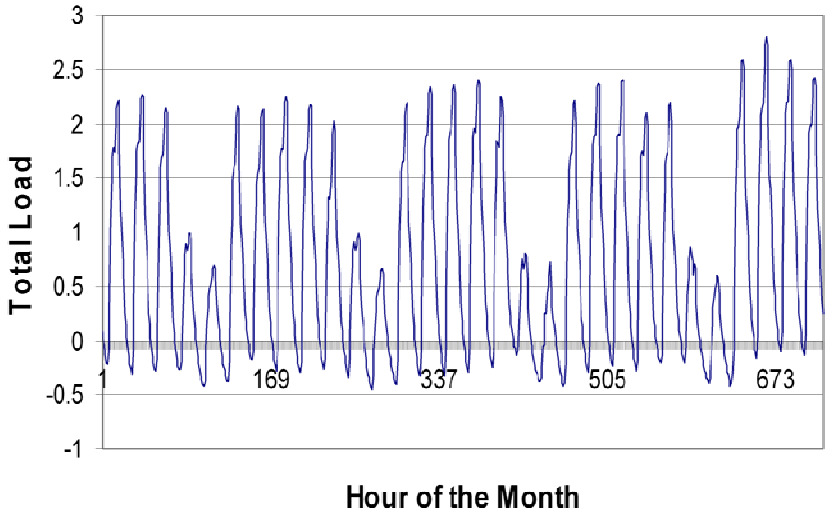

Figure V-15. Normalized Hourly Loads for the Month of October.

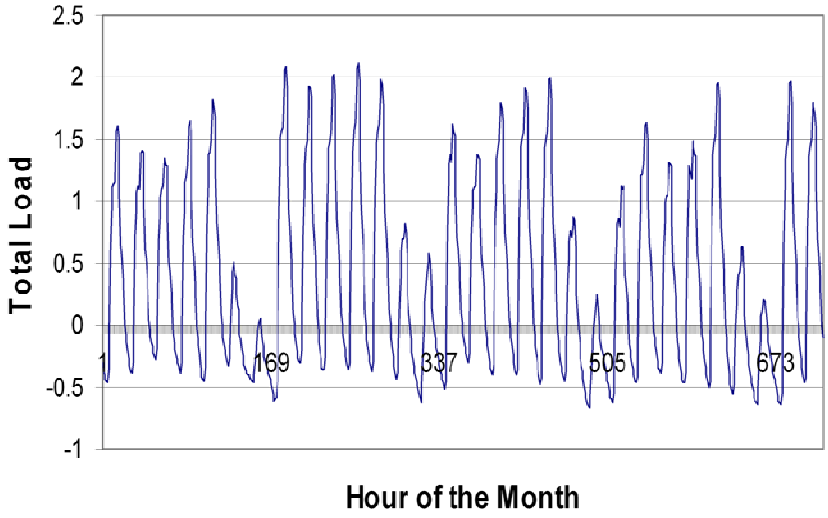

Figure V-16. Normalized Hourly Loads for the Month of November.

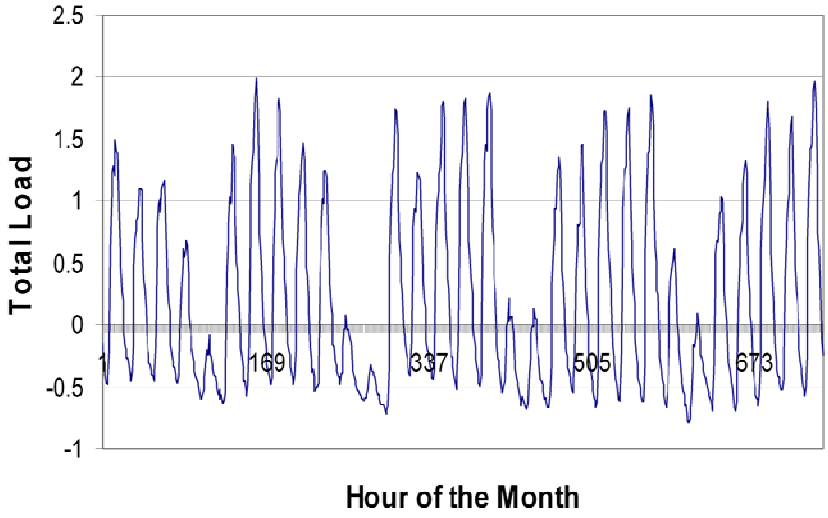

Figure V-17. Normalized Hourly Loads for the Month of December.

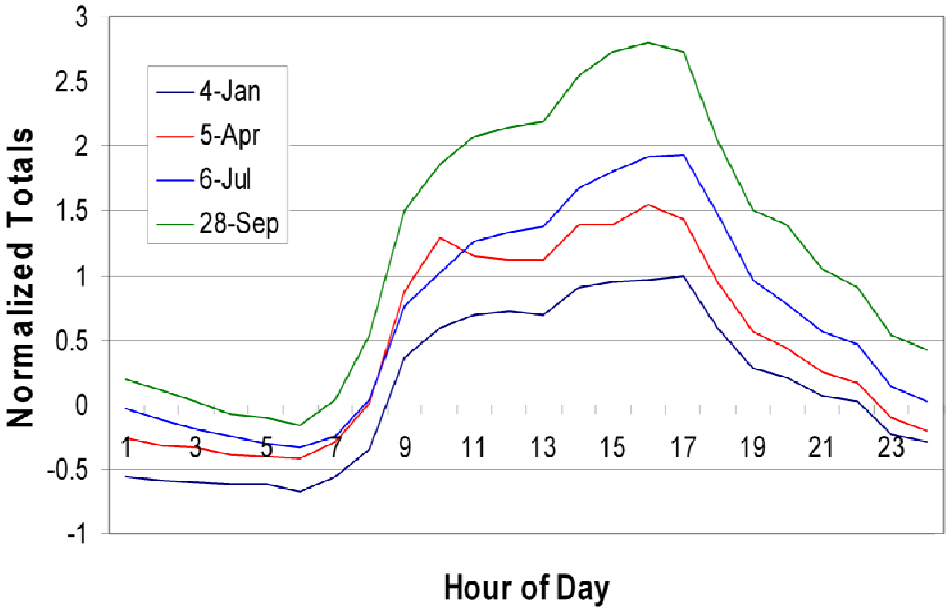

Figure V-18. Normalized Hourly Loads for the Four Daily Profiles Selected from Annual Loads.

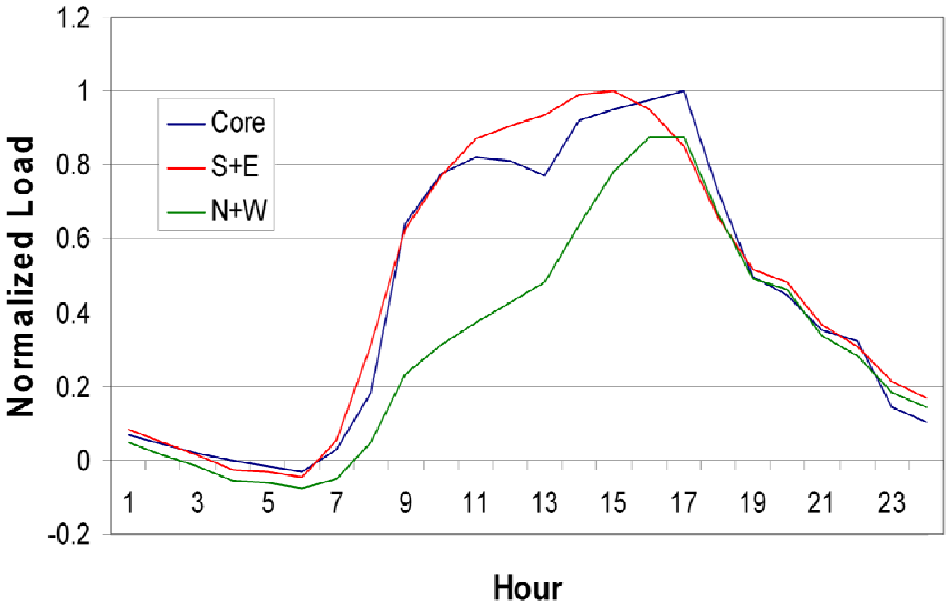

Figure V-19. Hourly Loads for Three Zones on September 28, Coincident with Peak Cooling for the Facility.

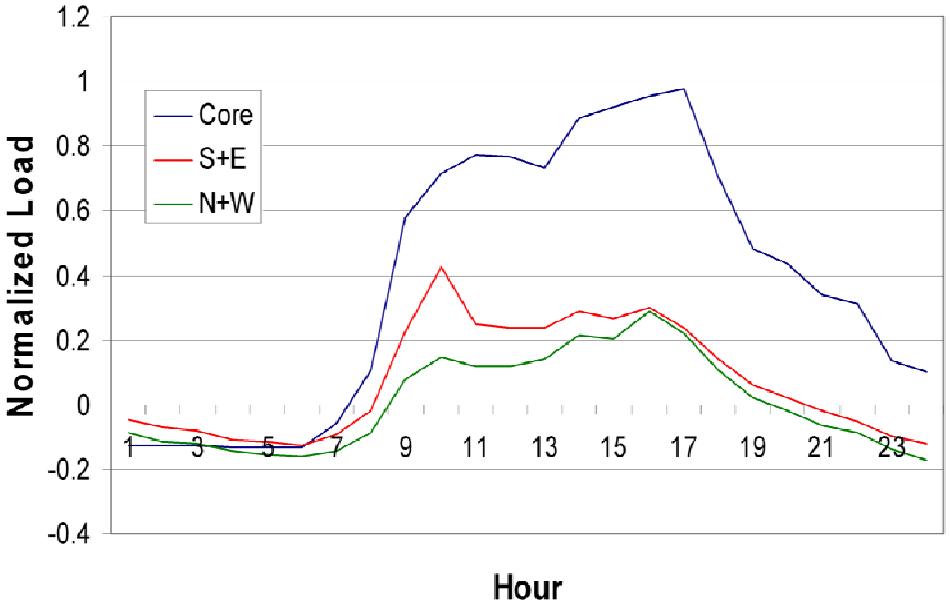

Figure V-20. Normalized Hourly Loads for Three Zones for April 5, Representative of Moderate Load Conditions.

MODEL VERIFICATION TEST POINTS

The time periods used for the model verification points were selected and the total normalized loads for these time periods are shown in Table V-1. In addition to selecting the load profiles used for the model verification, the time periods were also used to select the VAV terminal unit size rotation that was used as the second step in the model verification process. The terminal unit size rotation schedule is shown in Table V-2. The hourly load profiles and terminal size rotation schedules shown in Table V-1 and Table V-2 were used for both series and parallel terminal units.

Table V-1. Hourly Periods Selected as Basis for Model Verification Points.

Hour	4-Jan	5-Apr	6-Jul	28-Sep
8	-0.35	0.01	0.03	0.54
9	0.36	0.88	0.76	1.50
10	0.59	1.29	1.02	1.86
15	0.94	1.40	1.81	2.73
16	0.97	1.54	1.92	2.80
17	0.99	1.43	1.93	2.73

Table V-2. Terminal Unit Size Rotation Schedule for the Model Verification Test Points.

	4-Jan			5-Apr			6-Jul			28-Sep		
Hour	Core	N+E	S+W	Core	N+E	S+W	Core	N+E	S+W	Core	N+E	S+W
8	8	8	8	12	8	8	12	12	8	12	12	12
9	8	8	8	12	8	8	12	12	8	12	12	12
10	8	8	8	12	8	8	12	12	8	12	12	12
15	8	8	8	12	8	8	12	12	8	12	12	12
16	8	8	8	12	8	8	12	12	8	12	12	12
17	8	8	8	12	8	8	12	12	8	12	12	12

SERIES TEST MATRIX

After the operating points were selected, the settings to be used for the test stand were determined for the series terminal units. The zone terminal units were setup based on the peak cooling capacity of the terminal unit and the peak cooling load of the zone. Using the normalized loads that were scaled to the capacity of the terminal unit, the test stand settings were determined using the three zone series terminal unit model to determine the operating settings of the test stand zones. Tables V-3 through V-6 show the predicted test stand control system and duct settings for each hour selected as a test point.

Table V-3. Terminal Unit Test Stand Settings for January 4th Operating Profile.

Test Point Settings Jan 4												
	Zone 1 - S8C				Zone 2 - S8C				Zone 3 - S8C			
Hour	Primary Static (in)	Primary Air Damper (V)	SCR Voltage (V)	Downstream Static (in)	Primary Static (in)	Primary Air Damper (V)	SCR Voltage (V)	Downstream Static (in)	Primary Static (in)	Primary Air Damper (V)	SCR Voltage (V)	Downstream Static (in)
8	0.10	2.695	277	0.25	0.10	6.9	224	0.25	0.10	6.5	171	0.25
9	0.10	0.352	277	0.25	0.10	6.9	224	0.25	0.10	6.5	171	0.25
10	0.13	0.234	277	0.25	0.13	7.1	224	0.25	0.13	6.8	171	0.25
15	0.23	0.156	277	0.25	0.23	7.6	224	0.25	0.23	7.6	171	0.25
16	0.25	0.156	277	0.25	0.25	7.7	224	0.25	0.25	7.7	171	0.25
17	0.10	0.625	277	0.25	0.10	6.9	224	0.25	0.10	6.5	171	0.25

Table V-4. Terminal Unit Test Stand Settings for the April 5 Operating Profile.

Test Point Settings Apr 5												
	Zone 1 - S12C				Zone 2 - S8C				Zone 3 - S8C			
Hour	Primary Static (in)	Primary Air Damper (V)	SCR Voltage (V)	Downstream Static (in)	Primary Static (in)	Primary Air Damper (V)	SCR Voltage (V)	Downstream Static (in)	Primary Static (in)	Primary Air Damper (V)	SCR Voltage (V)	Downstream Static (in)
8	0.10	4.258	277	0.25	0.10	6.3	277	0.25	0.10	7.1	277	0.25
9	0.10	2.852	277	0.25	0.10	4.5	277	0.25	0.10	7.0	277	0.25
10	0.10	2.188	277	0.25	0.10	6.1	277	0.25	0.10	7.1	277	0.25
15	0.13	0.313	277	0.25	0.13	5.9	277	0.25	0.13	5.9	277	0.25
16	0.14	0.273	277	0.25	0.14	6.4	277	0.25	0.14	6.6	277	0.25
17	0.10	3.008	277	0.25	0.10	7.0	277	0.25	0.10	7.1	277	0.25

Table V-5. Terminal Unit Test Stand Settings for the July 6 Operating Profile.

Test Point Settings Jul 6												
	Zone 1 - S12C				Zone 2 - S12B				Zone 3 - S8C			
Hour	Primary Static (in)	Primary Air Damper (V)	SCR Voltage (V)	Downstream Static (in)	Primary Static (in)	Primary Air Damper (V)	SCR Voltage (V)	Downstream Static (in)	Primary Static (in)	Primary Air Damper (V)	SCR Voltage (V)	Downstream Static (in)
8	0.10	3.672	277	0.25	0.10	4.4	277	0.25	0.10	7.1	277	0.25
9	0.10	2.188	277	0.25	0.10	4.4	277	0.25	0.10	7.1	277	0.25
10	0.10	1.406	277	0.25	0.10	3.7	277	0.25	0.10	6.5	277	0.25
15	0.14	0.313	277	0.25	0.14	3.2	277	0.25	0.14	3.4	277	0.25
16	0.15	0.273	277	0.25	0.15	3.3	277	0.25	0.15	3.2	277	0.25
17	0.10	2.813	277	0.25	0.10	3.6	277	0.25	0.10	3.6	277	0.25

Table V-6. Terminal Unit Test Stand Settings for the September 28 Operating Profile.

Test Point Settings Sep 28												
	Zone 1 - S12C				Zone 2 - S12B				Zone 3 - S12A			
Hour	Primary Static (in)	Primary Air Damper (V)	SCR Voltage (V)	Downstream Static (in)	Primary Static (in)	Primary Air Damper (V)	SCR Voltage (V)	Downstream Static (in)	Primary Static (in)	Primary Air Damper (V)	SCR Voltage (V)	Downstream Static (in)
8	0.10	3.672	277	0.25	0.10	1.9	277	0.25	0.10	7.0	277	0.25
9	0.10	2.188	277	0.25	0.10	1.3	277	0.25	0.10	6.3	277	0.25
10	0.10	1.406	277	0.25	0.10	0.9	277	0.25	0.10	5.8	277	0.25
15	0.14	0.313	277	0.25	0.14	1.0	277	0.25	0.14	1.7	277	0.25
16	0.15	0.273	277	0.25	0.15	1.4	277	0.25	0.15	1.8	277	0.25
17	0.10	2.813	277	0.25	0.10	1.8	277	0.25	0.10	3.2	277	0.25

The values shown in Table V-3 through V-6 were used as control points and operational settings with the three zone test stand when the series terminal units were tested.

PARALLEL TEST MATRIX

After the operating points were selected, the settings to be used for the test stand were determined for the parallel terminal units. The zone terminal units were set up based on the peak cooling capacity of the terminal unit and the peak cooling load of the zone. Using the normalized loads that were scaled to the capacity of the terminal unit, the test stand settings were determined using the three zone series terminal unit model to determine the operating settings of the test stand zones. Tables V-7 through V-10 show the predicted test stand control system and duct settings for each hour selected as a test point.

Table V-7. Terminal Unit Test Stand Settings for the January 4 Operating Profile.

4-Jan												
	Zone 1				Zone 2				Zone 3			
	Primary Static	Primary Damper	SCR V	Downstream Static	Primary Static	Primary Damper	SCR V	Downstream Static	Primary Static	Primary Damper	SCR V	Downstream Static
8	0.173	0.00	265	0.123	0.173	0.63	0	0.0992	0.173	1.25	0	0.099
9	0.200	0.00	0	0.150	0.200	0.00	0	0.1530	0.200	0.63	0	0.153
10	0.274	0.00	0	0.174	0.274	0.00	0	0.1778	0.274	0.63	0	0.178
15	0.463	0.00	0	0.263	0.463	0.00	0	0.2688	0.463	0.31	0	0.269
16	0.478	0.00	0	0.278	0.478	0.00	0	0.2834	0.478	0.31	0	0.283
17	0.195	0.00	0	0.145	0.195	0.00	0	0.1481	0.195	0.63	0	0.148

Table V-8. Terminal Unit Test Stand Settings for the April 5 Operating Profile.

5-Apr												
	Zone 1				Zone 2				Zone 3			
	Primary Static	Primary Damper	SCR V	Downstream Static	Primary Static	Primary Damper	SCR V	Downstream Static	Primary Static	Primary Damper	SCR V	Downstream Static
8	0.182	2.19	0	0.132	0.182	1.6	220	0.4383	0.182	3.44	175	0.258
9	0.853	4.69	0	0.203	0.853	0.9	0	0.0540	0.853	5.00	175	0.300
10	0.286	0.94	0	0.236	0.286	2.5	220	0.4557	0.286	3.75	175	0.282
15	0.457	0.31	0	0.357	0.457	4.7	0	0.0267	0.457	4.38	0	0.025
16	0.477	0.00	0	0.377	0.477	4.1	220	0.4448	0.477	4.06	175	0.344
17	0.247	1.25	0	0.197	0.247	2.5	220	0.3778	0.247	3.44	175	0.275

Table V-9. Terminal Unit Test Stand Settings for the July 6 Operating Profile.

6-Jul												
	Zone 1				Zone 2				Zone 3			
	Primary Static	Primary Damper	SCR V	Downstream Static	Primary Static	Primary Damper	SCR V	Downstream Static	Primary Static	Primary Damper	SCR V	Downstream Static
8	0.213	1.88	0	0.163	0.213	5.3	240	0.3107	0.213	3.75	175	0.251
9	0.287	0.94	0	0.237	0.287	5.3	240	0.3467	0.287	3.75	175	0.286
10	0.317	0.63	0	0.267	0.317	4.7	240	0.4253	0.317	3.44	175	0.334
15	0.476	0.00	0	0.376	0.476	5.9	0	0.0420	0.476	2.81	0	0.094
16	0.543	0.31	0	0.393	0.543	6.6	0	0.0358	0.543	2.81	0	0.102
17	0.257	1.25	0	0.207	0.257	4.4	240	0.4327	0.257	2.19	0	0.075

Table V-10. Terminal Unit Test Stand Settings for the September 28 Operating Profile.

28-Sep												
	Zone 1				Zone 2				Zone 3			
	Primary Static	Primary Damper	SCR V	Downstream Static	Primary Static	Primary Damper	SCR V	Downstream Static	Primary Static	Primary Damper	SCR V	Downstream Static
8	0.213	1.88	0	0.163	0.213	2.8	0	0.1157	0.213	0.31	277	0.464
9	0.287	0.94	0	0.237	0.287	1.9	0	0.1775	0.287	4.06	0	0.029
10	0.317	0.63	0	0.267	0.317	0.9	0	0.2240	0.317	3.44	0	0.042
15	0.672	1.88	0	0.376	0.672	2.5	0	0.2690	0.672	0.31	0	0.227
16	0.673	1.56	0	0.393	0.673	3.4	0	0.2141	0.673	0.31	0	0.228
17	0.330	1.88	0	0.207	0.330	3.1	0	0.1270	0.330	0.00	0	0.132

The values shown in Table V-7 through V-10 were used as control points and operational settings with the three zone test stand when the parallel terminal units were tested.

EXPERIMENTAL PROCEDURE

The experimental procedure consisted of setting up the three zones according to the test matrix and then gathering data for a period of ten minutes after the measured values had achieved steady state. Steady state was defined as no changes in temperature greater than 2°F (1.2°C) for more than five minutes.

Setting up the three zones was the first step in the experimental procedure. The conditions were dictated by the test matrix. The test matrix specified the operating conditions for all three zones and detailed everything about the operating conditions of the zones. The test matrix specified the upstream static pressure, the downstream static pressure, the primary air flow control damper position, and the SCR setting for the terminal unit fan. The operating parameters for all three zones were specified and the operator prepared to take data by adjusting the control points in the test setup until the specified conditions had been achieved.

After the conditions specified by the test matrix had been reached and steady state operation established, the data acquisition system was used to acquire and store the test data into the SQL database.

For a number of the tests, the operating conditions could not be reached as specified by the test matrix. In some cases, the quantity of primary air could not be reached

because the primary fan of the test apparatus could not generate enough static pressure to move the air through the test stand.

RESULTS

The data that were gathered from the tests conducted using the test stand were evaluated and used to verify the three zone models. The verification procedure for the three zone models is covered in the chapters that discuss each model – series and parallel.

The data that were used for the model verification were not the raw sample data gathered during the tests. The raw data were evaluated statistically and the results of the analysis were used to verify the models. The statistical evaluation of the raw data consisted of calculating the median and standard deviation for each set of data and for each channel of data.

For example, a typical data set consisted of ten minutes of one minute data which resulted in 10 data points for each channel. The median point for each channel was calculated along with the standard deviation for that channel. The median values from the sampled data were used to evaluate the three zone model.

Table V-11 shows a sample set of raw data gathered during a test that was done using series VAV terminal units. Not all of the channels sampled during the test were included in Table V-11. Table V-11 shows the raw one minute data as well as the median and standard deviation values that resulted from the sampled data.

Table V-11. Sample Data From a Series VAV Test.

Start test for April 5 hour 8 series 3/25/06 at 2:49
Stop test for April 5 hour 8 series 3/25/06 at 3:00

Standard Deviation	0.17	0.19	0.13	1.27	1.66	1.42	0.003	0.008	0.003
Mean	64.31	62.44	56.67	401.16	371.57	836.83	0.251	0.218	0.104

	Temp			Watts			Bottom VAV		
datadate	**tempsupplytop**	**tempsupplymid**	**tempsupplybot**	**watts_top**	**watts_mid**	**watts_bot**	**psi_bot_downstream**	**psi_bot_flow**	**psi_bot_upstream**
3/25/2006 15:00	64.06	62.56	56.78	399.25	373.52	836.66	0.245	0.206	0.106
3/25/2006 15:00	64.34	62.50	56.80	400.09	371.96	834.67	0.253	0.212	0.102
3/25/2006 14:59	64.10	62.26	56.69	399.09	372.47	837.17	0.252	0.222	0.102
3/25/2006 14:59	64.14	62.37	56.59	401.15	371.43	837.25	0.253	0.225	0.105
3/25/2006 14:58	64.27	62.22	56.65	401.20	368.03	837.70	0.254	0.195	0.102
3/25/2006 14:58	64.13	62.18	56.52	401.44	372.01	838.05	0.249	0.208	0.108
3/25/2006 14:57	63.93	62.14	56.69	402.93	370.94	837.40	0.251	0.207	0.101
3/25/2006 14:57	64.16	62.40	56.61	403.60	369.39	835.09	0.247	0.214	0.106
3/25/2006 14:56	64.47	62.36	56.62	400.39	371.92	837.67	0.251	0.221	0.105
3/25/2006 14:56	64.35	62.50	56.67	400.40	371.32	837.57	0.250	0.218	0.109
3/25/2006 14:55	64.38	62.41	56.72	400.16	370.29	836.99	0.250	0.222	0.110
3/25/2006 14:55	64.58	62.76	56.84	400.88	371.39	835.66	0.251	0.221	0.101
3/25/2006 14:54	64.35	62.56	56.59	401.79	372.87	834.46	0.246	0.201	0.104
3/25/2006 14:54	64.16	62.46	56.64	401.17	372.81	834.16	0.252	0.220	0.104
3/25/2006 14:53	64.06	62.33	56.59	401.55	371.69	835.30	0.254	0.218	0.103
3/25/2006 14:53	64.26	62.43	56.42	402.66	371.45	837.55	0.250	0.226	0.112
3/25/2006 14:52	64.41	62.54	56.71	400.56	370.65	836.43	0.250	0.218	0.103
3/25/2006 14:52	64.43	62.68	56.67	400.71	373.41	836.61	0.248	0.222	0.103
3/25/2006 14:51	64.43	62.80	56.94	402.36	370.93	836.30	0.252	0.218	0.100
3/25/2006 14:51	64.36	62.77	56.95	403.47	376.11	839.99	0.246	0.218	0.105

UNCERTAINTY ANALYSIS

An uncertainty analysis was performed on the experimental data to provide an upper and lower limit on the estimated error of the measured data. This analysis was carried out using the basic method developed in the 1950's (Kline and McClintock, 1953). Basically, the method allows one to calculate the cumulative measurement uncertainty in a derived quantity based on the cumulative effect of the constituents of the base equation. The model was verified, as described in an earlier chapter, by comparing the predicted supply air temperature to the supply air temperature as measured in the laboratory. If the model was working correctly, these temperatures should be quite close. Though the model predicted the supply temperature trends quite well, the uncertainty analysis allows quantitative comparisons as well.

For example, in the present study the final air delivery from the fan powered parallel terminal unit is given in equation V-1. This equation represents the supply temperature for the case when the terminal unit fan is operating or in the "on" condition.

$$T_{Supply} = \frac{Q_P T_P + Q_F T_R + \frac{3.412 P_{Fan}}{1.08}}{Q_P + Q_F} \tag{V-1}$$

Applying the general uncertainty method to determine propagated uncertainty for equation V-1, results in equation V-2. This equation features five contributing elements to the uncertainty associated with the measurement of the supply temperature. They are uncertainties related to the Primary Volumetric air flow, Fan Volumetric air flow, Power at the fan, Room Temperature, and Plenum or Supply Air Temperature.

$$uT_s = \left[\begin{array}{l} \left(\left(\frac{T_p}{Q_P + Q_F} - \frac{Q_P T_P + Q_F T_R + 3.16 P_{Fan}}{(Q_P + Q_F)^2} \right) uQ_P \right)^2 + \\ \left(\frac{Q_P}{Q_P + Q_F} uT_P \right)^2 + \\ \left(\left(\frac{T_R}{Q_P + Q_F} - \frac{Q_P T_P + Q_F T_R + 3.16 P_{Fan}}{(Q_P + Q_F)^2} \right) uQ_F \right)^2 + \\ \left(\frac{Q_F}{Q_P + Q_F} uT_R \right)^2 + \\ \left(\frac{3.16}{(Q_P + Q_F)} uP_{Fan} \right)^2 \end{array} \right]^{1/2} \tag{V-2}$$

Where:

T_{Supply} = supply air temperature (°F)

uT_S = uncertainty in estimated supply temperature (°F)

T_P = measured plenum supply temperature (also referred to as T_{Supply}) (°F)

uT_P = uncertainty in plenum supply temperature (assumed to be ±0.7°F (1.26°C)) (°F)

T_R = measured room temperature (°F)

uT_R = uncertainty in room temperature (assumed to be ±0.7°F (1.26°C)) (°F)

Q_P = measured Primary air flow rate into box (CFM)

Q_F = measured Fan air flow rate (CFM)

uQ_P = uncertainty in primary air flow (CFM)

uQ_F = uncertainty in box fan air flow (CFM)

P_{Fan} = measured Power used by Terminal Unit fan (Watt)

uP_{Fan} = uncertainty in Power at the Terminal Unit Fan (1% of the reading) (Watt)

Total propagated uncertainty would then be expressed as; $T_S \pm uT_S$. The last three elements have uncertainties that can be expressed directly from the basic measurement statistics of their associated instrumentation. For the temperature sensors, the uncertainty was determined to be ±0.7°F (1.26°C) and for the fan power measurement the uncertainty was 1.0% of the reading.

The uncertainty expressions for Primary air flow and Fan air flow are both cumulative expressions. The Phase I report presented correlating equations for Primary air flow through parallel terminal units as a function of exit damper setting (degrees), upstream static pressure, and downstream static pressure. This equation is repeated from the Phase I report as shown in equation V-3.

$$Q_p = C1\left(1 + C2S + C3S^2\right)\left(P_{up} - P_{dn}\right)^{0.5} \tag{V-3}$$

Uncertainty for the flow in these units was estimated using these correlations and, depending on the unit, the uncertainty equation for the Primary air flow is as follows,

$$uQ_P = \left[\begin{array}{l} \left(\left(C1\left(1 + C2 \times S + C3 \times S^2\right)\left(P_{up} - P_{dn}\right)^{1/2}\right) uDmpr\right)^2 + \\ \left(\left(\dfrac{0.5C1\left(1 + C2 \times S + C3 \times S^2\right)}{\left(P_{up} - P_{dn}\right)^{1/2}}\right) uP_{up}\right)^2 + \\ \left(\left(\dfrac{-0.5C1\left(1 + C2 \times S + C3 \times S^2\right)}{\left(P_{up} - P_{dn}\right)^{1/2}}\right) uP_{up}\right)^2 \end{array}\right]^{1/2} \tag{V-4}$$

Where:

S = damper setting (degrees)

$uDmpr$ = uncertainty in the damper setting (assumed as ± 6 degrees)

P_{up} = upstream static pressure (in.wg.)

P_{dn} = downstream static pressure (in.wg.)

uP_{up} = uncertainty in the upstream static pressure (in.wg.)

uP_{dn} = uncertainty in the downstream static pressures (in.wg.)

$C_1 - C_3$ = correlation constants as given in Table V-12.

Table V-12. Coefficients for Parallel Box Flow Correlations (Phase I Report).

Box	C1	C2	C3
P 8A	1,362.9	-2.020E-02	9.870 E-05
P 8B	1,935.0	-2.480E-02	1.910 E-04
P 8C	1,593.8	-2.730E-02	1.910 E-04
P 12A	7,425.1	-3.070E-02	2.450 E-04
P 12B	5,781.2	-2.770E-02	2.040 E-04
P	183	-	1.630

12C	8.4	1.160E-02	E-05

The Phase I report also presented correlations for terminal unit fan air flow performance as a function of correlating constants, SCR setting, and downstream static pressure. Equation V-5 gives one of these forms (refer to the Phase I report for a complete description of these equations).

$$Q_{Fan} = C1 + C2V + C3V^2 + C4P_{dn} \tag{V-5}$$

The uncertainty in fan air flow is then given by equation V-6

$$uQ_{Fan} = \left[\left((C2 + 2C3V)uV\right)^2 + \left(C4uP_{dn}\right)^2\right]^{1/2} \tag{V-6}$$

Where:

uQ_{Fan} = propagated uncertainty in fan air flow (CFM)

$C_1 - C_4$ = correlation constants as given in Table 9.1

V = SCR voltage setting (Volts)

uV = uncertainty in the voltage setting for the SCR (1% of reading)

P_{dn} = downstream static pressure (in.wg.)

uP_{dn} = uncertainty in the downstream static pressure (in.wg.)

The energy balance for the terminal units changes for the situation where the unit fan is not operating or in the off condition (cooling). Equation V-7 shows the expression for this operating condition as

$$T_S = T_P + \frac{3.412 P_{Htr}}{1.08 Q_S} \tag{V-7}$$

Propagated uncertainty for this case is given by equation V-8 as,

$$uT_S = \left[\left(uT_P\right)^2 + \left(\frac{3.16 uP_{Htr}}{Q_S} \right)^2 + \left(\frac{3.16 P_{Htr} uQ_S}{Q_S^2} \right)^2 \right]^{1/2} \tag{V-8}$$

Where:

T_S = supply air temperature (°F)

uT_S = uncertainty in estimated supply temperature (°F)

T_p = measured plenum supply temperature (also referred to as T_{Supply}) (°F)

uT_P = uncertainty in plenum supply temperature (assumed to be ±0.7°F (1.26°C)) (°F)

Q_S = measured Supply air flow rate out of VAV terminal unit (CFM)

uQ_S = uncertainty in supply air flow (CFM)

P_{Htr} = measured Power consumed at the heating element in the terminal unit (Watt)

uP_{Htr} = uncertainty in heater Power at the terminal unit (1% of the reading) (Watt)

Again, as in previous equations, there is another cumulative uncertainty in the Q_S quantity. That is because Q_S has two components for flow as shown in equation V-9.

$$Q_S = Q_P + Q_{Fan} \tag{V-9}$$

The propagated uncertainty for this expression is

$$uQ_S = \left[uQ_P^2 + uQ_{Fan}^2\right]^{1/2} \tag{V-10}$$

Where:

Q_S = total air flow exiting VAV terminal unit (CFM)

Q_P = measured Primary air flow rate into the VAV terminal unit (CFM)

uQ_P = uncertainty in Primary air flow (CFM)

Q_{Fan} = measured Fan air flow rate into VAV terminal unit (CFM)

uQ_{Fan} = uncertainty in Fan air flow (CFM)

DISCUSSION

In Chapter 5, the methodology was developed on how the model was to be calibrated. To summarize, the model would be used to predict the exiting air temperature for a VAV terminal unit under different loading conditions. Once normalized, these loads were replicated with an experimental setup at the Energy Systems Laboratory and the resulting exiting air temperatures were measured. Upon comparison, the validity of the model could be verified. The uncertainty, or sensitivity analysis, was used not only to quantify cumulative uncertainty in the experimental measurements but also to explore the relative impact of the different physical measurements on experimental uncertainty.

Table V-13 shows a few representative values for six of the VAV terminal units that were tested in this research project.

Table V-13. Uncertainty Results for Four VAV Terminal Units.

Unit Designation	Total Airflow Q_S - CFM (m^3/min)	Uncertainty Q_S - CFM (m^3/min)	Uncertainty Q_P - CFM (m^3/min)	Uncertainty Q_F - CFM (m^3/min)	Uncertainty in T_S - °F (°C)
P8A	354 (10)	75 (2.1)	70 (2)	27 (0.76)	5.2 (9.4)
P12A	714 (20.2)	278 (7.9)	277 (7.8)	27 (0.76)	4.9 (8.8)

P8B	952 (2V-9)	104 (2.9)	74 (2.1)	75 (2.1)	0.9 (1.6)
P12B	1613 (45.7)	213 (V-0)	120 (3.4)	176 (5)	1.1 (2)
P8C	671 (19)	156 (4.4)	47 (1.3)	148 (4.2)	1.1 (2)
P12C	365 (10.3)	107 (3.0)	46 (1.3)	96 (2.7)	7.0 (12.6)

The propagated uncertainty in the Total Airflow for these units varied from 10 – 30%. Note that there is quite a range in the uncertainty for the Supply Air Temperature, T_S, for these particular data points. Figure V-21 shows test data for parallel VAV terminal units where the data are shown from low to high airflow rates against predicted and measured Supply Air Temperatures. This figure shows that the propagated uncertainty is quite high for these units when the units are operating at low flow, or primarily heating, conditions. Throughout the "neutral" of "cooling" region the model trends the actual data very well with uncertainty bands in the predicted temperature often overlapping the measured quantity.

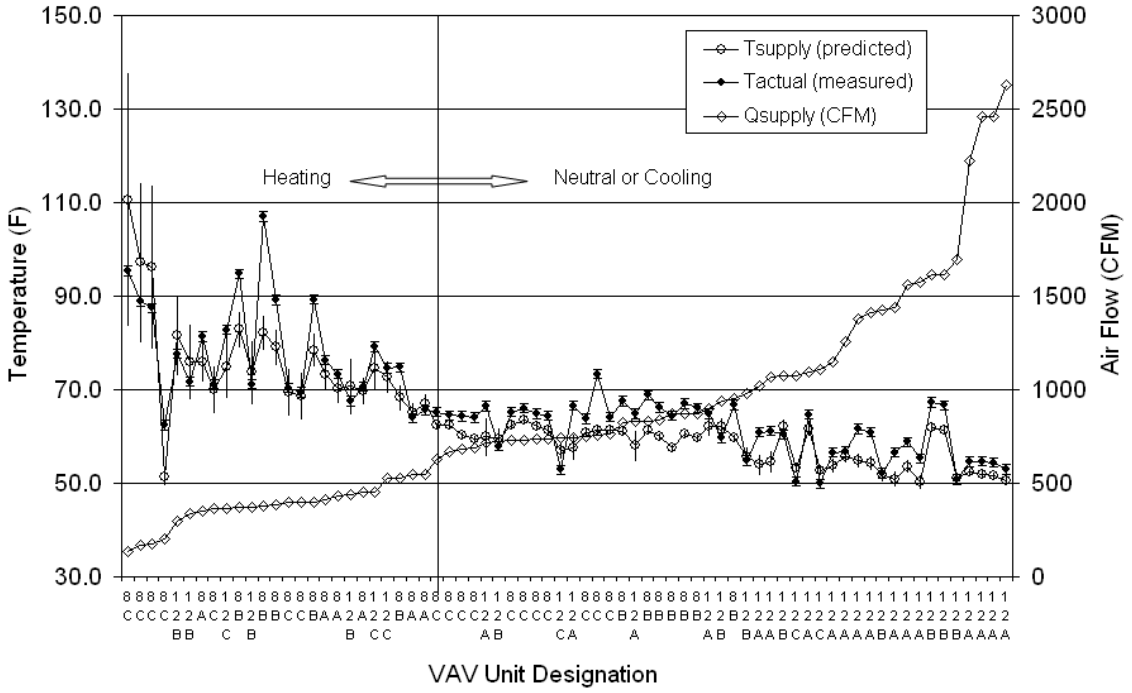

Figure V-21. Parallel VAV Terminal Unit Supply Temperature Data and Airflow Relationship.

The quantitative effect of uncertainty on the energy model would have to take into account the number of hours in the year that the system is in the heating or cooling mode to be able to predict the impact on total system energy. However, it is apparent that the model is very good at predicting Supply Temperatures, especially at higher airflow rates.

Figure V-22 shows the data grouped by Parallel Unit Type that were tested for this study. No particular unit had consistently high experimental uncertainties. This is a "comforting" finding in that it says that there was no systematic errors in the experimental data and that none of the units displayed a consistent poor pattern in performance.

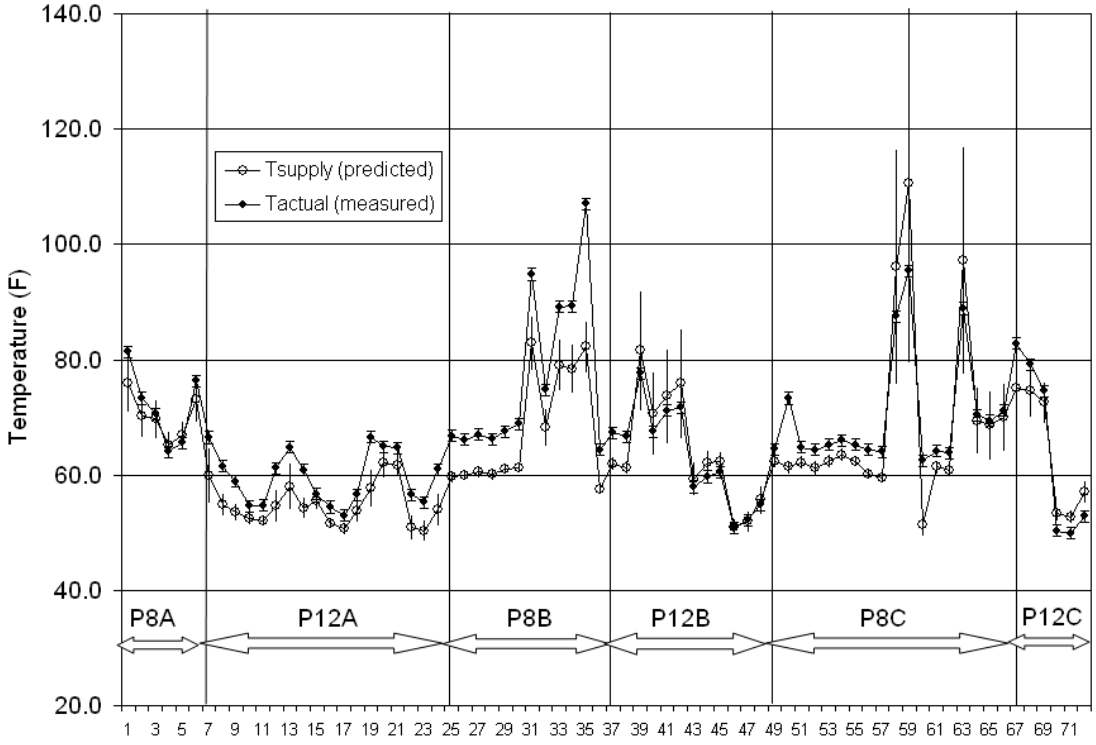

Figure V-22. Predicted vs. Measured Supply Temperatures for Parallel VAV Terminal Units.

Comparing Figure V-22 with V-21, one can see that some of the largest and smallest uncertainties in the temperature data are recorded with the same unit. Again, this is more indication that at low airflow experimental uncertainty is higher. This would be expected because basic instrument measurement uncertainty becomes a larger percentage of the reading at the low end of a given measurement. So, for example, if measuring a very low airflow, we expect a very low differential pressure but the corresponding error associated with that measurement remains unchanged. Whether a large or small differential, the pressure transducer error is stated in the same way for the type of transducers used in this study.

VERIFICATION FOR THE SERIES AND PARALLEL TERMINAL UNITS

The data gathered using the three zone test stand were used to perform the verification analysis of the three zone model. The verification procedure consisted of gathering data from the test stand, feeding the measured data back into the three zone model, and using the predicted air flow rates estimated by the model to predict the supply temperatures. The predicted supply temperatures were then compared to the measured supply temperatures.

The first step in the verification process was the acquisition of data from the test stand. Once the data were gathered, the measured values of upstream static pressure, downstream static pressure, flow sensor pressure, primary air damper position, and SCR voltage were then used with the three zone model in place of the model's predicted values. The model was then used with the measured values to predict the primary, induced, and supply flow rates. Using the updated flow rates, the supply temperature for the zone was then predicted using the measured primary air temperature, fan power, and return air temperature. The estimated supply temperature that was based on measured values was then compared to the measured supply temperature. Figure V-23 shows the graph of the predicted supply temperature and the measured supply temperature for all test points in the series terminal unit test matrix.

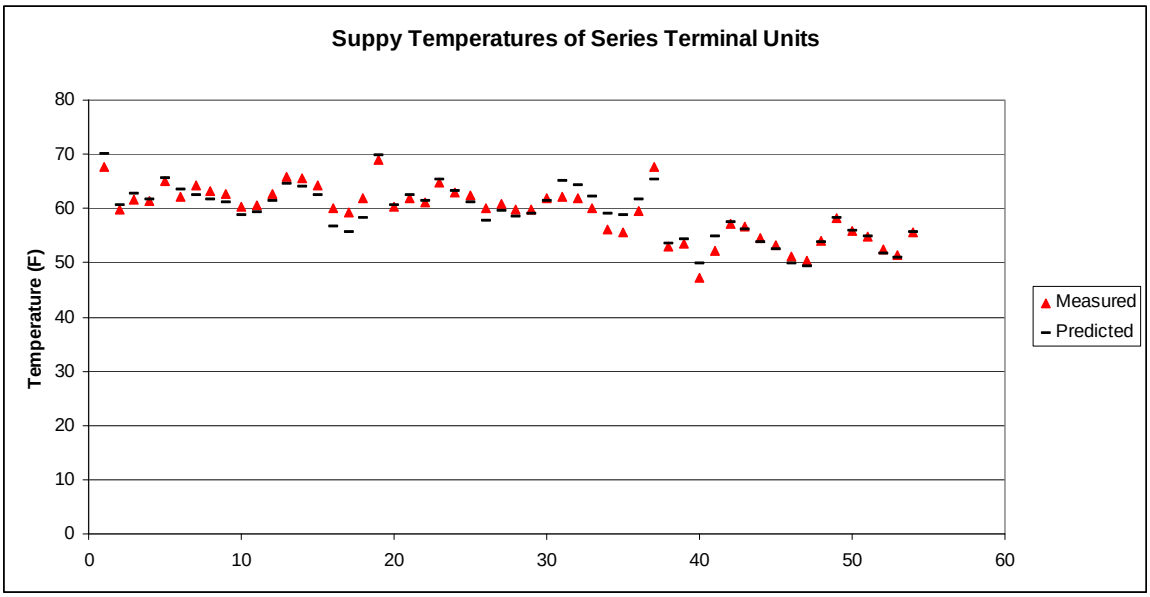

Figure V-23. Graph of Predicted and Measured Supply Temperatures for Fan Powered Series Terminal Units.

The data in Figure V-23 show good agreement between the predicted and measured supply temperatures for fan powered series terminal units which verifies the accuracy of the model.

Figure V-22 shows the graph of the predicted supply temperature and the measured supply temperature for all test points in the parallel terminal unit test matrix.

As with the series terminal unit results, the parallel unit data in Figure V-22 show good agreement between the predicted and measured supply temperatures for fan powered parallel terminal units. Again, these results provide verification of the accuracy of the model.

VITA

Name: Michael A. Davis

Address: New York University in Abu Dhabi

P.O. Box 903

New York, NY 10276-0903

Email Address: michael.davis@nyu.edu

Education: B.S., Mechanical Engineering, Texas A&M University, 1986

M.S., Mechanical Engineering, Texas A&M University, 1994

Ph.D., Mechanical Engineering, Texas A&M University, 2010